Repository Istituzionale dei Prodotti della Ricerca del Politecnico di Bari

The effects of submerged berms on the stability of rubble mound breakwaters

This is a PhD Thesis

Original Citation:
The effects of submerged berms on the stability of rubble mound breakwaters / Celli, Daniele. - ELETTRONICO. - (2019). [10.60576/poliba/iris/celli-daniele_phd2019]

Availability:
This version is available at http://hdl.handle.net/11589/161204 since: 2019-01-21

Published version
DOI:10.60576/poliba/iris/celli-daniele_phd2019

Publisher: Politecnico di Bari

Terms of use:

(Article begins on next page)

12 October 2024

POLITECNICO DI BARI

04
2018

D.R.R.S
Doctor of Philosophy in Environmental and Building Risk and Development

Coordinator: Prof. Michele Mossa

XXXI CYCLE
Curriculum ICAR/02

DICATECh

Department of Civil, Environmental, Building Engineering and Chemistry

The effects of submerged berms on the stability of rubble mound breakwaters

Supervisor: Prof. Michele Mossa
Department of Civil Environmental, Building, Engineering and Chemistry
Technical University of Bari

Supervisor: Prof. Marcello Di Risio
Department of Civil, Construction-Architectural and Environmental Engineering
University of L'Aquila

Ph.D. candidate: Daniele Celli

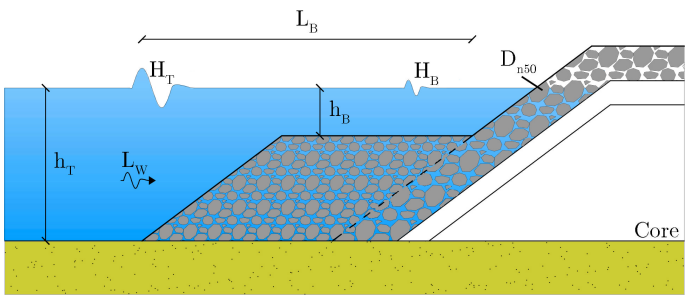

POLITECNICO DI BARI

04
2018

D.R.R.S
Dottorato di Ricerca in Rischio e Sviluppo ambientale, territoriale ed edilizio

Coordinatore Prof. Michele Mossa

XXXI CICLO
Curriculum ICAR/02

DICATECh

Dipartimento di Ingegneria Civile, Ambientale, del Territorio, Edile e di Chimica

Gli effetti delle berme sommerse sulla stabilità delle opere a gettata

Supervisore: Prof. Michele Mossa
Dipartimento di Ingegneria Civile, Ambientale, del Terriotirio, Edile e di Chimica
Politecnico di Bari

Supervisore: Prof. Marcello Di Risio
Dipartimento di Ingegneria Civile, Edile-Architettura e Ambientale
Università dell'Aquila

Dottorando: Daniele Celli

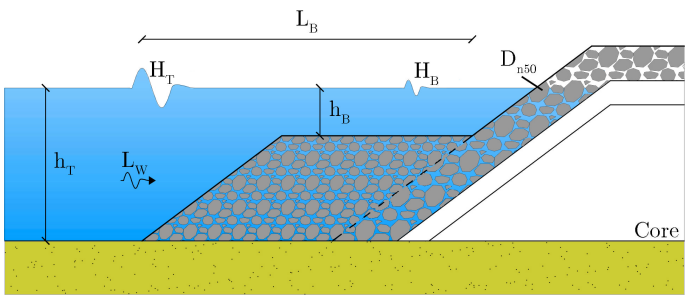

To my Grandparents,
Nicolangelo and *Antonietta*
and to my Parents,
Antonino and *Eleonora*.

ABSTRACT

Berms deployed at the toe of conventional rubble mound breakwaters may be useful for various purposes, i.e. to reduce wave loads acting on the breakwater armor elements, to reduce wave overtopping, to limit momentary liquefaction occurrences under the structure and to protect from the scouring the breakwater toe.

In the first part, the Thesis is aimed to provide a new design criterion for the armor layer of conventional breakwaters with submerged berms marked by small thickness compared to water depth. Indeed, past research studies focused on the influence of relatively high berms on the stability of the armor layer. The design of the berm itself was not tackled herein. The effects of submerged berms on the incident waves transformation have been evaluated by means of a numerical model, validated by using experimental data. Then, a parametric correction factor of the incident significant wave height at the toe of the structure is provided and included in well-established design criteria. The experimental comparison confirmed the reliability of the proposed method by highlighting the importance to use design criteria within their validity ranges, in order to avoid an unsafe dimensioning of the armor elements.

In the second part, the Thesis is aimed to evaluate how submerged berms configuration influence the seabed soil response and momentary liquefaction occurrences around and beneath breakwaters foundation, under dynamic wave loading. The effects of submerged berms on the incident waves transformation have been evaluated by means of the aforementioned phase resolving numerical model for simulating non-hydrostatic, free-surface, rotational flows. The soil response to wave-induced seabed pressures has been evaluated by using an ad-hoc anisotropic poro-elastic soil solver, developed within the OpenFOAM framework. Once the evaluation of the seabed consolidation state, due to the presence of the breakwater, has been performed, the dynamic interaction among water waves, soil and structure has been analyzed by using a one-way coupling boundary condition. A parametric study has been carried out by varying the berm configuration (i.e. its height and its length), keeping constant the offshore regular wave conditions, the wa-

ter depth and the elastic properties of the soil. Results indicate that the presence of submerged berms tends to mitigate the liquefaction probability if compared to straight sloped conventional breakwater without a berm. In addition, it appears that the momentary liquefaction phenomena are more influenced by changing the berm length rather than the berm height.

In the last part, the Thesis is focused on the role of submerged berms on the random wave-induced momentary liquefaction. A numerical study has been carried out by selecting three ad-hoc domain, among those tested under regular wave condition. Indeed, the influence of random wave loading on the momentary liquefaction occurrences is investigated through a comparison with the corresponding representative regular wave results. Due to the wave randomness, the random wave-induced momentary liquefaction depths are larger than the corresponding representative regular ones. This means that the evaluation of the momentary liquefaction occurrences, under the action of representative regular waves, could underestimate the liquefaction depth, determining an unsafe design in the practice.

Keywords: Breakwaters, Berm, Physical model tests, Numerical models, Hydraulic Stability, Momentary liquefaction, Design Criteria

SOMMARIO

L'introduzione di berme sommerse nella geometria delle convenzionali opere a gettata può risultare efficace per la riduzione dei cedimenti delle fondazioni, e per limitare i fenomeni di scavo nella parte antistante le opere. Allo stesso tempo, le berme sommerse possono incrementare la stabilità dello strato di armatura e diminuire l'entità del sormonto, se comparate al caso di opere a gettata convenzionali, prive di berme.

Con riferimento alla prima parte, lo scopo della Tesi è quello di fornire un innovativo criterio progettuale per le opere a gettata convenzionali dotate di berme sommerse, caratterizzate da altezze ridotte se comparate alla profondità al di sopra delle stesse. La trasformazione delle onde incidenti a opera delle berme sommerse è stata valutata attraverso l'utilizzo di un modello numerico, preliminarmente validato attraverso il confronto con risultati sperimentali. Attraverso uno studio parametrico, è

stato determinato un fattore correttivo per l'altezza d'onda significativa incidente, da utilizzare all'interno di criteri progettuali esistenti. Il confronto con i risultati sperimentali ha confermato l'affidabilità del metodo proposto, sottolineando l'importanza dell'utilizzo di criteri progettuali all'interno del loro intervallo di validità, al fine di evitare un dimensionamento degli elementi costituenti l'armatura a sfavore di sicurezza.

Nella seconda parte, la Tesi è volta alla valutazione degli effetti della geometria delle berme sommerse sulla risposta del suolo e sui fenomeni di liquefazione momentanea in corrispondenza delle fondazioni di opere a gettata, sollecitate dal carico dinamico delle onde di mare. Come in precedenza, la trasformazione delle onde incidenti a opera delle berme sommerse è stata valutata attraverso l'utilizzo di un modello numerico in grado di simulare flussi rotazionali, non idrostatici, a superficie libera. La risposta del terreno è stata valutata attraverso il ricorso a un modello poro-elastico del terreno, sviluppato in ambiente OpenFOAM. Determinato lo stato di consolidazione del terreno che si instaura in seguito alla realizzazione di una generica opera a gettata, l'interazione dinamica tra le onde del mare, il terreno e la struttura è stata analizzata sfruttando una condizione al contorno in grado di accoppiare i differenti modelli, preliminarmente citati. E' stato quindi realizzato uno studio parametrico al variare della geometria delle berme sommere (in termini di altezza e lunghezza), mantenendo costante lo stato di mare "a largo" e le proprietà elastiche del terreno. I risultati indicano che la presenza di berme sommerse tende a mitigare il fenomeno della liquefazione momentanea se comparati al caso di opere a gettata prive di berme sommerse. Inoltre, si evince che il fenomeno della liquefazione momentanea è maggiormente influenzato da variazioni della lunghezza della berma piuttosto che della sua altezza.

Nell'ultima parte, la Tesi si focalizza sul ruolo che hanno le berme sommerse sulla liquefazione momentanea indotta dall'azione di onde irregolari. E' stato eseguito uno studio numerico selezionando tre configurazioni geometriche, precedentemente testate sotto l'azione di onde regolari. Ciò ha permesso di valutare l'influenza che hanno le onde irregolari sul fenomeno della liquefazione momentanea, attraverso il confronto con i risultati derivanti dalla presenza di onde regolari. Gli strati di suolo interessati dal fenomeno della liquefazione risultano essere più ampi in presenza di onde irregolari. Pertanto, la riproduzione degli effetti di onde irregolari attraverso onde regolari

rappresentative, può portare a una sottostima delle profondità degli strati di terreno interessati da liquefazione momentanea e pertanto a una progettazione a sfavore di sicurezza.

Parole chiave: Opere a gettata, Berme, Modellazione fisica, Modellazione numerica, stabilità idraulica, Liquefazione Momentanea, Criteri progettuali

ACKNOWLEDGMENTS

First of all, I would like to express my sincere gratitude to my supervisor Prof. Marcello Di Risio for having passed on me part of his great knowledge and passion for the coastal engineering world. His guidance has been very important during my PhD Study, as well as our talks at LIam of the University of L'Aquila. A great part of my scientific knowledge I owe to you, Marcello.

I would also like to thank my supervisor Prof. Michele Mossa for make me feel very welcome at the Technical University of Bari. In addition, I greatly appreciated the friendly hosting I received from the staff of the Coastal Engineering Laboratory (LIC).

During my PhD I visited the University of Stavanger. My special gratefulness is given to Prof. Muk Chen Ong and Dr. Yuzhu Li for making me feel so at home at UiS and for sharing their experience and knowledge within the wave-soil-structure framework.

Many thanks goes to Dr. Davide Pasquali. His continuous support and motivation have helped me during my PhD experience at the University of L'Aquila. Moreover, I would also like to thank the lab technician Mr. Lucio Matergia, without whose help every experimental test wouldn't be possible and Dr. Piera Fischione, the new Ph.D student of the LIam group, for the shared moments in the office and coffee room.

A special thanks goes to Paola, for sharing with me an important part of my life, always by my side. Our joyful days, our holidays, our daily life have made my Phd experience more enjoyable. Thank you for teaching me to never give up.

Last but not least, I would like to express my huge gratitude to my parents and my sister for endlessly supporting me during all my studies. Without your help, your sympathy, your encouragement, your life coaching, nothing would have been possible.

CONTENTS

1 INTRODUCTION 1
1.1 Thesis outline 5
2 THE ROLE OF SUBMERGED BERMS ON THE HYDRAULIC STABILITY OF RUBBLE MOUND BREAKWATERS 7
2.1 The conventional rubble mound breakwater 7
2.2 Hydraulic stability of breakwaters: state of the art 8
2.3 Methodology 12
2.4 Experimental investigation 16
2.4.1 Scaling 18
2.4.2 Experimental tests 23
2.5 Numerical investigation 25
2.5.1 The numerical model 25
2.5.2 Model validation 27
2.5.3 Numerical results 32
2.6 The proposed stability formula 35
2.6.1 Example calculation 38
3 THE ROLE OF SUBMERGED BERMS ON THE SOIL STABILITY AROUND RUBBLE MOUND BREAKWATERS 43
3.1 Wave-induced liquefaction 43
3.2 Methodology 45
3.3 The matemathical model 47
3.3.1 The soil numerical model 48
3.4 Model calibration and validation 49
3.5 Numerical investigations 55
3.6 Results and discussion 58
3.6.1 Consolidation 58
3.6.2 Wave-induced seabed response 59
3.6.3 Momentary liquefaction analysis 61
4 THE ROLE OF SUBMERGED BERMS ON THE RANDOM WAVE-INDUCED MOMENTARY LIQUEFACTION AROUND RUBBLE MOUND BREAKWATERS 69
4.1 Introduction 69
4.2 Model calibration and validation 72
4.3 Numerical investigation 73
4.4 Results 75

4.4.1 Consolidation 75
4.4.2 Momentary liquefaction analysis 76
5 CONCLUDING REMARKS 82

BIBLIOGRAPHY 85

LIST OF FIGURES

Figure 2.1 Typical cross section of conventional rubble mound breakwater. 7

Figure 2.2 Geometric berm parameters as defined by van Gent., 2013. 13

Figure 2.3 Geometric parameters definition of conventional rubble mound breakwaters with a berm. The core runs below the berm only for considerable values of berm height. 13

Figure 2.4 The wave flume and the wave generator components 17

Figure 2.5 The experimental breakwater during the investigation. 23

Figure 2.6 Sketch aimed at illustrating the difference between extracted and displaced elements. 25

Figure 2.7 Sketch of the experimental layout. Wave gauges deployed along the flume are referred to with the symbol "WG". Bottom and left axes refer to prototype dimensions if a model-to-prototype scale ratio equal to 20 is considered. Upper and right axes refer to model dimensions. 27

Figure 2.8 Upper panel: Jonswap spectrum ($\gamma = 3.3$) resulting from H_{m0} = 2.5 and T_p = 8.8. Lower panel: Synthesized surface elevation time series. 28

Figure 2.9 Spatial distribution of the 2% exceedance individual wave crests (positive values) and troughs (negative values) numerically computed (dashed lines) and experimentally observed (triangular markers); the maximum crest and minimum trough elevations are depicted (circular markers and continuous lines); also the significant wave height is shown in the plot (diamonds and dash dot line) 30

Figure 2.10 Q-Q Plots of the observed (z_{zc-exp}) and computed (z_{zc-num}) EPDFs of individual wave crests and troughs; from left to right, the diagrams refer to wave gauges WG1, WG4 and WG7 (see Figure 2.7); shaded areas depict the $\pm$ 10% error; triangular markers refer to the same values of the Figure 2.9. 30

Figure 2.11 Wave energy density spectra of the observed total water levels (dashed lines) and of the computed total water levels (continuous lines); from left to right, the diagrams refer to wave gauges WG3, WG6 and WG9 (see Figure 2.7). Shaded areas indicate the standard errors 31

Figure 2.12 Incident (higher values) and reflected (lower values) wave energy density spectra of the observed water levels (dashed lines) and of the computed water levels (continuous lines) estimated by means of the standard method proposed by Mansard and Funke (1980)); from left to right, the diagrams refer to the locations of wave gauges WG3, WG6 and WG9 (see Figure 2.7). Shaded areas indicate the standard errors 32

Figure 2.13 Sketch of the computational domain used to catch the influence of the berm on the incident water wave propagation. The same symbols used to indicate experimental wave gauges are used to indicate the locations where the numerical results have been extracted. 32

Figure 2.14 Variation of the normalized 2% exceedance individual wave height over the berm ($H^B_{2\%}/H^T_{2\%}$, upper panels) and of the normalized significant wave height over the berm (H^B_s/H^T_s, lower panels) as a function of the dimensionless water depth over the berm (h_B/h_T, left panels) and of the dimensionless berm length (L_B/L_W, right panels). 35

Figure 2.15 Scatter plot of the estimation (γ_{comp}) obtained by Equation 2.33 and the values of γ computed by means of the numerical model (γ_{num}). Shaded area refers to the $\pm$ 10 % deviation. 37

Figure 2.16 Scatter plot of the observed damage parameter $\left(S_d/\sqrt{N_W}\right)_{obs}$ to the estimated damage parameter $\left(S_d/\sqrt{N_W}\right)_{est}$ by means of the criteria proposed by Van Der Meer, 1988 (circles), by van Gent, 2013 (squares)and by means of the criterion proposed herein (diamonds). Solid line refers to the perfect fitting. Dashed lines refer to relative errors (expressed as a percentage) with a 20% step (only the $\pm$100% relative error lines have been labeled). 38

Figure 2.17 Comparison of the mean diameter of armor elements estimated by means of the criteria proposed by Van Der Meer (1988), ($D_{n50-VDM}$), by van Gent (2013), (D_{n50}, dashed lines) and proposed herein (D_{n50} , continuous lines). The curves refer to the ratio of D_{n50} to $D_{n50-VDM}$ (equal to the ratio of the related stability numbers, i.e. N_{s-VDM}/N_s). Thin lines are intended to indicate that the criterion is used outside the validity ranges, thick lines that the criterion is used inside the validity ranges. Main parameters: S_d = 2, h_T = 6 m, cot α = 2.5. 39

Figure 2.18 Sketch aimed at illustrating the geometry adopted for the example calculation. 40

Figure 3.1 Seabed pressure under progressive wave. 45

Figure 3.2 Sketch of vertical pore pressure distribution in different type of soil. 45

Figure 3.3 One-way boundary coupling algorithm of wave-structure-seabed interaction. 47

Figure 3.4 Variation of the normalized wave pressure height $P_{dxi}/P_{dx0.1}$, as a function of the number of computational points of the mesh. 50

Figure 3.5 Sketch of the computational domain implemented to numerically catch the wave-induced seabed pressure by using SWASH and OpenFOAM solver. 51

Figure 3.6 Spatial distribution of the maximum and minimum individual wave-dynamic pressure crests and troughs values, computed by using SWASH (blue dashed and magenta dot dashed lines) and OpenFOAM solver (green continuous and cyan dotted lines). 52

Figure 3.7 Sketch of the computational domain implemented for the soil model convergency study. It is shown the sample point (x = 330.2 m, z =-2 m), where the pore pressures are collected. 53

Figure 3.8 Grid convergence for dynamic pore pressure in the seabed (sample point coordinates: x = 330.2 m , z = -2 m). 54
Figure 3.9 Geometric parameters definition of conventional rubble mound breakwater with a berm. The berm and core toe positions could vary among the simulated test cases. 56
Figure 3.10 Vertical soil displacement U_z after the completion of the consolidation process for a breakwater with submerged berm characterized by h_B/h_T = 0.49 and L_B/L_W = 0.25. 58
Figure 3.11 Vertical effective stress $\sigma_z^{'}$ after the completion of the consolidation process for a breakwater with submerged berm characterized by h_B/h_T = 0.49 and L_B/L_W = 0.25. 59
Figure 3.12 Transient pore pressure and seepage flow at the instant t = 676 s (H = 4 m) for a breakwater with submerged berm characterized by h_B/h_T = 0.59 and L_B/L_W = 0.30. 60
Figure 3.13 Shear stress σ_{xz} distribution in the seabed at the instant t = 676 s (H = 4 m) for a breakwater with submerged berm characterized by h_B/h_T = 0.59 and L_B/L_W = 0.30. 61
Figure 3.14 Wave-induced momentary liquefaction with reference to a breakwater without submerged berm. Upper panel: momentary liquefaction maximum depth around and beneath the structure. Lower panel: zoom of the momentary liquefaction maximum area splits into two subareas, according to the location of the liquefaction occurrences. Dark green subarea refers to maximum liquefaction depth in front of the structure up to the breakwater toe. Light green subarea refers to maximum liquefaction depth beneath the structure. 63

Figure 3.15 Wave-induced momentary liquefaction with reference to breakwater with submerged berm characterized by h_B/h_T = 0.59 and L_B/L_W = 0.17. Upper panel: momentary liquefaction maximum depth around and beneath the structure. Lower panel: zoom of the momentary liquefaction maximum area splits into two subareas, according to the location of the liquefaction occurrences. Dark green subarea refers to maximum liquefaction depth in front of the structure, up to the breakwater toe. Light green subarea refers to maximum liquefaction depth beneath the structure. 64

Figure 3.16 Wave-induced momentary liquefaction with reference to breakwater with submerged berm characterized by h_B/h_T = 0.59 and L_B/L_W = 0.30. Upper panel: momentary liquefaction maximum depth around and beneath the structure. Lower panel: zoom of the momentary liquefaction maximum area splits in two subareas, according to the location of the liquefaction occurrences. Dark green subarea refers to maximum liquefaction depth in front of the structure, up to the breakwater toe. Light green subarea refers to maximum liquefaction depth beneath the structure. 65

Figure 3.17 Variation of d^*, (i.e. the ratio $\bar{d}_{ext}/\bar{d}_{int}$) as a function of the dimensionless berm length (L_B/L_W , upper panel) and of the dimensionless water depth over the berm (h_B/h_T , lower panel). 66

Figure 3.18 Variation of the normalized mean maximum liquefaction depth d_m/d_{m0} as a function of the dimensionless berm length (L_B/L_W, upper panel) and of the dimensionless water depth over the berm (h_B/h_T, lower panel). 67

Figure 4.1 Time history of the simulated irregular waves, equal for each simulation. The represented water levels do not take into account the offshore water depth h = 12 m. 74
Figure 4.2 Vertical effective stress $\sigma_z^{'}$ after the completion of the consolidation process for a breakwater with submerged berm characterized by h_B/h_T = 0.19 and L_B/L_W = 0.35. 76
Figure 4.3 Vertical soil displacement U_z after the completion of the consolidation process for a breakwater with submerged berm characterized by h_B/h_T = 0.19 and L_B/L_W = 0.35. 76
Figure 4.4 Regular wave-induced momentary liquefaction depth percentiles with reference to a breakwater without submerged berm. 77
Figure 4.5 Regular wave-induced momentary liquefaction depth percentiles with reference to a breakwater with submerged berm characterized by h_B/h_T = 0.59, L_B/L_W = 0.35. 77
Figure 4.6 Regular wave-induced momentary liquefaction depth percentiles with reference to a breakwater with submerged berm characterized by h_B/h_T = 0.19, L_B/L_W = 0.35. 78
Figure 4.7 Random wave-induced momentary liquefaction depth percentiles with reference to a breakwater without submerged berm. 79
Figure 4.8 Random wave-induced momentary liquefaction depth percentiles with reference to a breakwater with submerged berm characterized by h_B/h_T = 0.59, L_B/L_W = 0.35. 79
Figure 4.9 Random wave-induced momentary liquefaction depth percentiles with reference to a breakwater with submerged berm characterized by h_B/h_T = 0.19, L_B/L_W = 0.35. 80

LIST OF TABLES

Table 2.1 Synthesis of the scaling factors 19

Table 2.2 Wave parameters (offshore spectral wave height H_{m0}, peak wave period T_p, wave length at the toe of the berm L_W) and berm configuration (berm length L_B, water depth at the toe of the berm h_T and over the berm h_B) used to validate the numerical model. 29

Table 2.3 Comparison among the validity ranges of existing criteria in terms of berm parameters (VDM1988 refers to the criterion proposed by Van Der Meer, 1988 and VG2013 to the criterion proposed by van Gent, 2013) and the proposed criterion. 33

Table 2.4 Empirical parameters to be used in Equation 2.33 along with their 0.95 confidence interval. 36

Table 2.5 Wave characteristics at the toe of the structure, evaluated by means of a standard spectral wave propagation model. 40

Table 2.6 Main parameters and results of the example calculation (VDM1988 refers to the criterion proposed by Van Der Meer, (1988) and VG2013 to the criterior porposed by van Gent, (2013)). 42

Table 3.1 Mesh parameters for the soil model convergency study (relative change is evaluated with respect to the finest Mesh No.3). 54

Table 3.2 Parameter settings for wave-structure-seabed interaction. 56

ACRONYMS

- *WSSI*: Wave-Structure-Seabed-Interface
- *SWL*: Still Water Level
- *ARC*: Active Reflection Compensation system
- *EPDF*: Empirical Probability Distribution Function
- *FVM*: Finite Volume Method
- *2D*: Two-dimensional
- *2DV*: Two-dimensional vertical

1 INTRODUCTION

Conventional rubble mound breakwaters are widely used all around the world, mainly to provide protection for harbors (e.g. Van Der Meer, 1988) and to preserve coastal areas (Di Risio et al., 2010; Lamberti et al., 2005) from currents and wave actions. Therefore, the design of any structure is aimed to ensure stability against such environmental loads. This is pursued by paying attention to the armor layer design. Indeed, many empirical methods for the selection of the armor unit size are available in literature, for both breaking and non-breaking conditions (e.g. Herrera et al., 2017; Hudson, 1959; Iribarren, 1938; Melby and Kobayashi, 1998; Van Der Meer, 1987; 1988; van Gent et al., 2004).

Usually, in front of breakwaters, scour protection and armor layer support are obtained by using a structure toe (e.g. van Gent and van der Werf, 2014), especially when the armor layer is made up of concrete units or when it is necessary to protect the rubble mound breakwater toe from wave breaking.

For particular cases, it could be necessary to extend the toe (e.g. Herrera et al., 2016), in order to limit the scour related to coastal currents and storm surge (Pasquali et al., 2015) as well. In such cases, it may be appropriate to modify the straight slopes of conventional breakwaters, by deploying a submerged berm marked by higher than usual length. In practise, the berm represents an extention of the toe berm. Indeed, when a rubble mound breakwater with submerged berm is considered, it must not be confused with a reshaping berm breakwater. The presence of submerged berms could be valuable even in reducing wave overtopping, at least for relative high berms, i.e. when the water depth on the berm is small enough and the berm is wide enough to induce a significant wave height decrease (e.g. see Fig. 1 of van Gent, 2013).

Since the loads due to the incident water wave action are reduced in presence of a berm with low water depths (Van Der Meer, 2011), the usage of the aforementioned empirical methods for the armor unit size dimensioning, may lead to an overestimation of the rock size required for the stability. Then, it is necessary to refer to ad-hoc methods that take into account the influence of submerged berms upon the stability of the armor layer.

Recently, van Gent, (2013) provided empirical relationship aimed to evaluate correction factors to be applied to existing design criterion (van Gent et al., 2004), in order to consider the berm influence on the rock armor stability. Nevertheless, the experimental range investigated by van Gent, (2013) is limited to rather high berms, i.e. characterized by small values of water depth over the berms compared to the water depth at the toe. For submerged berm marked by small thickness compared to water depth, the use of previous methods may lead to an underestimation of the armor layer rock size (i.e. on the unsafe side).

The first part of this Thesis aims to provide a design criterion for the armor layer rock elements of conventional rubble mound breakwater with submerged berm, extending the validity range of the method suggested by van Gent, (2013).

The method proposed herein is based on the use of numerical and experimental tools and on a rationale aimed to continue using well-established stability formulas, properly modified to be employed as a reliable design criterion when a submerged berm is foreseen.

Other than the structural response, in designing rubble mound breakwaters, the soil response and its effect on the foundation stability must be assessed. Indeed, as reported in literature (e.g. Chung et al., 2006; Elsafti and Oumeraci, 2016; Franco, 1994; Oumeraci, 1994; Zhao et al., 2017) the stability of such structures can be threatened also by geotechnical causes, such as liquefaction. When water waves propagate over a non-cohesive seabed and interact with coastal structures, excess pore pressure can be generated, enabling the rise of two different types of

liquefaction (Nago et al., 1993). The "residual" liquefaction is caused by compression-relaxation cycles under wave crests and wave troughs, respectively. It generates shear stresses in the soil and the consequent buildup of pore water pressure that could exceed the value of the overburden pressure, making the soil grains totally unbound (Sumer, 2014). The "momentary" liquefaction occurs during the passage of wave troughs if the upward pore pressure gradient (strictly related to seepage forces) exceeds the initial vertical effective stress.

Kudella et al., (2006) carried out a series of experiments related to the generation of momentary and residual pore pressure in the seabed beneath a caisson breakwater, subjected to both pulsating and breaking wave loads. On the basis of their experiments, Kudella et al., (2006) showed that the transient (i.e. momentary) pore pressures in the seabed, beneath the caisson, were generated by the caisson motion. Moreover, these pore pressures are higher than the wave induced transient pore pressures in front of the caisson, for the same wave conditions. Therefore, the contribution of surface water waves to residual pore pressure generation was almost negligible. Anyway, the concept cannot be extended to the areas surrounding the structure. Indeed, Ye et al., (2015) found that for a composite breakwater poro-elastoplastic seabed foundations, the residual liquefaction potential in the zone far from the structure is greater than that in the zone near to the composite breakwater (see their Figure 15). The proposed work deals with rubble mound breakwaters with submerged berms. The knowledge of the potential structure failure due to liquefaction occurrences should hence include the effects of both residual and transient pore pressure generation.

However, the second part of this Thesis is focused on the evaluation of submerged berm configuration only upon momentary liquefaction occurrences. In the past decades, research studies have been carried out on the interaction between waves, seabed and structures (hereinafter referred to as WSSI). In this regard, Mase et al., (1994) and Hur et al., (2010) used the classic Biot's poro-elastic theory to investigate the seabed response around a composite caisson-type breakwater by using numerical tools.

Ulker et al., (2010), Ye et al., (2014) and Zhao et al., (2017) simulated the presence of a composite caisson-type breakwater in their numerical models, showing that the assessment of the consolidation process, in presence of marine structures, is essential for the liquefaction analysis.

All the aforementioned studies focused on WSSI. Although existing numerical models (e.g. Ye et al., 2015) are suitable for simulating the presence of submerged berms within the WSSI framework, none of the aforementioned studies considered the effects of submerged berms on the liquefaction phenomenon. Therefore, the aim of the present Thesis (within its second part) is to investigate the wave-induced soil response and momentary liquefaction probability around and beneath rubble mound breakwaters with (and without) submerged berms. A parametric study has been carried out by varying the berm configuration in terms of its length and its height, keeping constant the elastic properties of the soil, the water depth and the offshore regular wave conditions. This is to assess if the deployment of a submerged berm will provide improvements in terms of reduction of liquefaction probability, if compared to the case of straight sloped conventional breakwaters without a berm. The adopted rationale, based on a parametric-comparative study, makes reasonable the regular wave assumption, despite irregular waves always occur in the real ocean environments.

Under the random real wave assumption, the soil response to the wave-induced seabed pressure may be dissimilar from regular waves conditions. With the aim to evaluate how different could be the soil response in terms of liquefaction depths, the third part of the Thesis is focused on the investigation of random-wave-induced momentary liquefaction probability around and beneath rubble mound breakwaters with submerged berm. A comparison with representative regular wave results has been carried out.

1.1 THESIS OUTLINE

A brief overview of the Thesis is presented herein.

Chapter 2 deals with the hydraulic stability of rubble mound breakwaters with submerged berms.

It begins with the detailed description of conventional rubble mound breakwaters, including existing armor layer design criteria. Then, Section 2.3 describes the methodology of the research, explaining the employed strategy about the inclusion of the physical phenomena occurring when incident waves propagate on the berm, into well-established design criteria. Sections 2.4 and 2.5 illustrate the experimental and numerical investigations respectively. On a final note, Section 2.6 details and discusses the proposed design criterion, including a useful example calculation.

Chapter 3 is focused on the evaluation of the wave-induced soil response and momentary liquefaction probability around and beneath rubble mound breakwaters with (and without) submerged berm.

It starts with the description of wave-induced liquefaction, detailing the difference among residual and momentary liquefaction phenomena. Section 3.2 describes the methodology of the work and provides a literature review within the wave-structure-seabed interaction framework. Sections 3.3 and 3.5 illustrate the adopted numerical models and the numerical investigations as well, considering only regular wave conditions. In closing, Section 3.6 details the findings, explaining which submerged berm configuration could be intended as the best design choice to prevent the liquefaction phenomena, at least within the tested conditions.

Chapter 4 is aimed to evaluate the effects of random waves on the momentary liquefaction around and beneath rubble mound breakwaters with submerged berms.

It begins with the introduction to the topic, including also a literature review and underlining that only a few research studies considered the effect of random waves on the soil responses and liquefaction processes. Sections 4.3 and 4.4 describe the

carried out numerical investigations and the achieved results as well, specifying that, within the evaluation of momentary liquefaction occurrences, the usage of representative regular wave instead of irregular waves, could lead to an underestimation of the liquefaction depth, determining an unsafe design in the practice.

The concluding remarks of Chapter 5 close the Thesis.

2

THE ROLE OF SUBMERGED BERMS ON THE HYDRAULIC STABILITY OF RUBBLE MOUND BREAKWATERS

Before describing the topic on which the chapter is focused on, it is useful starting with a brief introduction to conventional rubble mound breakwaters, including existing armor layer design criteria. The succeeding section illustrate the methodology of the research,as well as the the experimental and numerical investigations, which have led to define the proposed stability formula, useful to evaluate the armor layer rock size for rubble mound breakwaters with submerged berms.

2.1 THE CONVENTIONAL RUBBLE MOUND BREAKWATER

Rubble mound breakwaters are widely used all around the world to deliver protection for coastal areas and harbors as well, from the concerted action of waves and currents. Their deployment takes a variety of forms, being used for defending beaches from erosion phenomena, but also for providing harbors tranquillity, etc.

Versatile in their usage, conventional rubble mound breakwaters could hence be characterized by variable geometry. Figure 2.1 represents a typical layout of conventional rubble mound breakwater cross-section.

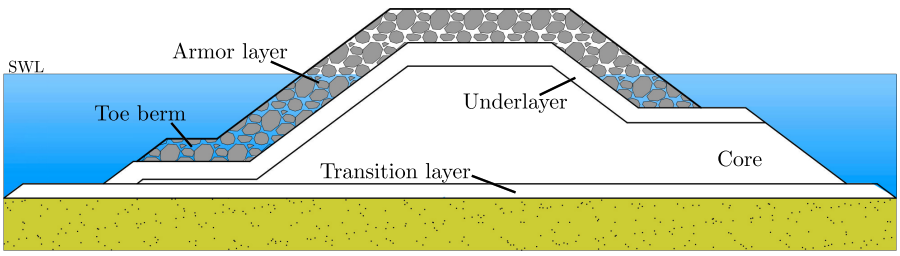

Figure 2.1: Typical cross section of conventional rubble mound breakwater.

The innermost part is referred to as the core, generally made with fine grain material such as quarry run. It has several functions to perform, as forming a satisfactory foundation for the underlayers and the armor layer as well. Moreover, it should provide a relatively impermeable barrier to the transmission of wave energy (e.g. Hedges, 1984).

As for the core, also the underlayers have to fulfill several requirements. They should act as filters to prevent the washing out of core material through the armor layer. Moreover, they should provide a temporary shield for the core, before the armor layer deployment.

The toe berm provides support to the armor layer and protects the structure from the damage due to the scour (van Gent and van der Werf, 2014).

The armor layer, being the outer seaward layer, must be stable against wave attacks during design conditions. In general, it is made up of rock stones, but it could be realized by deploying concrete elements in case heavier units are needed or if natural resources are not available. The serviceability of the structure mainly relies on the armor layer capability to remain stable during wave attacks.

In the next Section, several empirical methods for the armor unit size dimensioning are illustrated.

2.2 HYDRAULIC STABILITY OF BREAKWATERS: STATE OF THE ART

Many empirical methods for the armor unit size dimensioning, required for the stability under wave attacks, have been proposed in the last 60 years (CIRIA/CUR/CETMEF, 2007). In general, the stability number N_s is used to characterize the hydraulic stability. It is expressed as follows (Hald, 1998):

$$N_s = \frac{H_n}{\Delta D_{n50}} = Kf(\cdot) \tag{2.1}$$

where:

- H_n is the characteristic wave height;
- $\Delta = (\rho_r - \rho_w)/\rho_w$ is the relative submerged mass density, being ρ_r the mass density of the rocks and ρ_w the mass density of the sea water;
- $D_{n50} = (M_{50}/\rho_r)^{1/3}$ is the nominal diameter of the rocks in the armor, being M_{50} the median rock mass;
- K is an empirical coefficient;
- $f(\cdot)$ is a function of. The dot $(\cdot)$ is used in order to underline that different criteria with different parameters influences exist.

A very used formulation, expressed by Equation 2.2, is the Hudson formula (Hudson, 1959), based on the pioneering work of Iribarren, (1938):

$$\frac{H}{\Delta D_{n50}} = (K_D cot\alpha)^{1/3} \tag{2.2}$$

In the Equation 2.2, the empirical coefficient $K = K_D^{1/3}$ (K_D is equal to 3.5 and 4.0 for breaking and non-breaking waves, if rock armor layers are considered.) and $f(\cdot) = f(\alpha) = (cot\alpha)^{1/3}$, where α is the armor slope. The main advantage of Equation 2.2 is its simplicity. Nevertheless, many limitations mark it out. Indeed, the Hudson formula does not take into account the wave period or the storm duration and it was validated with only regular wave conditions.

To overcome the last limitation, USACE, (1975); 1984 proposed using $H = H_s = H_{1/3}$ and $H = H_{1/10}$, respectively.

Based on earlier work of Thompson and Shuttler, (1975), Van Der Meer, (1988) proposed Equations 2.3 to design armor rock

unit size, based on several tests performed at Delft Hydraulics, by considering irregular wave conditions.

$$\frac{H_s}{\Delta D_{n50}} = c_p P^{0.18} \left(\frac{S_d}{\sqrt{N}}\right)^{0.2} \xi_m^{-0.5} \qquad \text{for} \quad \xi_m < \xi_{mc} \tag{2.3a}$$

$$\frac{H_s}{\Delta D_{n50}} = c_s P^{-0.13} \left(\frac{S_d}{\sqrt{N}}\right)^{0.2} \sqrt{cot\alpha}\xi_m^{P} \qquad \text{for} \quad \xi_m > \xi_{mc} \tag{2.3b}$$

where:

- $c_p = 6.2$ and $c_s = 1.0$ are empirical coefficients;
- P is the permeability of the structure;
- $S_d = A_e/D_{n50^2}$ is the dimensionless armor damage;
- N is the number of waves;
- $\xi_m = tan\alpha/(2\pi H_s/gT_m^2)$ is the surf similarity parameter based on the mean period T_m, being H_s the significant wave height;
- $\xi_{mc} = (6.2P^{0.31}\sqrt{tan\alpha})^{1/(P+0.5)}$ is the critical breaker parameter, being α the armor slope.

With a reference to Equations 2.3 the empirical coefficients are:

- $K = C_p$ for $\xi_m < \xi_{mc}$
- $K = C_s$ for $\xi_m > \xi_{mc}$

whilst, $f(\cdot) = f(S_d, N, P, \xi, \alpha)$ is equal to:

- $P^{0.18} \left(\frac{S_d}{\sqrt{N}}\right)^{0.2} \xi_m^{-0.5}$ for $\xi_m < \xi_{mc}$
- $P^{-0.13} \left(\frac{S_d}{\sqrt{N}}\right)^{0.2} \sqrt{cot\alpha}\xi_m^{P}$ for $\xi_m > \xi_{mc}$

In shallow water, the distribution of individual wave height may significantly deviate from theoretical Rayleigh distribution and lower wave heights are likely to occur (Battjes and Groenendijk, 2000; Goda, 2010). Therefore, if the same offshore

conditions are considered, the stability increases (e.g. Van Der Meer, 2011; van Gent, 2013), i.e. the wave load decreases. Then, Van Der Meer, (1988) suggested using the 2% exceedance individual wave height ($H_{2\%}$) instead of the significant wave height. Then, for plunging ($\xi_m < \xi_{mc}$) and surging waves ($\xi_m > \xi_{mc}$), equations 2.3 become:

$$\frac{H_s}{\Delta D_{n50}} \frac{H_{2\%}}{H_s} = c_p^* P^{0.18} \left(\frac{S_d}{\sqrt{N}} \right)^{0.2} \xi_m^{-0.5} \qquad \text{for} \quad \xi_m < \xi_{mc} \tag{2.4a}$$

$$\frac{H_s}{\Delta D_{n50}} \frac{H_{2\%}}{H_s} = c_s^* P^{-0.13} \left(\frac{S_d}{\sqrt{N}} \right)^{0.2} \sqrt{cot\alpha} \xi_m^P \qquad \text{for} \quad \xi_m > \xi_{mc} \tag{2.4b}$$

It has to be stressed that in deep water, Equations 2.4 are equivalent to Equations 2.3, as $H_{2\%}/H_s = 1.4$ for the Rayleigh distribution and $c_p^* = 1.4c_p$ (and $c_s^* = 1.4c_s$).

In shallow water conditions, the value of the ratio $H_{2\%}/H_s$ can be estimated by applying methods aimed to describe the probability distribution of the individual wave heights (e.g. Battjes and Groenendijk, 2000).

For applications with very shallow foreshore, van Gent et al., (2004) proposed to modify Equations 2.4, on the basis of results from tests carried out by Smith et al., (2003) and additional physical tests in breaking and non-breaking wave conditions:

$$\frac{H_s}{\Delta D_{n50}} \frac{H_{2\%}}{H_s} = c_p^* P^{0.18} \left(\frac{S_d}{\sqrt{N}} \right)^{0.2} \xi_{s-1,0}^{-0.5} \qquad \text{for} \quad \xi_m < \xi_{mc} \tag{2.5a}$$

$$\frac{H_s}{\Delta D_{n50}} \frac{H_{2\%}}{H_s} = c_s^* P^{-0.13} \left(\frac{S_d}{\sqrt{N}} \right)^{0.2} \sqrt{cot\alpha} \xi_{s-1,0}^P \qquad \text{for} \quad \xi_m > \xi_{mc} \tag{2.5b}$$

Equations 2.5 are similar to Equations 2.4, but the spectral period $T_{m-1,0}$ is used instead of the mean period T_m.

2.3 METHODOLOGY

This Section aims to describe a new stability formula to be used when relative low berms are foreseen at the toe of conventional rubble mound breakwater.

The strategy is to include the physical phenomena occurring when incident waves propagate on the berm, thus affecting the wave loads on the upper rock slope, into well established design criteria (Van Der Meer, 1987; 1988).

The same methodology was adopted by van Gent, (2013), which proposed to apply two coefficients to the formulations of van Gent et al., (2004), (see Equations 2.5), in order to take into account the role of relative high berms upon the damage suffered by the upper rock slope of conventional rubble mound breakwaters.

In particular, to take into account the vertical position of the berm, van Gent, (2013) proposed the following coefficient:

$$\gamma_{pos} = \left[0.25 + 0.125 cot\alpha \left(1 + \frac{h_b}{H_s}\right)\right]^5 \qquad with\ 0 \leq \gamma_{pos} < 1 \tag{2.6}$$

where α is the armor slope, H_s is the significant wave height at the toe of the berm and h_b is the water depth on the berm (see Figure 2.2).

The influence of the berm length B on the stability is given by:

$$\gamma_{berm} = 1 - 0.15\xi_{m-1,0}\left(\frac{B}{H_s}\right)^{0.3} \tag{2.7}$$

The resulting stability formulae, written in terms of the damage parameter S_d, read as follows:

$$S_d = \gamma_{berm}\gamma_{pos}\left(\frac{1}{c_p^*}\frac{H_{2\%}}{\Delta D_{n50}}\xi_{m-1,0}^{0.5}P^{-0.18}N^{0.1}\right)^5 \tag{2.8a}$$

$$S_d = \gamma_{berm}\gamma_{pos}\left(\frac{1}{c_s^*}\frac{H_{2\%}}{\Delta D_{n50}}\xi_{m-1,0}^{0.5}P^{0.13}N^{0.1}\sqrt{cot\alpha}\right)^5 \tag{2.8b}$$

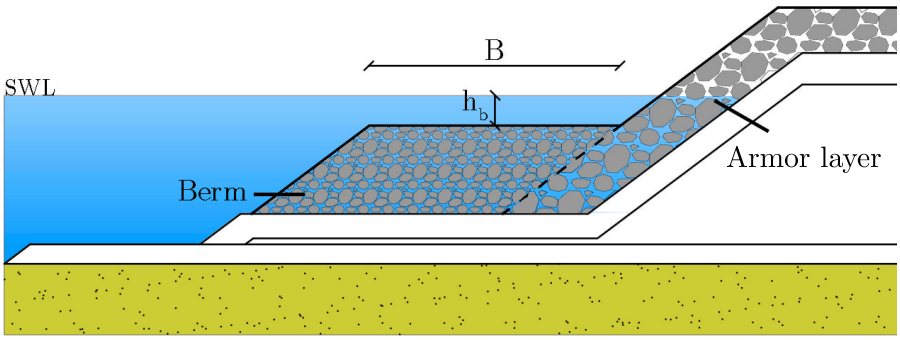

Figure 2.2: Geometric berm parameters as defined by van Gent., 2013.

Now, the strategy of the proposed formulation is to include, in Equations 2.4, the role of submerged berms on the damage parameter S_d. The ratio $H_{2\%}/H_s$ represents the statistical measure of individual wave height at the toe of the breakwater. For this reason, it is useful to rename the variables by introducing the suffix "T" (i.e. $H^T_{2\%}/H^T_s$). If a berm is present, it is also necessary to consider the wave features over the berm itself (i.e. $H^B_{2\%}/H^B_s$), where the suffix "B" indicates that the wave heights have to be estimated at the toe of the armor layer over the berm (see Figure 2.3).

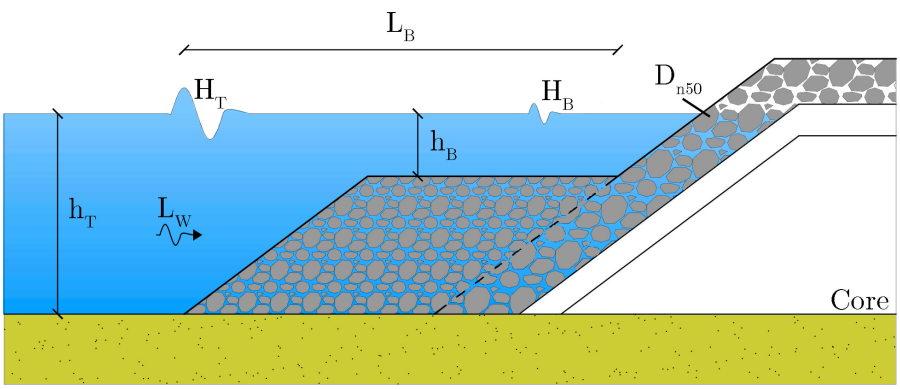

Figure 2.3: Geometric parameters definition of conventional rubble mound breakwaters with a berm. The core runs below the berm only for considerable values of berm height.

In order to continue the practical use of the ratio $H^T_{2\%}/H^T_s$, Equations 2.4 have to be modified by expressing the wave fea-

tures on the berm as a function $f(\cdot)$ of the wave features at the toe:

$$H_{2\%}^{B} = f\left(H_{2\%}^{T}\right) \tag{2.9}$$

Equation 2.9 is the formal core of the method proposed herein.

From a practical point of view, the function $f(\cdot)$ can be simply expressed as follows:

$$H_{2\%}^{B} = \left(\frac{H_{2\%}^{B}}{H_{2\%}^{T}}\right) H_{2\%}^{T} \tag{2.10}$$

Basically, it can be observed that the term between brackets depends on the configuration of the berm (i.e. its length, L_B, and the water depth over the berm, h_B, see Figure 2.3), as well as on the water depth at the toe (h_T) and on the incident wave length (L_W, evaluated on the basis of the incident peak period, as the influence of the berm is related to the travel distance):

$$\gamma = \left(\frac{H_{2\%}^{B}}{H_{2\%}^{T}}\right) = f(L_B, h_B, h_T, L_W) \tag{2.11}$$

It has to be noted that the berm length L_B is defined as the horizontal distance of the armor toe from the berm one, whilst van Gent, 2013 defined the berm length (i.e. B, see Figure 2.2) as the extension of the horizontal part of the berm. The definition used herein is intended to represent the role of the whole berm on the wave propagation.

By using Equations 2.10 and 2.11, Equations 2.4, written in terms of the damage parameter, read as follows:

$$N_s = \frac{c_p^*}{\gamma}\left(\frac{S_d}{\sqrt{N_w}}\right)^{0.2} \xi_m^{-0.5} P^{0.18} \frac{H_s^T}{H_{2\%}^T} \qquad \text{for} \quad \xi_m \leq \xi_{mc} \tag{2.12a}$$

$$N_s = \frac{c_s^*}{\gamma}\left(\frac{S_d}{\sqrt{N_w}}\right)^{0.2} \xi_m^{P} \sqrt{tan\alpha} P^{-0.13} \frac{H_s^T}{H_{2\%}^T} \qquad \text{for} \quad \xi_m > \xi_{mc} \tag{2.12b}$$

Hence, the presence of the berm may be considered by modifying the significant wave height at the toe, by using the function γ expressed by Equation 2.11.

Equations 2.12 may be expressed also in terms of the damage parameter S_d:

$$\frac{S_d}{\sqrt{N_W}} = \left(\frac{1}{c_p^*} \xi_m^{0.5} \frac{\gamma H_s^T}{\Delta D_{n50}} P^{-0.18} \frac{H_{2\%}^T}{H_s^T} \right)^5 \qquad \text{for} \quad \xi_m \leq \xi_{mc} \tag{2.13a}$$

$$\frac{S_d}{\sqrt{N_W}} = \left(\frac{1}{c_s^*} \xi_m^{-P} \sqrt{cot\alpha} \frac{\gamma H_s^T}{\Delta D_{n50}} P^{0.13} \frac{H_{2\%}^T}{H_s^T} \right)^5 \qquad \text{for} \quad \xi_m > \xi_{mc} \tag{2.13b}$$

Equations 2.12 or 2.13 are the practical core of the method proposed herein.

If there is not any berm, Equations 2.12 are equivalent to Equations 2.4 as $\gamma = 1$ (i.e. $H_{2\%}^B = H_{2\%}^T$). When a berm is present, then $\gamma \neq 1$.

From a qualitative point of view, it could be observed that the stronger the influence of the berm on the incident waves (i.e. the lower the water depth h_B and the higher the berm length L_B), the lower the expected value of γ (i.e. $\gamma < 1$).

In order to make useful Equations 2.12 or 2.13, an empirical method aimed to provide γ as a function of the berm length (L_B), the water depth over the berm (h_B), the water depth (h_T) and the wave length (L_W) at the toe is needed. By using the Buckingham Pi Theorem (e.g. Cengel and Cimbala, 2006), Equation 2.11 reads:

$$\gamma = f\left(\frac{L_B}{L_W}, \frac{h_B}{h_T} \right) \tag{2.14}$$

To find the dependence of γ upon the dimensionless groups L_B/L_W and h_B/h_T, a long series of observations should be collected and analyzed. As an extensive experimental investigation is time-consuming, numerical tools have been employed, by using an ad-hoc experimental database for validation purposes.

The succeeding Section details the experimental and numerical investigations aimed to define the function $f(\cdot)$ of Equation 2.14.

2.4 EXPERIMENTAL INVESTIGATION

Experimental tests have been performed in a wave flume (45 m long, 1.5 m wide and 2 m high) at the Environmental and Maritime Hydraulic Laboratory (LIAM) of the University of L'Aquila. The flume bottom is horizontal. It was filled with sand in order to reproduce the correct bathymetry (see Figure 2.4). The flume is made of reinforced concrete. A 10 m long wall is made of transparent glass to allow the direct visualization of the experimental model.

The wave flume is equipped with a piston type wave generator (stroke 0.75 m) that can be used to generate any sea state, i.e. regular and irregular waves as well, characterized by target spectra (i.e. JONSWAP, PM, etc ...). Figure 2.4 shows the wave generator components and the glass wall of the wave flume. The wave generator system is equipped with an Active Reflection Compensation (hereinafter referred to as ARC) system. The ARC system allows reproducing the real life boundary conditions, where the waves reflected by the structure are radiated offshore. In the laboratory conditions, the wave paddle is located at the seaward boundary and the waves are not allowed to radiate offshore. Hence, the incident spectra rapidly deviate from the target ones. In order to absorb the reflected waves, the ARC system is then required. It is based on the real-time estimation of the reflected waves in the time domain. Basically, a counter-phase wave component, interfering with the reflected wave, is generated, while the latter is absorbed. On the basis of this principle, some wave gauges are placed in front of the wave paddle at a known distance (x>3h, being h the water depth, i.e. outside the theoretical nearfield) and time domain reflection analysis (based on Finite Impulse Digital Filters, see Frigaard

and Brorsen, 1995) is performed in real time, and the wave paddle motion is corrected.

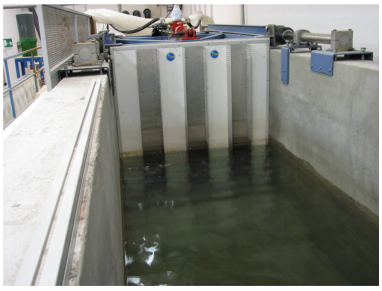

(a) Wave paddle

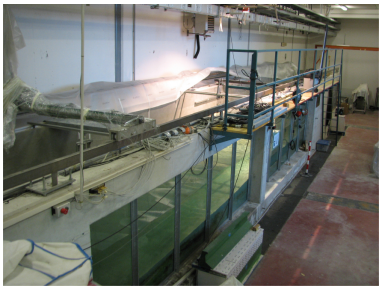

(b) Wave flume glass wall

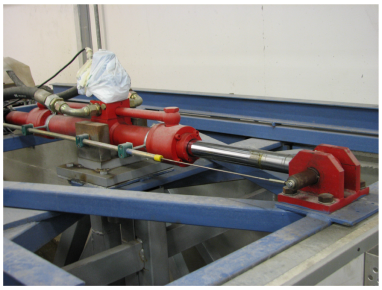

(c) Wave generator

(d) Hydraulic power supply

Figure 2.4: The wave flume and the wave generator components

The physical model reproduces a conventional rubble mound breakwater with a submerged berm. The foreshore is reproduced as a 7.0 m long mild slope (1V:1000H) connected to the flume bottom by means of a 8.0 m long steel ramp (slope equal to 1V:20H). With reference to the sketch of Figure 2.3, the tested configurations are characterized by a berm length in the range (0.15 ÷ 0.75) m, a water depth on the berm in the range (0.03 ÷ 0.34) m, a wave length at the toe of the berm in the range (1.98 ÷ 3.93) m.

The combination of the parameters led to dimensionless groups used by Equation 2.14 in the ranges (0.134 ÷ 0.670) and (0.091 ÷ 0.691) for L_B/L_W and h_B/h_T respectively.

2.4.1 *Scaling*

The model has been intended to reproduce a typical prototype condition at a Froude scale 1:20 (λ = 20). The breakwater model has been placed on a sand bottom in the flume (d_{50} = 0.12 mm). The Froude criterion allow conserving the Froude number among the model and prototype scale, whilst the Reynolds number is not reproduced. Indeed, when a rubble mound breakwater is built at laboratory scale, the Froude criterion is able to reproduce only the wave propagation, mainly governed by gravity forces. The role of other forces, such as friction, elasticity and surface tension are hence neglected. In case of rubble mound structures, the most critical effects are mainly due to the incorrect reproduction of viscous effects (i.e. governed by the Reynolds number) within the armor and filter layers, as well as into the core material.

In order to partially reproduce the physical phenomena influenced by the Reynolds number, i.e. with the view to reproduce the correct flow regime into the armor and the filter layer, it is shown that the reproduced Reynolds number has to be higher than 30000 (Frostick et al., 2011). Reynolds number for the armor elements can be defined as follows:

$$Re = \frac{D_n \sqrt{gH_s}}{\nu} > 30000 \tag{2.15}$$

where D_n is the natural element diameter, H_s is the significant wave height, g is the gravitational acceleration and ν is the water kinematic viscosity. Equation 2.15 has been used to define the minimum value of D_{n-min} in order to correctly reproduce the regime flow into the armor layer:

$$D_{n-min} = \frac{30000\nu}{\sqrt{g(H_{s-min})_m}} \tag{2.16}$$

being $(H_{s-min})_m$ the minimum (observed during the experimental tests) value of significant wave height at model scale. Equation 2.16 yields:

$$D_{n-min} = 38mm \tag{2.17}$$

As far as the reduction of the core material is concerned, the condition imposed by Equation 2.17 cannot be respected in general, then a different scaling procedure (e.g. Burcharth and Andersen, 1995; Burcharth et al., 1999) must be followed with a view to reproduce the correct filtration fluid flow regime into the structure. Table 2.1 synthesizes the scaling factor of the investigation.

Parameter	**Scaling factor**	**Model to prototype scaling factor**	**Prototype to model scaling factor**
Length	λ	20.00	0.0500
Velocity	λ_v	4.47	0.2236
Time	λ_t	4.47	0.2236
Volume	λ_V	9148.89	1.09E-04
Grain Size	λ_g	20.91	0.0478

Table 2.1: Synthesis of the scaling factors

Armor layer

The diameter of the elements $(D_{50})_p$ and its volume $(V_{50})_p$ at prototype scale (subscript "p"), has been scaled at model size (D_{50_m} and V_{50_m}) by considering the volume reduction factor λ_V, obtained on the basis of Hudson formula (Hughes, 1993). To reproduce the same damage factor, the volume reduction factor λ_V has been related to the length reduction factor λ, through the following relationship:

$$\lambda_V = \left[\lambda \left(\frac{\rho_s/\rho_{fw} - 1}{\rho_s/\rho_{sw} - 1}\right)\right]^3 \tag{2.18}$$

where ρ_s(=2650 kg/m^3), ρ_{sw}(=1028 kg/m^3) and ρ_{fw}(=1000 kg/m^3) are the material, salt water and fresh water densities, respectively. The volume reduction factor is:

$$\lambda_V = 9148.89 \tag{2.19}$$

For stability tests, a $(D_{50})_p$ = 1.10 m (2-5 t) has been reproduced. By considering the same shape factor at prototype and model scale, the $(D_{50})_m$ is:

$$(D_{50})_m = 52\ mm \tag{2.20}$$

The grading of the armor material has been selected by following the CIRIA/CUR/CETMEF, (2007) guidelines. The model scale allows to correct reproduce the regime flow into the armor layer as the smaller deployed diameter (40 mm) is greater than the value of D_{n-min} (38 mm) , see Equation 2.17.

The measured density and weight of the elements used to build the armor layer, along with the measured total volume of the armor layer, have been used to estimate the experimental (volumetric) porosity, equal to 0.39.

Leeward armor layer and berms

The leeward armor layer as well as the seaward and leeward berms have been scaled to model size by using the same procedure illustrated for the seaward armor layer.

Core and filter layers

Due to the importance of correctly reproduce the filtration phenomena rather than the stability, a different scaling procedure has been used for filter and core layers. Then, the method proposed by Burcharth et al., (1999) has been adopted. The strategy is to estimate the model grain size for which the characteristic velocity into the core is Froude scaled, with respect to the proto-

type conditions. In the followings, the method is briefly detailed. Into the core, the maximum dynamic pressure distribution can be expressed as follows:

$$p_{max} = p_{0-max} exp\left(-\frac{2\pi}{L'}\delta x\right) \tag{2.21}$$

in which δ is a damping coefficient, L' is the wave length within the core, p_{0-max} is the reference pressure and x is the distance measured from the beginning of the core (interface between the filter layer and the core) of the filter layer (interface between the seaward armor layer and the filter layer).

The damping coefficient can be estimated by means of the following relationship:

$$\delta = 0.0141\frac{L_p^2\sqrt{n}}{bH_s} \tag{2.22}$$

where n is the porosity, L_p is the incident wave length computed with respect to the peak wave period, H_s is the significant wave height and b is the length of the core or the filter layer.

The wave length L' can be estimated as follows:

$$L' = \frac{L_p}{\sqrt{\xi}} \tag{2.23}$$

with $\xi \simeq 1.4 \div 1.5$.

Hence, the hydraulic gradient I_x can be expressed as follows:

$$I_x(x,t) = -\frac{\pi H_s}{L'} exp\left(-\frac{2\pi}{L'}\delta x\right)\left[\delta cos\left(\frac{2\pi}{L'}x + \frac{2\pi}{T_p}t\right) + \right. \\ \left. + sin\left(\frac{2\pi}{L'}x + \frac{2\pi}{T_p}t\right)\right] \tag{2.24}$$

If the hydraulic gradient is known, the velocity within the core (or the filter layer) can be achieved by solving the following algebraic equation:

$$I_x = \alpha\left(\frac{1-n}{n}\right)^2 \frac{\nu}{gD_{50}^2}\left(\frac{U}{n}\right) + \beta\left(\frac{1-n}{n}\right)\frac{1}{gD_{50}^2}\left(\frac{U}{n}\right)^2 \tag{2.25}$$

where α and β are coefficients that depend upon the Reynolds number and the grain shape as well. Burcharth and Andersen, (1995) suggested α = 0 and β = 3.6 at prototype scale, and α = 900.0 and β = 2.5 at model scale.

The method can be applied by computing a characteristic value of the velocity $\bar{U}_p$ within the core (or the filter layer), at prototype scale. Burcharth et al., (1999) suggested estimating the characteristic velocity $\bar{U}_p$ within the core, as the arithmetic mean of the velocity occurring at t = 0.0-0.1-0.2-0.4-0.5 T_p, at x = 0.0-0.25-0.50b, where b is the core (or filter layer) length at the water level. Once $\bar{U}_p$ has been estimated, its value at model scale $\bar{U}_m$ can be obtained by:

$$\bar{U}_m = \frac{\bar{U}_m}{\sqrt{\lambda}} \tag{2.26}$$

The scaling factor λ_f for the core (or the filter layer) material can be estimated by computing a characteristic value of the velocity $\bar{U}_m$ within the core (or the filter layer) at model scale, with varying grain size D_{50}. It has to be stressed that the scaling factor depends upon the wave characteristic, then a representative value has to be selected. For the filter layers (sea- and lee-ward) scaling factors are almost equal to λ (=20). For the core material, two different gradings (c_1 and c_2) have been reproduced during the investigations. The first one (c_1) is characterized by D_{50} = 0.34 m, for which a scaling factor of 17.05 has been estimated. The second grading (c_2) is characterized by D_{50} = 0.065 m (finer if compared to c_1) and the scaling factor has been estimated to be equal to 7.2. It can be observed that the method aims at scaling the grain size in order to reproduce the characteristic velocity within the core, following the Froude criterion: the finer the grains, the lower the scaling factor (i.e. the heavier at model scale).

2.4.2 *Experimental tests*

With a view to estimating reflection and transmission coefficients, and to tune the ARC system as well, the free surface elevations time series have been collected through a series of nine wave gauges deployed along the wave flume (see Figure 2.7). The sample acquisition frequency has been set to 100 Hz at model scale, i.e. sample time equal to about 0.05 s at prototype scale. The gauges have been arranged in groups of three in order to apply standard reflection analysis (e.g. Mansard and Funke, 1980)

During each experimental test, about 2000 waves have been generated. The damage suffered by the armor layer has been estimated by counting the extracted elements (e.g. Herrera et al., 2017; Vidal et al., 2004) within the frame of standard digital image analysis. The latter has been visually performed on the basis of rectified pictures comparison. In particular, the analysis has been carried out for small areas, by analyzing the whole breakwater. To estimate the displaced elements, the stones of the armor layer were painted with different colors (see Figure 2.5 as an example).

Figure 2.5: The experimental breakwater during the investigation.

At the end of each test run, the number N_{mov} of elements moved for a distance greater than D_{50} has been counted. N_{mov} has been estimated as the sum of elements N_{ext} extracted from the armor layer and of elements N_{disp} displaced of a quan-

tity greater than D_{50} but stayed within the double layer of the primary armor. Figure 2.6 illustrates the difference between extracted and simply displaced elements.

Two usual methods available in literature have been followed to quantify the observed damage:

1. the total number N_{mov} of moved elements has been used to estimate a damage percentage: $D = N_{mov}/N_{tot}$, where N_{tot} is the number of elements forming the armor layer in the reference area. The cumulative damage percentage Dd, at the end of a single test run, has been estimated as the sum of incremental damages, calculated in the previous test runs;

2. the number N_{ext} of elements extracted from the armor layer, has been used to evaluate the average (over the breakwater width W) value of transversal eroded area A_e (e.g.):

$$A_e = \frac{N_{ext} D_{50}^3}{(1 - n_v)W} \tag{2.27}$$

where n_v is the (volumetric) porosity of the armor layer. The variation of the porosity has been neglected during the experimental tests (Herrera et al., 2017). The average eroded area can be used to estimate the observed damage parameter S_d:

$$S_d = \frac{A_e}{D_{50}^2} = \frac{N_{ext} D_{50}}{(1 - n_v)W} \tag{2.28}$$

The cumulative damage parameter S_d, has been estimated by comparing the eroded area, at the end of the single test run, with the initial, undeformed cross section.

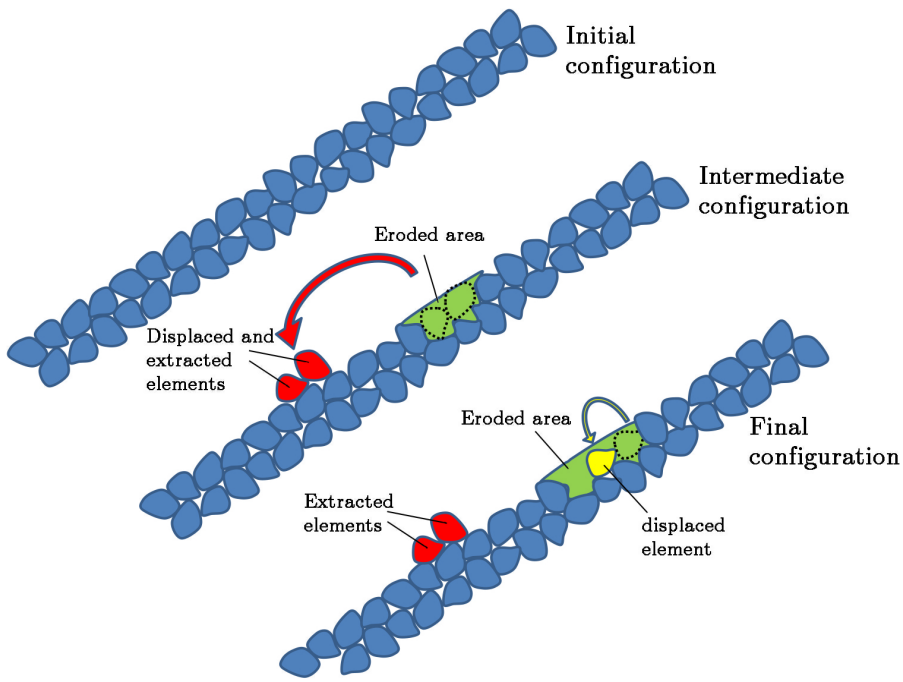

Figure 2.6: Sketch aimed at illustrating the difference between extracted and displaced elements.

2.5 NUMERICAL INVESTIGATION

2.5.1 *The numerical model*

The numerical model SWASH has been used to parametrically compute the wave features on the breakwater berm. It is an open-source, phase resolving numerical model for simulating non-hydrostatic, free surface, rotational flows (Zijlema et al., 2011).

The governing equations solved by the model are the shallow water equations, including a non-hydrostatic pressure term that can be derived from the incompressible Navier-Stokes equations.

In the research described herein, the numerical model has been employed by using three terrain-following layers in the vertical direction in the one-dimensional case. Then, the layer-integrated continuity equation for layer $1 \leq k \leq K$ ($K = 3$) reads as follows (e.g. Zijlema and Stelling, 2005):

$$\frac{\partial h_k u_k}{\partial x} - u \frac{\partial z}{\partial x}\bigg|_{z_k-1/2}^{z_k+1/2} + w_{k+1/2} - w_{k-1/2} = 0 \tag{2.29}$$

where x is the horizontal coordinate, h_k is the thickness of the layer k, z is the elevation of the interface between two layers (being $z - k - 1/2$ the interface between the layer k and the layer $k+1$), u is the layer-integrated horizontal velocity, $w_{k\pm1/2}$ is the vertical velocity at the interfaces between two layers.

The layer-integrated horizontal momentum equation reads as follows:

$$\begin{aligned} &\frac{\partial h_k u_k}{\partial t} + \frac{\partial h_k u_k^2}{\partial x} + \bar{u}^z_{k+1/2}\omega_{k+1/2} - \bar{u}^z_{k-1/2}\omega_{k-1/2} + \\ &+ g h_k \frac{\partial \xi}{\partial x} + \frac{\partial h_k \bar{q}^z_k}{\partial x} - q_{k+1/2}\frac{\partial z_{k+1/2}}{\partial x} + q_{k-1/2}\frac{\partial z_{k-1/2}}{\partial x} = 0 \end{aligned} \tag{2.30}$$

where t is the elapsed time, $\bar{u}^z_{k\pm1/2}$ is the horizontal velocity estimated at the layer interfaces $z_{k\pm1/2}$, $\omega_{k\pm1/2}$ is the vertical velocity relative to layer interfaces $z_{k\pm1/2}$ (defined as the difference between the vertical velocity along the streamline and the vertical velocity along the interface), g is the gravitational acceleration, ξ is the free surface elevation, $q_{k\pm1/2}$ is the non-hydrostatic pressure defined at the layer interfaces, $\bar{q}^z_k$ is the arithmetic mean of the non-hydrostatic pressure at the layer interfaces $z_{k\pm1/2}$.

The layer-integrated vertical momentum equation reads as follows:

$$\begin{aligned} &\frac{\partial h_{k+1/2} w_{k+1/2}}{\partial t} + \frac{\partial h_{k+1/2}\bar{u}^z_{k+1/2} w_{k+1/2}}{\partial x} + \bar{w}^z_{k+1}\bar{\omega}^z_{k+1} + \\ &\qquad - \bar{w}^z_k \bar{\omega}^z_k + 2\bar{q}^z_k = 0 \end{aligned} \tag{2.31}$$

where $h_{k+1/2}$ is the arithmetic mean of the layer thicknesses h_k and h_{k+1}, $\bar{w}^z_{k(+1)}$ is the arithmetic mean of the vertical velocities at the layer interfaces $z_{k(+1)\pm1/2}$, $\bar{\omega}^z_{k(+1)}$ is the arithmetic mean of the vertical velocities relative to the layer interface at the layer interfaces $z_{k(+1)\pm1/2}$.

For the details of numerical procedures and boundary conditions, the reader is referred to Zijlema and Stelling, (2008); Zijlema and Stelling, (2005) and Smit et al., (2013).

2.5.2 *Model validation*

A computational domain describing prototype dimension has been considered for validation purposes (see Figure 2.7). It has reproduced the experimental wave flume (see Section 2.4) intended as Froude scaled with a model-to-prototype length ratio rqual to 20.

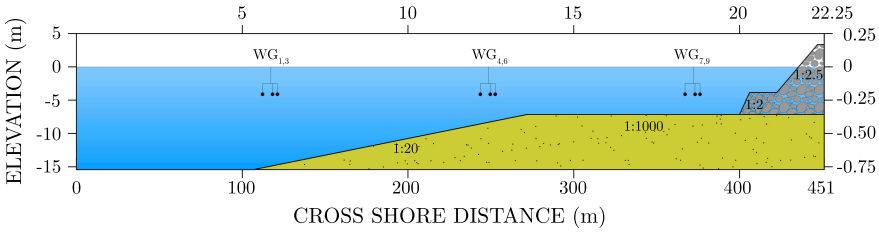

Figure 2.7: Sketch of the experimental layout. Wave gauges deployed along the flume are referred to with the symbol "WG". Bottom and left axes refer to prototype dimensions if a model-to-prototype scale ratio equal to 20 is considered. Upper and right axes refer to model dimensions.

A series of preliminary numerical simulations was performed at model and prototype scales and the results compared to observed values. The performance of the numerical model to reproduce the experimental findings was found to be not significantly sensitive to the scale of the simulations and it was preferred to perform the simulations at prototype scale, i.e. the same scale at which the numerical model is intended to be used.

The one-dimensional domain has been discretized by a constant horizontal spacing $\Delta x = 0.5$, in order to ensure a sufficient number of grid points per wave length within the range $80 \div 160$ (e.g. The SWASH team, 2017)

In order to properly describe wave dispersion also in the offshore zone, where shallow water conditions do not apply, a fixed number of three terrain-following layers in vertical direction has been selected, each of them characterized by equal thickness between the bottom and the moving free surface.

A porosity layer has been placed inside the computational domain to simulate the presence of the rubble mound breakwater in terms of its reflection effects. In particular, a volumetric

porosity values of 0.3 and 0.4 have been used for the berm and the armor layer respectively.

Moreover, to solve the governing equations, appropriate initial and boundary conditions have been imposed at the boundaries of the computational grid.

In this regard, a still water level has been applied as initial condition for all the numerical tests.

A water level time series condition has been imposed at the offshore side of the computational domain as a weakly reflective boundary. This provides that target waves are generated at this boundary, while reflected waves from onshore are radiated. The time series of surface elevation have been derived synthesizing Jonswap spectra (see Figure 2.8), varying accordingly to the offshore synthetic wave parameters (i.e. spectral wave height and peak period) of the considered sea state.

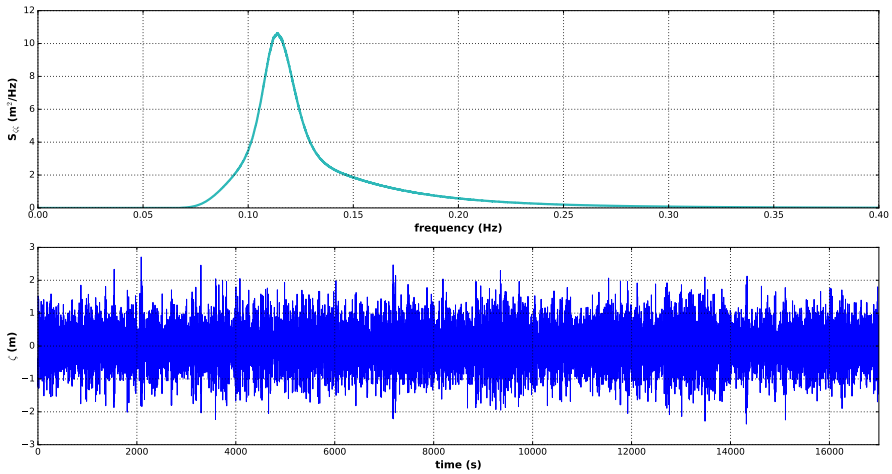

Figure 2.8: Upper panel: Jonswap spectrum ($\gamma = 3.3$) resulting from H_{m0} = 2.5 and T_p = 8.8. Lower panel: Synthesized surface elevation time series.

The Sommerfeld radiation condition has been applied to the onshore side of the numerical domain. As suggested by Suzuki et al., (2017), the non-hydrostatic pressure term has been applied with a Keller-box scheme, which has significant influence on the wave transformation. Adaptive time step has been employed by respecting the Courant-Friedrichs-Lewy (CFL) condition.

H_{m0} (m)	T_p (s)	h_T (m)	h_B (m)	L_B (m)	L_W (m)
2.5	8.8	7.0	4.0	15.0	68.5
2.5	8.8	9.7	6.7	15.0	78.6
3.0	8.8	9.7	6.7	15.0	78.6
2.5	8.8	6.0	3.0	15.0	64.0
2.3	7.3	6.0	3.0	15.0	51.7
2.0	6.0	5.5	2.5	15.0	39.5

Table 2.2: Wave parameters (offshore spectral wave height H_{m0}, peak wave period T_p, wave length at the toe of the berm L_W) and berm configuration (berm length L_B, water depth at the toe of the berm h_T and over the berm h_B) used to validate the numerical model.

Table 2.2 synthesizes the offshore synthetic wave parameters and the breakwater configuration used during the validation phase.

Figure 2.9 shows the comparison of modeled individual total wave features against observed values for one of the validation tests (H_{m0} = 2.3 m, T_p = 7.3 s, h_T = 6.0 m, h_B = 3.0 m; similar results have been achieved for all other tests).

The difference of the 2% exceedance wave crests and troughs computed and observed are relatively small (not higher than about 10%), as the differences in terms of maximum and minimum individual wave elevations and of significant wave height are.

A deeper knowledge may be gained by looking at the whole Empirical Probability Distribution Function (hereinafter referred to as EPDF) of the individual wave crests and troughs. The inspection of the EPDFs Q-Q Plots of the computed and observed wave crests and troughs (see Figure 2.10) reveals that the numerical model is able to catch their probability distribution satisfactorily even if the higher the quantiles, the higher the deviation (shaded areas refers to $\pm$ 10 % error).

The validation of the model is confirmed by looking at at the shapes of the energy density spectra. In particular, Figure 2.11 shows the energy density spectra of the total water surface

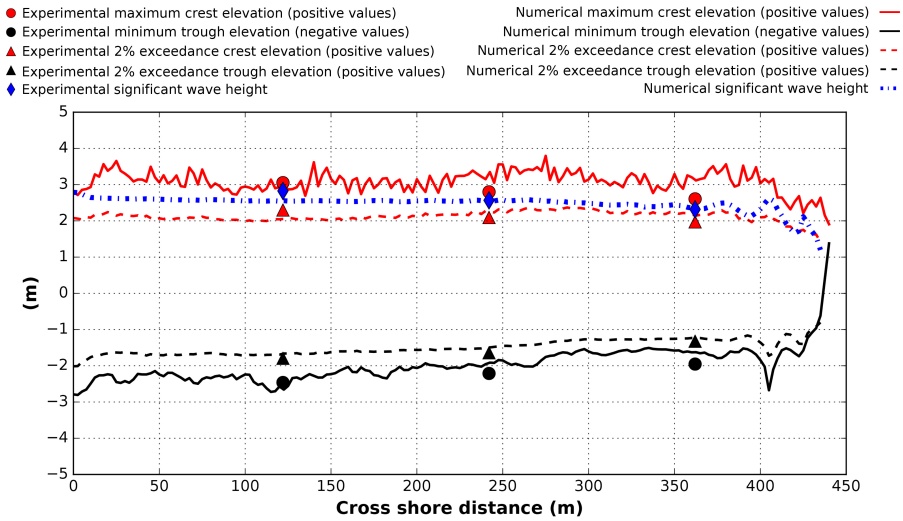

Figure 2.9: Spatial distribution of the 2% exceedance individual wave crests (positive values) and troughs (negative values) numerically computed (dashed lines) and experimentally observed (triangular markers); the maximum crest and minimum trough elevations are depicted (circular markers and continuous lines); also the significant wave height is shown in the plot (diamonds and dash dot line)

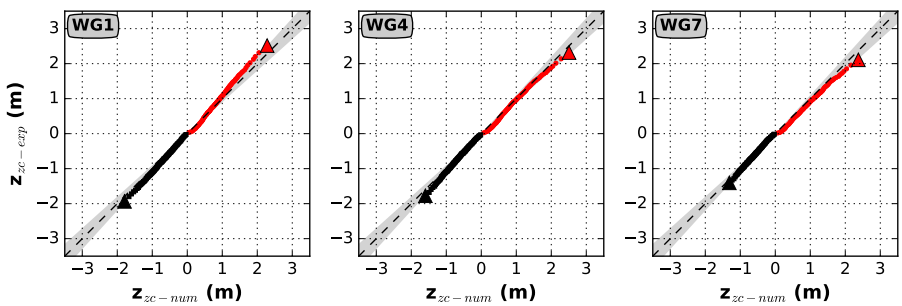

Figure 2.10: Q-Q Plots of the observed (z_{zc-exp}) and computed (z_{zc-num}) EPDFs of individual wave crests and troughs; from left to right, the diagrams refer to wave gauges WG1, WG4 and WG7 (see Figure 2.7); shaded areas depict the $\pm$ 10% error; triangular markers refer to the same values of the Figure 2.9.

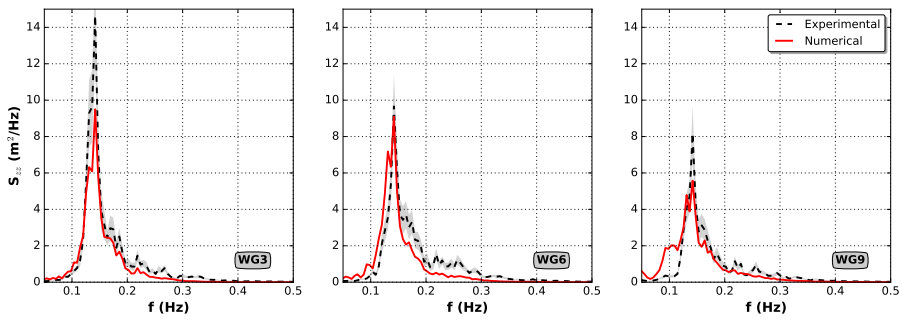

Figure 2.11: Wave energy density spectra of the observed total water levels (dashed lines) and of the computed total water levels (continuous lines); from left to right, the diagrams refer to wave gauges WG3, WG6 and WG9 (see Figure 2.7). Shaded areas indicate the standard errors

elevation (i.e. due to the superposition of incident and reflected components).

On the other hand, Figure 2.12 shows energy density spectra of the incident and reflected waves, estimated by employing standard methods (e.g. Mansard and Funke, 1980). Spectral results inspection reveals that during the propagation toward the breakwater, the spectral band tends to spread due to the effects related to the restricted depth-to-height ratio and to the wave breaking. At the offshore boundary of the ramp (i.e. at the location of wave gauges WG1-WG2-WG3), computed and observed spectra are almost similar. As the waves propagate to the foreshore (i.e. at the locations of wave gauges WG4-WG5-WG6) the computed incident spectrum shows lower energy in the high frequency band (i.e. for frequencies larger than the peak one) than the observed one. Once the waves reach the offshore boundary of the berm (i.e. at the locations of wave gauges WG7-WG8-WG9), the computed incident spectrum shows larger energy in the low frequency band and lower energy in the high frequency band than the observed one.

The reliability of the mean spectral period $T_{m-1,0}$ estimation is consistent with the results obtained by Suzuki et al., (2017): the error between observed and computed mean spectral period increases from offshore (about 8.8%) up to the shallow zone (about 20.5%) with the computed values higher than the observed ones.

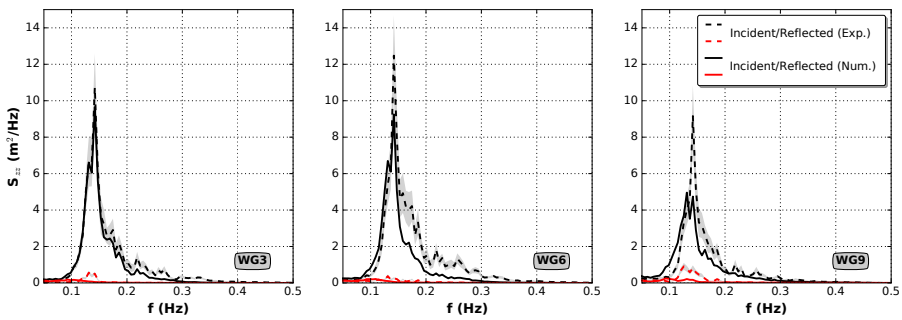

Figure 2.12: Incident (higher values) and reflected (lower values) wave energy density spectra of the observed water levels (dashed lines) and of the computed water levels (continuous lines) estimated by means of the standard method proposed by Mansard and Funke (1980)); from left to right, the diagrams refer to the locations of wave gauges WG3, WG6 and WG9 (see Figure 2.7). Shaded areas indicate the standard errors

2.5.3 *Numerical results*

With the aim to provide stability formulae that take into account the presence of submerged berms, several tests have been carried out by using the numerical model, validated as described in the previous Section.

Figure 2.13 shows a generic computational domain. In order to minimize the number of numerical simulations, the domain has been implemented without the armor layer.

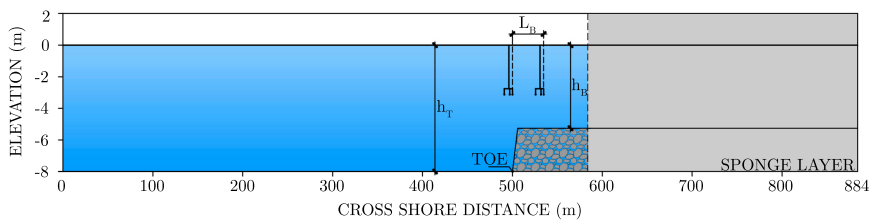

Figure 2.13: Sketch of the computational domain used to catch the influence of the berm on the incident water wave propagation. The same symbols used to indicate experimental wave gauges are used to indicate the locations where the numerical results have been extracted.

The results of reflection analysis did not differ significantly from the results obtained without the armor layer. Then, for each berm height (i.e. for each value of the water depth h_B over

the berm), a series of reflection analysis have been performed at different horizontal distance far from the toe of the berm (i.e. for different values of the berm length L_B).

The water depth at the toe of the berm (i.e. h_T), the offshore significant wave height and peak period, hence the wave length at the toe of the berm (i.e. L_W), have been kept constant.

The value of the ratio h_B/h_T ranged from 0.09 up to 0.906. The ratio L_B/L_W ranged from:

$$\left(\frac{L_B}{L_W}\right)_{min} = 0.282 - 0.267\frac{h_B}{h_T} \tag{2.32}$$

up to 0.356. It could be noted that the lower limit of the ratio is defined by Equation 2.32 due to the definition of berm length (L_B). Indeed, it is defined starting from the toe of the berm and it is not realistic to consider high and short berms.

In the case at hand, the slope of the offshore boundary of the berm has been kept constant as 1V:2H (see Figure 2.13). Table 2.3 synthesizes the comparison of the validity range of existing criteria (e.g. Van Der Meer, 1988; van Gent, 2013) and of the proposed criterion.

Validity ranges			
Parameter	VDM1988	VG2013	Proposed
h_B/h_T	1.0	-0.167÷0.125	0.09÷0.91
L_B/L_W	0.0	0.015÷0.110	(0.282-0.267h_B/h_T)÷0.356

Table 2.3: Comparison among the validity ranges of existing criteria in terms of berm parameters (VDM1988 refers to the criterion proposed by Van Der Meer, 1988 and VG2013 to the criterion proposed by van Gent, 2013) and the proposed criterion.

The total length of the computational domain is set at 884 m and the cell size in the x-direction at 0.5 m. The model is run with three layers in the vertical direction in order to properly describe the wave frequency dispersion. The offshore boundary is considered as weakly reflective and a water level time series, synthesized from Jonswap spectrum (γ = 3.3, H_s = 2.5 m, T_p =

7.5 s), is imposed. At the onshore boundary, the Sommerfeld radiation condition is applied and a sponge layer is placed behind the berm (see Figure 2.13) to absorb the propagating waves and to minimize the wave reflection (e.g. Zijlema et al., 2011). The total length of the sponge layer is 300 m, equal to about five times the typical wave length.

For each tested berm configuration, the computed water level time series have been extracted and standard reflection analyses performed. In this respect, it has to be noticed that, despite the presence of a sponge layer, a small amount of reflected components was still evident. This justifies the choice of carrying out reflection analysis. The computed incident wave spectra have been used to synthesize free surface time series from which the 2% exceedance individual wave heights over the berm $\left(H^B_{2\%}\right)$ have been evaluated. The same method is applied to evaluate the 2% exceedance individual wave heights at the toe of the berm $\left(H^T_{2\%}\right)$. Hence, the underlying behavior of function $f\left(\cdot\right)$ expressed by Equation 2.14 may be drawn.

Figure 2.14 (upper panels) shows the variation of the normalized 2% exceedance individual wave height over the berm $\left(H^B_{2\%}/H^T_{2\%}\right)$ as a function of the dimensionless water depth over the berm (h_B/h_T , upper left panel) and of the dimensionless berm length (L_B/L_W , upper right panel). It could be noted how the normalized $H^B_{2\%}$ decreases as the dimensionless water depth over the berm decreases and the dimensionless berm length increases. Moreover, it tends to the unity as the dimensionless water depth over the berm increases and the dimensionless berm length decreases.

For comparison, Figure 2.14 (lower panels) shows also the variation of the normalized significant wave height over the berm $\left(H^B_s/H^T_s\right)$ as a function of the dimensionless water depth over the berm (h_B/h_T, lower left panel) and of the dimensionless berm length (L_B/L_W, lower right panel).

It should be emphasized that the points clouds exhibit different shapes, at least from a qualitative point of view, as the empirical probability distribution functions of the individual wave heights change as the water depth over the berm decreases

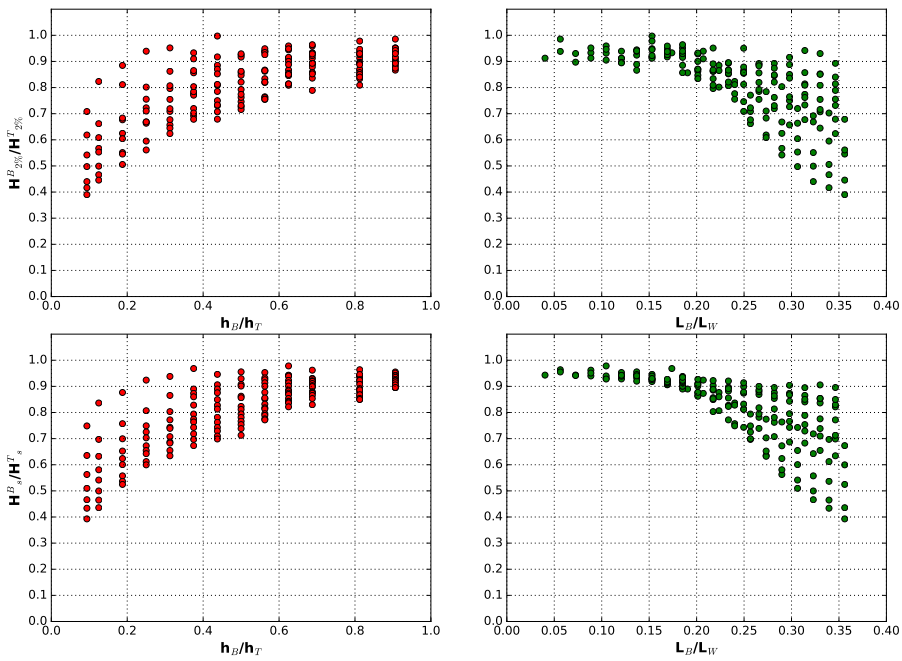

Figure 2.14: Variation of the normalized 2% exceedance individual wave height over the berm ($H^B_{2\%}/H^T_{2\%}$, upper panels) and of the normalized significant wave height over the berm (H^B_s/H^T_s, lower panels) as a function of the dimensionless water depth over the berm (h_B/h_T, left panels) and of the dimensionless berm length (L_B/L_W, right panels).

(left part of left panels) or the berm length increases (right part of right panels).

2.6 THE PROPOSED STABILITY FORMULA

On the basis of the numerical results illustrated in the previous Section, and with the aim to practically define the functional of Equation 2.14, it is possible to express γ as follows:

$$\gamma = 1 - a \left(\frac{L_B}{L_W}\right)^b \left(\frac{h_B}{h_T}\right)^c \tag{2.33}$$

It could be noted that, from a qualitative point of view, the empirical parameter b should be positive and c negative: the longer and the higher the berm, the strong its effects in reducing wave heights reaching the armor.

Then, Equation 2.33 is able to describe that the normalized 2% exceedance individual wave height over the berm (i.e. γ) tends to the unity if the berm is absent (i.e. $L_B/L_W \rightarrow 0$), by keeping in mind that the numerical results have been obtained within the validity range defined in Section 2.5.

The empirical parameters in Equation 2.33 i.e. a, b and c, have been estimated by means of a non-linear regression method (e.g. Gauss-Newton method) and their estimated values are reported in Table 2.4.

Figure 2.15 shows the scatter plot of the estimations by Equation 2.33 and the values of γ computed by means of the numerical model $\left(R^2 = 0.897\right)$.

parameter	**value**
a	$+0.968 \pm 0.227$
b	$+1.539 \pm 0.174$
c	-0.503 ± 0.041

Table 2.4: Empirical parameters to be used in Equation 2.33 along with their 0.95 confidence interval.

Figure 2.16 shows the comparison of the estimated damage parameter S_d against the observed values during the experimental investigation (see Section 2.4). It could be noted that the proposed method is able to properly represent the decrease of the armor damage (e.g. Van Der Meer, 2011), while the criterion proposed by Van Der Meer, (1988) is not, as it is not intended to describe the influence of berms upon the armor stability. On the other hand, the criterion proposed by van Gent, (2013) cannot be used because the tested configurations are well outside its validity range. Indeed, it tends to overestimate the role of the berm in increasing the stability of the armor. In other words, while the use of the criterion proposed by Van Der Meer, (1988) leads to a safe overestimation of the damage, the use of the criterion proposed by van Gent, (2013) outside its validity range, leads to an unsafe underestimation of the damage. It should be highlighted that other design criteria exist (e.g. Herrera et al., 2017). Nevertheless, the comparison shown by Figure 2.16, suffices

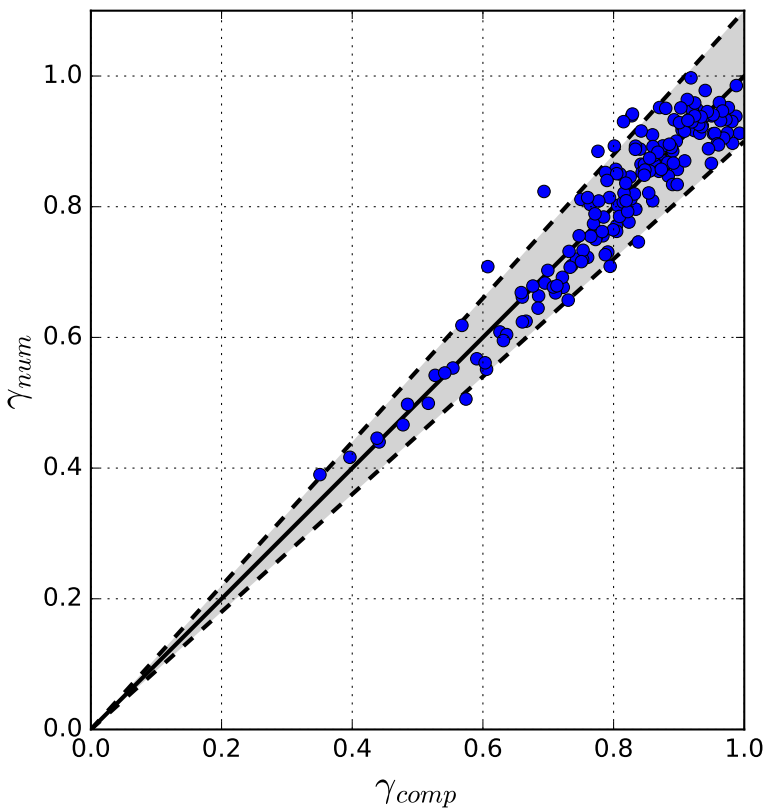

Figure 2.15: Scatter plot of the estimation (γ_{comp}) obtained by Equation 2.33 and the values of γ computed by means of the numerical model (γ_{num}). Shaded area refers to the $\pm$ 10 % deviation.

to underline the importance to use design criteria within their validity ranges when dealing with the influence of submerged berms on the armor layer stability.

The same big picture may be drawn by looking at Figure 2.17.

It is aimed to show the ratio of the stability number (N_{s-VDM}) estimated by using the criterion proposed by Van Der Meer, 1988 to the stability number (N_s) evaluated by either the criterion proposed by van Gent, 2013 or the criterion proposed herein. It is trivial to observe that the ratio (N_{s-VDM}/N_s) is equivalent to the ratio of the estimated mean diameters $(D_{n50}/D_{n50-VDM})$. Results inspection reveals that the usage of the criterion proposed by van Gent, (2013) leads to the unsafe overestimation of the armor stability if it is applied outside its validity range.

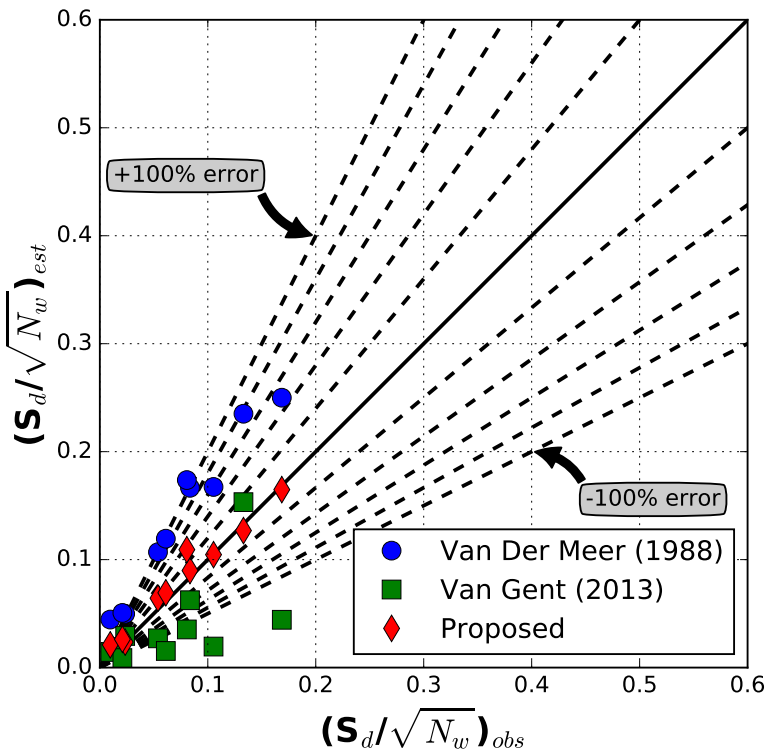

Figure 2.16: Scatter plot of the observed damage parameter $(S_d/\sqrt{N_W})_{obs}$ to the estimated damage parameter $(S_d/\sqrt{N_W})_{est}$ by means of the criteria proposed by Van Der Meer, 1988 (circles), by van Gent, 2013 (squares)and by means of the criterion proposed herein (diamonds). Solid line refers to the perfect fitting. Dashed lines refer to relative errors (expressed as a percentage) with a 20% step (only the ±100% relative error lines have been labeled).

2.6.1 *Example calculation*

In order to make clearer to the readers the usage of the proposed criterion, an example calculation follows.

The water depth at the toe of the structure is given as h_T = 8.0 m (see Figure 2.18). By means of a standard spectral wave propagation model it is possible to estimate the wave characteristics at the toe of the structure (see Table 2.5).

The slope of the armor layer is given as cot α = 2.5. The permeability factor of the structure is selected as P =0.4. A berm is foreseen at the toe of the breakwater whose length (L_B) and

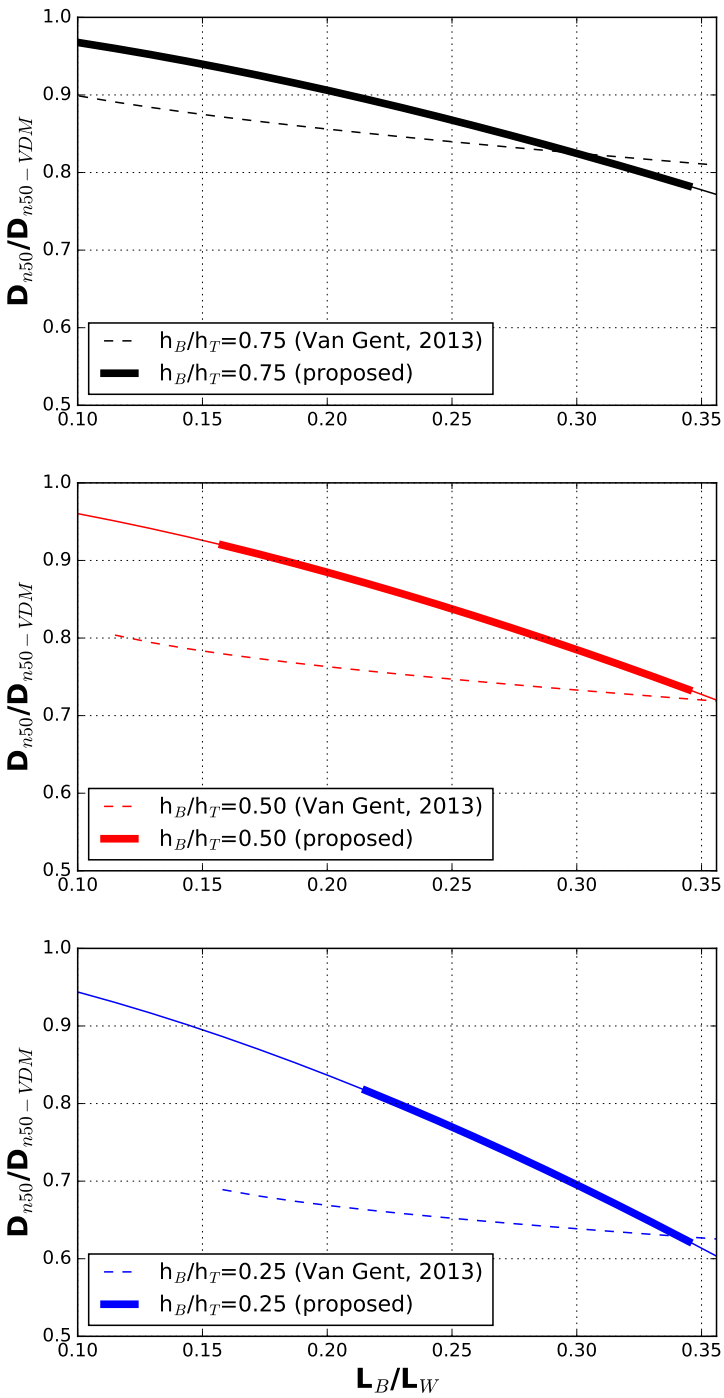

Figure 2.17: Comparison of the mean diameter of armor elements estimated by means of the criteria proposed by Van Der Meer (1988), ($D_{n50-VDM}$), by van Gent (2013), (D_{n50}, dashed lines) and proposed herein (D_{n50} , continuous lines). The curves refer to the ratio of D_{n50} to $D_{n50-VDM}$ (equal to the ratio of the related stability numbers, i.e. N_{s-VDM}/N_s). Thin lines are intended to indicate that the criterion is used outside the validity ranges, thick lines that the criterion is used inside the validity ranges. Main parameters: S_d = 2, h_T = 6 m, cot α = 2.5.

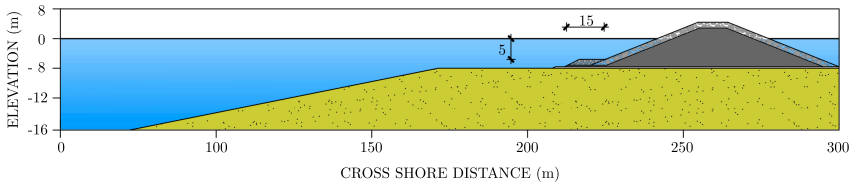

Figure 2.18: Sketch aimed at illustrating the geometry adopted for the example calculation.

thickness (= $h_B - h_T$) are given as 15.0 m and 5.0 m (i.e. h_B = 3) respectively.

parameter	value
H_{m0}	4 m
T_p	11.4 s
T_m	9.5 s
$T_{m-1,0}$	10.5 s

Table 2.5: Wave characteristics at the toe of the structure, evaluated by means of a standard spectral wave propagation model.

The slope of the offshore boundary of the berm is given as 1V:2H. The acceptable damage parameter is given as S_d = 2. The method proposed by Battjes and Groenendijk, (2000) may be used to estimate the values of the significant wave height (H_s) and 2% exceedance individual wave height $(H_{2\%})$. In particular, it provides the values of a series of ratios of characteristics wave heights (i.e. $H_{2\%}$, H_s, $H_{1/10}$, etc ...) to the root mean square wave height (H_{rms}) in tabular form, as a function of a dimensionless transitional wave height $\left(\tilde{H}_{tr} = H_{tr}/H_{rms}\right)$.

The transitional wave height (H_{tr}) is defined as follows:

$$H_{tr} = (0.35 + 5.8\ tan(\beta))\, h_T \tag{2.34}$$

where β is the foreshore bottom slope (given as 1V:100H). The root mean square wave height may be estimated, in shallow water, as follows:

$$H_{rms} = \left(0.6725 + 0.2025\frac{H_{m0}}{h_T}\right) H_{m0} \tag{2.35}$$

Equations 2.34 and 2.35 allow estimating the dimensionless transitional wave height, and to select from the table provided by Battjes and Groenendijk, 2000, the needed information. Nevertheless, the tabular values may be approximated by means of the following relationships:

$$\frac{H_s}{H_{rms}} = 1.3475 + 0.0685 \tanh\left(\frac{\tilde{H}_{tr} - 1.1}{0.3}\right) \tag{2.36a}$$

$$\frac{H_{2\%}}{H_s} = \begin{cases} 1.21 & \text{if } \tilde{H}_{tr} < 1.15 \\ 1.21 + 0.224\left(\tilde{H}_{tr} - 1.15\right)^2 & \text{if } 1.15 \leq \tilde{H}_{tr} < 2.0 \\ 1.40 & \text{if } \tilde{H}_{tr} \geq 2 \end{cases} \tag{2.36b}$$

The usage of Equations 2.36a and 2.36b lead to a maximum relative error, with respect to the tabular data of Battjes and Groenendijk, 2000, equal to 0.15% and 2.0% respectively.

With regard to the example proposed herein, a 2% exceedance individual wave height ($H_{2\%T}$) equal to 5.01 m and a significant wave height (H_s) equal to 4.14 m are estimated. The using of the design criterion proposed by Van Der Meer, (1988), (i.e. Equations 2.4) by considering 2000 individual waves, leads to N_s = 2.14, related to a mean diameter of armor elements equal to D_{n50} = 1.22 m (ρ_s = 2650 kg/m^3, ρ_w = 1025 kg/m^3) or a mean mass of armor elements equal to M_{50} = 4.82 t. It has to be stressed that this formulation does not take into account the presence of the submerged berm.

If the formulation proposed by van Gent, (2013) is used, the stability number is estimated as 2.74, then a mean diameter D_{n50} = 0.95 m (i.e. about 22% smaller than expected based on the criterion of Van Der Meer, (1988)) and a mean mass M_{50} = 2.29 t (i.e. about 52% lighter than expected based on the criterion of Van Der Meer, 1988) are achieved.

It should be emphasized that the considered configuration of the berm is outside the validity range of the criterion proposed by van Gent, (2013).

If the proposed criterion is used, a stability number equal to 2.35, then a mean diameter D_n50 = 1.11 m (i.e. about 9% smaller than expected based on the criterion of Van Der Meer, (1988)) and a mean mass M_50 = 3.63 t (i.e. about 25% lighter than expected based on the criterion of Van Der Meer, 1988) are achieved.

The usage of the criterion proposed by van Gent, (2013), outside its validity range, leads to an unsafe dimensioning of the armor elements.

Table 2.6 synthesizes the main results of the example calculations.

Known parameters			
cot(α) - P	3.0 - 0.4		
L_B - h_B - h_T	15.0 m - 3.0 m - 8.0 m		
S_d	2.0		
Characteristic wave heights			
H_{rms}	3.09 m		
H_s	4.14 m		
$H_{2\%}$	5.01 m		
Dimensioning results			
Parameter	VDM1988	VG2013	Proposed
Ns	2.14	2.74	2.35
Dn50 (m)	1.22	0.95	1.11
M50 (t)	4.82	2.29	3.63

Table 2.6: Main parameters and results of the example calculation (VDM1988 refers to the criterion proposed by Van Der Meer, (1988) and VG2013 to the criterior porposed by van Gent, (2013)).

3

THE ROLE OF SUBMERGED BERMS ON THE SOIL STABILITY AROUND RUBBLE MOUND BREAKWATERS

Before describing the topic on which the chapter is focused on, it is useful starting with a brief introduction to the physics of wave induced soil liquefaction. Then, after explaining the adopted rationale within the "Methodology" section, a description of the employed numerical models follows. The succeeding sections detail the parametric study that has been carried out by varying the berm configuration, keeping constant the offshore regular wave conditions, the water depth and the elastic properties of the soil. Results indicate that the presence of submerged berms tends to mitigate the liquefaction probability if compared to straight sloped conventional breakwater without a berm. In addition, it appears that the momentary liquefaction phenomena are more influenced by changing the berm length rather than the berm height.

3.1 WAVE-INDUCED LIQUEFACTION

Other than the hydraulic stability (detailed in Chapter 2), in designing rubble mound breakwaters, the soil stability around such structures must be ensured. Indeed, the stability of rubble mound breakwaters can be threatened also by geotechnical causes, as the soil liquefaction (e.g. Jeng, 2012; Sumer, 2014; Tsai, 1995).

In general, soils can be intended as multi-phase media, consisting of solid particles (i.e. soil skeleton) and pores or voids, that may be filled with water, air or both. The intergranular contacts among the particles provide the shear force transfer within the soil skeleton, only if they transfer normal forces at

the same time (e.g. De Groot et al., 2006). Normal forces can be transferred through the soil skeleton, as well as through the pore water, in case of saturated soil. Indeed, as expressed by Terzaghi's effective stress principle, the normal components of stresses (σ) can be decomposed into water pore pressure (p_p) and effective stresses ($\sigma^{'}$), where the last ones are supported by the soil skeleton:

$$\sigma = \sigma^{'} + p_p \tag{3.1}$$

Liquefaction occurs when the normal effective stress becomes zero. It could happen when the total stress remains constant and the pore pressure increases such that $\sigma^{'} = 0$, but also if the pore pressure remains constant and the total stress decreases such that $\sigma^{'} = 0$. In both cases, the shear stress that can be transferred becomes zero and the solid soil acts as a fluid.

When water waves propagate over a non-cohesive seabed and interact with coastal structures, two different types of liquefaction can be generated, the residual and the momentary liquefaction (Nago et al., 1993; Sumer, 2014).

The "residual" liquefaction is caused by compression-relaxation cycles under wave crests and wave troughs, respectively. They generate shear stresses that are able to rearrange the soil particles. This may result in the buildup of pore water pressure that could exceed the value of the overburden pressure, making the soil grains totally unbound.

The "momentary" liquefaction occurs during the passage of wave troughs (e.g. Sumer, 2014), where the pore pressure has negative sign (see Figure 3.1). For saturated soil (i.e. only water in the pores), the pressure gradient is not so large (see Figure 3.2a).

On the contrary, for an unsaturated soil (i.e. containing also gas in the pores), the resulting rapid decrease of pore pressure across the soil depth, produces high-pressure gradient, as depicted in Figure 3.2b. If the upward pore pressure gradient exceedes the submerged weight of the soil, the effective stresses vanish and the soil will be liquefied.

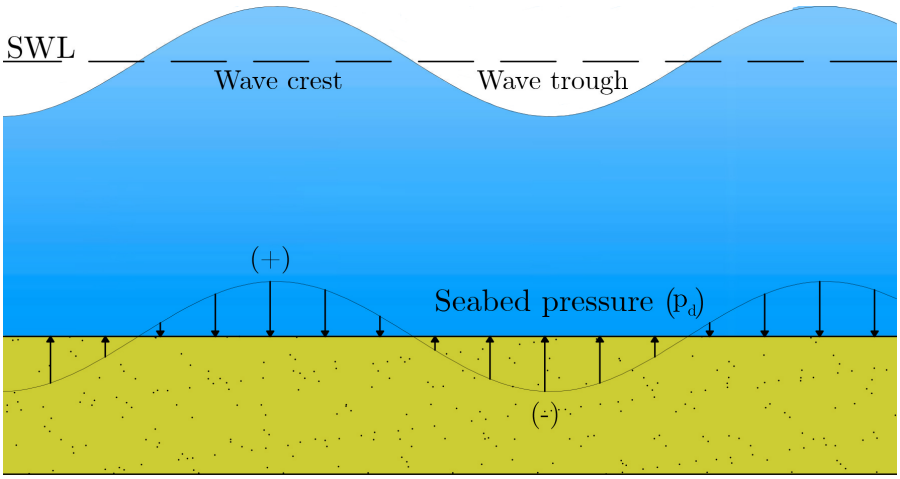

Figure 3.1: Seabed pressure under progressive wave.

The proposed work deals with rubble mound breakwaters. The knowledge of potential structure failure due to liquefaction should include the effects of both residual and transient pore pressure generation. However, this work is focused on the evaluation of submerged berm configuration only upon momentary liquefaction occurrences.

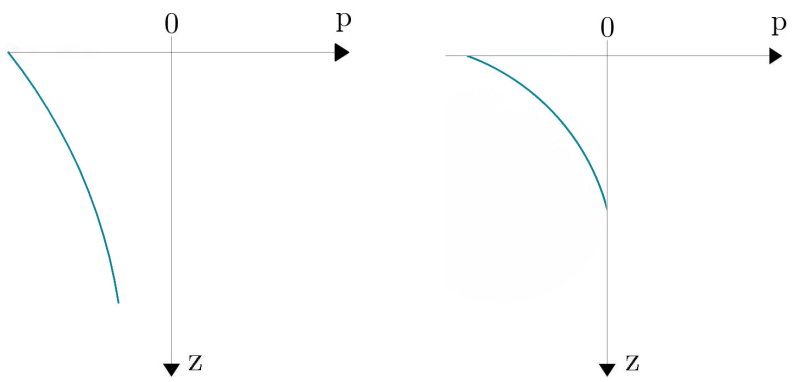

(a) Saturated soil (b) Unsaturated soil

Figure 3.2: Sketch of vertical pore pressure distribution in different type of soil.

3.2 METHODOLOGY

The aim of this work is to investigate the wave-induced soil response and momentary liquefaction probability around and beneath rubble mound breakwaters with (and without) sub-

merged berm. For this reason, a parametric-comparative study has been carried out by varying the berm configuration in terms of its length and its height, keeping constant the elastic properties of the soil, the water depth and the offshore regular wave conditions. The evaluation of the wave-induced soil response requires the knowledge of the spatio-temporal variation of the seabed pressure.

Due to its efficiency, the water wave hydrodynamic properties (including the pressure field) have been evaluated by means of SWASH (see Section 2.5), an open-source phase resolving numerical model for simulating non-hydrostatic, free-surface, rotational flows (Zijlema et al., 2011). Since this research study has involved 62 numerical simulations, only the usage of this type of tool enables to carry out the parametric study in a reasonable time.

The soil has been considered as an anisotropic poro-elastic medium, obeying to the classic Biot's consolidation equations (Biot, 1941). The dynamic interaction between the solid skeleton and the pore fluid, which develops under the seabed pressure action, has been modeled through an open-source poro-elastic soil solver. The soil model was developed within the Finite Volume Method (hereinafter referred to as FVM)-based OpenFOAM framework by Li et al., (2018) and was already employed for the detection of momentary liquefaction occurrences within the WSSI framework. It takes into account of anisotropy since most of the natural soils show some degree of anisotropy, i.e., having different elastic and hydraulic properties in different directions, according to Hsu and Jeng, (1994).

The interaction between the multiple physical phases (i.e. the soil mixture, the water and the porous structure) has been implemented by using the seabed dynamic pressure as one-way coupling boundary condition for the poro-elastic anisotropic soil model, applied on the common boundary. Hence, two physical domains are selected: the first one is addressed to the interaction between waves and porous structures, whilst the second one is dedicated to the seabed response to the waves loads. The common boundary is at the seabed surface. The minor motion

of the seabed soil does not alter the wave-porous structure domain, as depicted in Figure 3.3.

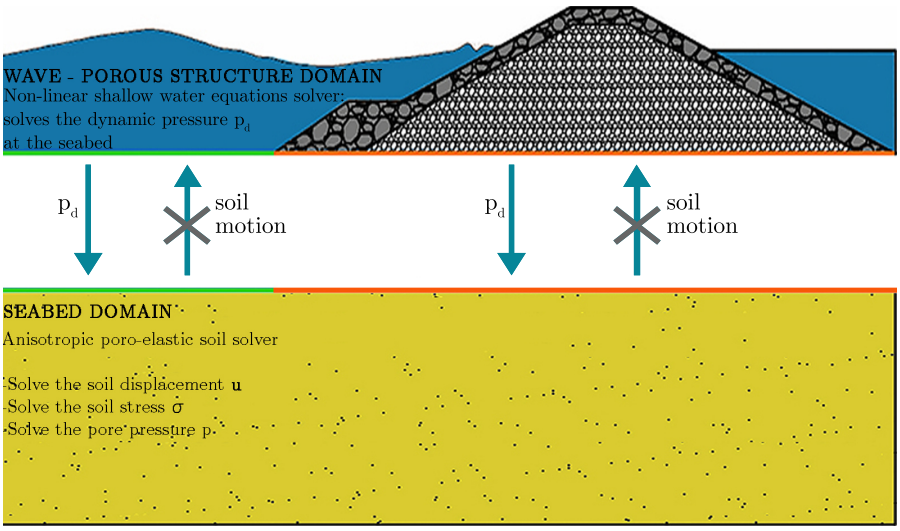

Figure 3.3: One-way boundary coupling algorithm of wave-structure-seabed interaction.

The dynamic wave pressure p_d, computed at the seabed layer and beneath the porous structure, transfers to the soil domain as a dynamic boundary condition. In the model, time-varying boundary conditions are implemented at the interface, by interpolating the values from the supplied domain in space and time. Since the grid sizes and time steps for the two domains are allowed to be different, it increases the efficiency of solving the coupled system and allows the usage of different numerical tools.

3.3 THE MATEMATHICAL MODEL

The numerical model SWASH has been used to compute the water wave hydrodynamic properties within the wave-structure interaction framework. As for the numerical simulations carried out within the hydraulic stability framework (see Chapter 2), in the research described herein, the numerical model has been employed by using three terrain-following layers in the vertical direction in the one-dimensional case. Indeed, the layer integrated continuity equation as well as the horizontal and vertical

layer-integrated momentum equations are the same described in Section 2.5.

3.3.1 *The soil numerical model*

Within the soil model framework, the following assumptions have been made (Li et al., 2018):

- the seabed has constant thickness;
- the soil skeleton obeys to Hooke's law (i.e. characterized by elastic properties);
- the Young's modulus, the Poisson's ratio and the constant soil permeability are different in vertical and horizontal directions (i.e. anisotropic condition).

The interaction among the solid skeleton and the pore fluid is described by the classic Biot's consolidation equations (Biot, 1941). Hence, the soil domain is governed by the quasi-static momentum balance equation for soil mixture and the mass balance equation of the pore fluid, based on Darcy's law.

Quasi-static momentum balance equation is presented in Equation 3.2:

$$\nabla \cdot \left[\mathbf{C} : \frac{1}{2} \left(\nabla \mathbf{U} + (\nabla \mathbf{U})^T \right) \right] - \nabla p = 0 \tag{3.2}$$

where $\mathbf{U}$ is the soil (skeleton) displacement, p is the pore fluid pressure and $\mathbf{C}$ is the elastic stiffness tensor. For anisotropic soil materials, the two dimensional (hereinafter referred to as 2D) orthotropic elastic stress-strain relation can be expressed in a 3 x 3 matrix notation:

$$\sigma' = \begin{pmatrix} \sigma'_{xx} \\ \sigma'_{zz} \\ \sigma_{xz} \end{pmatrix} = \begin{bmatrix} A_{11} & A_{12} & 0 \\ A_{12} & A_{22} & 0 \\ 0 & 0 & A_{33} \end{bmatrix} \begin{pmatrix} \epsilon_{xx} \\ \epsilon_{zz} \\ \epsilon_{xz} \end{pmatrix} = \mathbf{C} : \epsilon \tag{3.3}$$

where σ' is the effective stress tensor. The 4 independent coefficients A_{ij} are calculated from Young's modulus E_i, Poisson's ratio ν_{ij} and the shear modulus G_{ij} as follows:

$$\begin{aligned} A_{11} &= \frac{E_x}{1-\nu_{xz}\nu_{zx}} \\ A_{22} &= \frac{E_z}{1-\nu_{zx}\nu_{xz}} \\ A_{12} &= \frac{\nu_{xz}E_z}{1-\nu_{zx}\nu_{xz}} \\ A_{33} &= G_{xz} \end{aligned} \tag{3.4}$$

The mass balance equation of the pore fluid reads as follows:

$$\frac{n}{K'}\frac{\partial p}{\partial t} = -\frac{1}{\gamma_w}\nabla\cdot(\mathbf{k}\cdot\nabla p) + \frac{\partial}{\partial t}(\nabla\cdot\mathbf{U}) \tag{3.5}$$

where n denotes the soil porosity, γ_w represents the specific weight of the water in the soil and $\mathbf{k}$ denotes the diagonal permeability tensor with values k_x and k_z. The bulk modulus of the compressible pore flow K' is approximated through the formulation proposed by Vafai and Tien, (1981):

$$\frac{1}{K'} = \frac{1}{K_w} + \frac{1-S_r}{p_a} \tag{3.6}$$

where S_r represents the degree of soil saturation, K_w denotes the bulk modulus of pure water ($\approx$ 2 GPa), and p_a is the absolute pore water pressure.

3.4 MODEL CALIBRATION AND VALIDATION

The numerical model SWASH has been used to compute the wave-induced seabed pressure within the wave-porous structure interaction framework. At first, a series of preliminary tests have been carried out to evaluate the sensitivity of the seabed dynamic pressure for different computational grid sizes. A rubble

mound breakwater interacting with regular waves (H = 2 m, T = 7 s) has been simulated considering a domain length equal to 411 m and a series of computational grid spatial resolutions, ranging from 0.1 m up to 0.5 m. The seabed dynamic pressure time series have been collected at the same location for comparison purposes. Then zero-crossing analysis has been carried out and the mean values of the wave pressure heights have been evaluated. For a selected location (similar results are achieved for other points), Figure 3.4 shows the normalized values of the wave pressure heights i.e. $P_{dxi}/P_{dx0.1}$, taking as a reference the results obtained for the finest grid resolution (i.e. $P_{dx0.1}$).

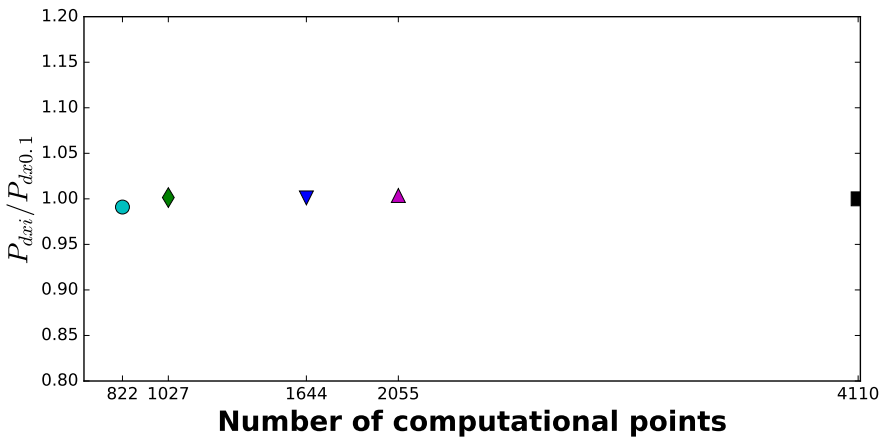

Figure 3.4: Variation of the normalized wave pressure height $P_{dxi}/P_{dx0.1}$, as a function of the number of computational points of the mesh.

With respect to the finest grid (i.e. dx=0.1 m), it appears that the difference of the results computed by adopting dx = 0.2 m is equal to 0.37%. Therefore, adopting a computational grid spatial resolution equal to 0.2 m suffices to achieve reliable numerical accuracy.

The model capability to simulate the effects of submerged berms on the incident waves transformation has been shown in Chapter 2 through a comparison with experimental data (e.g. see Figure 2.9). The reliability of the results given by SWASH, in terms of dynamic seabed pressure, has been evaluated through a comparison with the ones obtained by using a numerical

two-phase flow solver, developed within the OpenFOAM computational library by Higuera et al., (2014).

Such solver is widely used for coastal hydrodynamic studies and it is validated in terms of dynamic pressure calculation within the wave-porous structure (e.g. see Figure 6 of Higuera et al., 2014) and wave-structure (e.g. see Figure 7 of Castellino et al., (2018)) interaction frameworks. It solves the VARANS equations at the expense of high computational costs if compared to those required by SWASH numerical model. The computational domain illustrated in Figure 3.5 has been used in both the numerical models for comparison purposes.

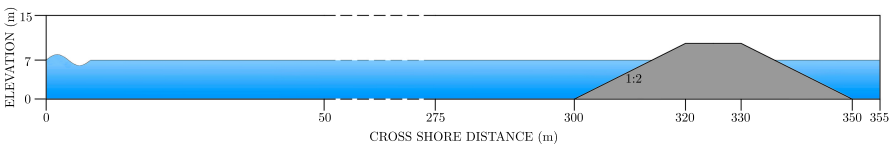

Figure 3.5: Sketch of the computational domain implemented to numerically catch the wave-induced seabed pressure by using SWASH and OpenFOAM solver.

In the SWASH model, the two-dimensional vertical domain (hereinafter referred to as 2DV) has been discretized by a constant horizontal spacing dx = 0.2 m, as suggested by the convergency study (see Figure 3.4). In order to properly describe wave dispersion also in the offshore zone, where shallow water conditions do not apply, a fixed number of three terrain-following layers in the vertical direction has been selected, each of them characterized by equal thickness between the bottom and the moving free surface. A porosity layer has been placed inside the computational domain to simulate the presence of the rubble mound breakwater in terms of its reflection effects. A volumetric porosity value of 0.4 has been used for both the berm and the armor layer. Moreover, appropriate boundary conditions have been imposed at the boundaries of the computational grid to solve the governing equations. A still water level is applied as initial condition. A water level time series condition has been imposed at the offshore side of the computational domain (reproducing regular waves characterized by H = 4 m and T = 8 s)

as a weakly reflective boundary. This provides that target waves are generated at this boundary, while reflected waves from onshore are radiated. The Sommerfeld radiation condition has been applied to the onshore side of the numerical domain. As suggested by Suzuki et al., (2017), the non-hydrostatic pressure term is applied with a Keller-box scheme, which has significant influence on wave transformation. Adaptive time step has been employed by respecting the Courant-Friedrichs-Lewy (CFL) condition.

In the OpenFOAM model, the 2DV domain has been discretized by adopting an orthogonal mesh characterized by a cell resolution equal to 0.20 m along the x-direction and 0.05 m along z-direction (5.32 x 10^5 elements). The porous structure has been modeled by using a porosity value n = 0.4. A still water level is applied as initial condition. A regular wave generation (H = 4 m, T = 8 s) and absorption boundary conditions presented in Higuera et al., (2013), have been adopted for the offshore and onshore sides of the computational domain. The integration time step is automatically chosen to ensure numerical stability. The Courant number was set to a maximum value of 0.45.

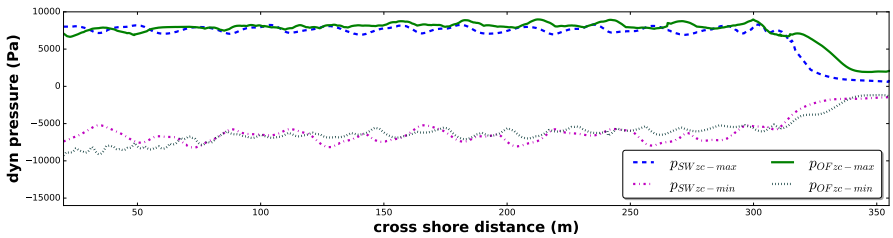

Figure 3.6: Spatial distribution of the maximum and minimum individual wave-dynamic pressure crests and troughs values, computed by using SWASH (blue dashed and magenta dot dashed lines) and OpenFOAM solver (green continuous and cyan dotted lines).

Figure 3.6 shows the comparison of computed maximum ($P_{SW_{zcmax}}$, obtained by means of SWASH and $P_{OF_{zcmax}}$, obtained by means of the OpenFOAM solver) and minimum ($P_{SW_{zcmin}}$, obtained by means of SWASH and $P_{OF_{zcmin}}$, obtained by means of the OpenFOAM solver) individual wave-dynamic pressure crests and troughs values, respectively. The results are depicted

starting 20 m far from the offshore side of the computational domain, in order to avoid result discrepancies related to the different implemented offshore boundary conditions. The inspection of Figure 3.6 reveals a general agreement between the results. Nevertheless, it should be stressed that under the breakwater, the values of the seabed maximum dynamic pressure computed by SWASH are lower than those obtained by using the OpenFOAM solver. However, the values of seabed minimum dynamic pressure, which is able to induce the momentary liquefaction, are comparable. The presence of observable results discrepancies among the two numerical models becomes of negligible importance when a parametric-comparative study is carried out. Therefore, the SWASH model could be reasonably used for the aforementioned work purposes, as its computational cost is compatible with the proposed extensive parametric-comparative study this Thesis deals with.

The seabed response to the wave-induced seabed pressures has been evaluated by using an ad-hoc anisotropic poro-elastic soil solver (Li et al., 2018), developed within the OpenFOAM framework. A grid convergence study has been carried out for the soil model, simulating a 30 m thick and 450 m long portion of soil (see Figure 3.7), subject to wave-induced seabed pressure acting on the upper boundary, adopting three different sets of meshes (see Table 3.1).

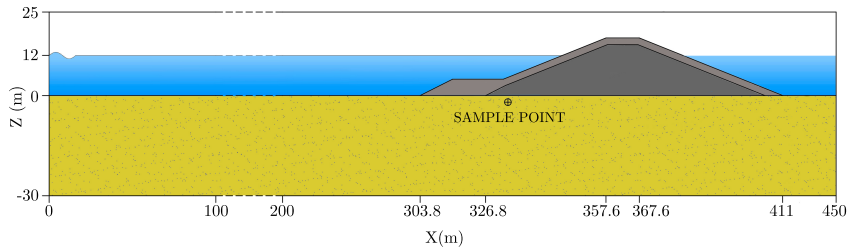

Figure 3.7: Sketch of the computational domain implemented for the soil model convergency study. It is shown the sample point (x = 330.2 m, z =-2 m), where the pore pressures are collected.

The dynamic pore pressures, collected in the sample point (see Figure 3.7), have been compared as shown in Figure 3.8.

Mesh	Number of grid points	Minimum pressure (Pa)	Relative change
No.1	8.43 x 10^4	-5116.88	1.28%
No.2	2.70 x 10^5	-5183.30	0.45%
No.3	6.75 x 10^5	-5206.84	

Table 3.1: Mesh parameters for the soil model convergency study (relative change is evaluated with respect to the finest Mesh No.3).

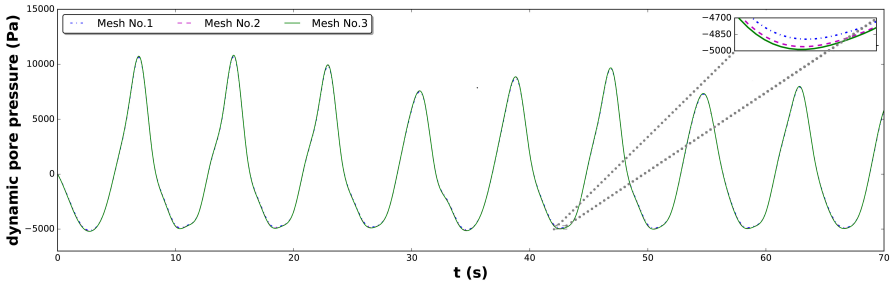

Figure 3.8: Grid convergence for dynamic pore pressure in the seabed (sample point coordinates: x = 330.2 m , z = -2 m).

It appears that as the number of grid points increases, the pore pressure converges to a higher amplitude (in absolute value). This implies that an insufficient number of points may underestimate the pore pressure in the seabed. As illustrated in Table 3.1, the relative change of minimum pressure derived from the finest tested mesh (Mesh No.3) and the medium tested mesh (Mesh No.2) is 0.45%. Then, 2.7 x 10^5 grid points (i.e. Mesh No.2) have been used to perform the parametric study described herein.

The capability of the solver to catch the wave-induced seabed response has been validated by Li et al., 2018, through a comparison with experimental data provided by Tsai and Lee, (1995) (e.g. see their Figures 2, 3 and 4).

3.5 NUMERICAL INVESTIGATIONS

The wave-induced liquefaction in a sandy seabed could cause the collapse of the breakwater toe and the slip down of the armor units (e.g. Mase et al., 1994), but also more serious core damage, in the event that a transition layer is not foreseen at the interface between the seabed and the armor layer. Therefore, the aim of the second part of the Thesis is to evaluate the performances of submerged berms in reducing the momentary liquefaction depths around and beneath a rubble mound breakwater. The results have been compared to them associated with the presence of a straight sloped conventional breakwater without a berm. In both cases, the absence of a transition layer beneath the armour layer and the berm is assumed by considering the stones in direct contact with the seabed, loading the soil in a discontinuous way. It should be emphasized that various experimental works (e.g. Kudella et al., 2006) indicated the absence of momentary liquefaction occurrences underneath the breakwater, where the overburdened pressure is significantly enhanced by the self-gravity of the structure. In the work presented herein, all the momentary liquefaction occurrences appearing under the breakwaters are clearly due to the discontinuous load acting on the soil, as well as the absence of a transition layer under the berm. The former assumptions find justification if a safe rationale is employed.

Then, a parametric study has been carried out by varying the berm configuration (i.e. its length, L_B, and the water depth over the berm, h_B, see Figure 3.9), keeping constant the offshore regular wave conditions, the water depth and the elastic properties of the soil (see Table 3.2).

The value of the ratio h_B/h_T (being h_T the water depth at the toe of the berm) ranges from 0.2 up to 0.8, whilst the ratio L_B/L_W (being L_W the wave length at the toe of the berm) ranges from 0.040 up to 0.356 for a total of 62 simulations.

With the aim to evaluate the wave-induced seabed pressure for different submerged berm configurations (i.e. by varying the berm length L_B and the water depth over the berm h_B), the

Wave parameters			
Wave height H (m)	4.0		
Wave period $T(s)$	8.0		
Water depth h_t (m)	12.0		
Wave length L_w (m)	75.8		
Seabed parameters (directional values)			
Young's modulus (N/m^2)	E_x = 1.2 x 10^7	E_y = 1.2 x 10^7	E_z = 2.0 x 10^7
Poisson's ratios	ν_{xy} = 0.20	ν_{yz} = 0.24	ν_{zx} = 0.40
Shear modulus (N/m^2)	G_{xy} = 5 x 10^6	G_{yz} = 5 x 10^6	G_{zx} = 5 x 10^6
Permeability (m/s)	k_x = 0.005	k_y = 0.005	k_z = 0.001

Table 3.2: Parameter settings for wave-structure-seabed interaction.

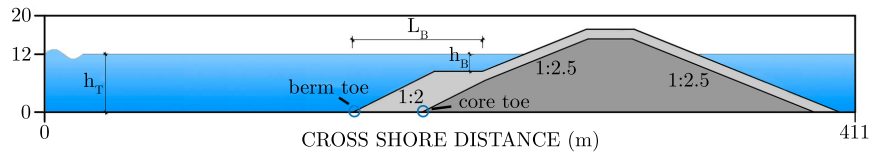

Figure 3.9: Geometric parameters definition of conventional rubble mound breakwater with a berm. The berm and core toe positions could vary among the simulated test cases.

simulations have been carried out by using SWASH numerical model, validated as described in Chapter 2.

Figure 3.9 shows one of the used computational domain. As for the simulations carried out for the validation of the model, the total length of the computational domain is set at 411 m and the cell size in the x-direction at 0.2 m. The model is run with three layers in the vertical direction, in order to properly describe the wave frequency dispersion. The offshore boundary is considered as weakly reflective and a water level time series, reproducing regular waves (see Table 3.2), is imposed. For each test case almost 90 individual waves have been simulated. At the onshore boundary, the Sommerfeld radiation condition is applied.

For each tested berm configuration, the computed seabed dynamic pressure time series have been collected and used as coupling boundary condition for the anisotropic Biot's porous soil model. The numerical domain of the porous seabed is 450

m long and 30 m thick. In order to avoid unwanted lateral boundary effects, a preliminary sensitivity study to evaluate the best structure location, inside the computational domain, has been carried out. Therefore, it has been decided to place the porous structure at a distance equal to almost 4 λ from the left side of the computational domain (where λ is the wave length at the toe of the berm, equal to 75.83 m).

Moreover, the soil domain was extended of a quantity equal to 39 m starting from the breakwater end, in order to further limit the effect of the onshore boundary.

The properties of the seabed sand sediment are based on the measurements of the North sea soil by Kjekstad and Lunne, (1981), with reasonable assumptions concerning the anisotropic properties. Since the comparative nature of the present work, based on the evaluation of the submerged berms configuration effects on the momentary liquefaction occurrences, the importance of simulating several soil properties is not crucial. The soil porosity n is set 0.3 and the saturation factor S_r is set to 0.975.

The anisotropic parameter settings are shown in Table 3.2. The boundary conditions of the seabed domain are specified as follows.

1) At the wave-seabed and the porous structure-seabed interfaces (see Figure 3.3), the effective soil stresses vanish, hence the soil has zero traction at the seabed surface. The pore pressure, at the aforementioned interfaces, is equal to the dynamic wave pressure acting on the seabed and beneath the porous structure.

2) At the bottom and lateral boundaries of the seabed, the soil skeleton is allowed to slip and the normal pore pressure gradient is zero.

3.6 RESULTS AND DISCUSSION

3.6.1 *Consolidation*

The deployment of the breakwaters can significantly increase the effective stresses in the surrounding soil. Once the structure is built on the seabed, the self-weight of a breakwater is initially transferred to the pore water in the seabed foundation, resulting in the generation of excess pore pressure. Then, the soil will experience the gradual dissipation of the excess pore pressure. Consequently, the breakwater load is gradually transferred from the pore water to the soil skeleton. At the end of the process, the seabed foundation reaches an equilibrium consolidation status. Therefore, the determination of the initial consolidation status of seabed foundation under hydrostatic pressure and breakwater weight is an essential step in the evaluation of structures stability (Jeng and Ye, 2012), since it is able to influence the potential probability of dynamic wave-induced soil liquefaction (e.g. Sui et al., 2017; Ulker et al., 2010; Zhao et al., 2017).

Figure 3.10 shows the vertical soil displacement U_z after the completion of the consolidation process for the simulated test cases with $h_B/h_T = 0.49$ and $L_B/L_W = 0.25$. A negative value of U_z indicates that the soil skeleton is compressed and moves downward.

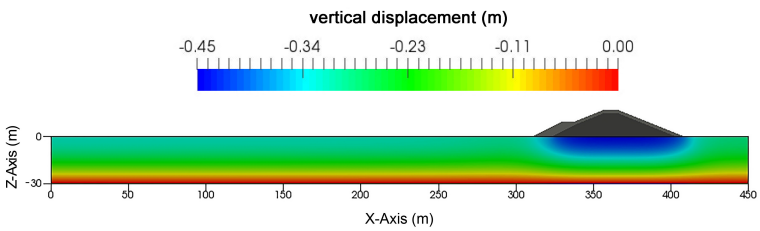

Figure 3.10: Vertical soil displacement U_z after the completion of the consolidation process for a breakwater with submerged berm characterized by $h_B/h_T = 0.49$ and $L_B/L_W = 0.25$.

It appears that beneath the structure, the soil skeleton has been largely compressed compared to the far field. The vertical soil displacement under the berm is lower (in absolute value)

than that under the breakwater core due to the berm reduced weight.

Figure 3.11 shows the distribution of the vertical effective stresses $\sigma_z^{'}$ in the soil, at the end of the consolidation process. A negative value of $\sigma_z^{'}$ indicates the compression of the soil skeleton.

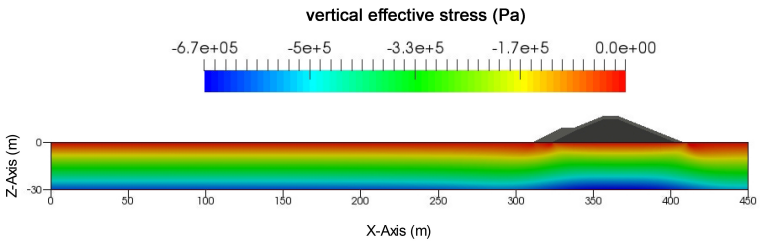

Figure 3.11: Vertical effective stress $\sigma_z^{'}$ after the completion of the consolidation process for a breakwater with submerged berm characterized by h_B/h_T = 0.49 and L_B/L_W = 0.25.

It appears that the gravity of the structure is gradually transferred to the supporting soil skeleton. The portion of soil beneath the breakwater is characterized by higher (absolute) values of vertical effective stresses if compared to the far field. Figure 3.11 also shows a compressive stress concentration at the berm-core interface as well as at the end of the breakwater. This effect is justified by the different gravitational load distributions between the submerged berm and the core, as well as between the loaded and unloaded areas at the end of the breakwater.

The vertical effective stresses $\sigma_z^{'}$ computed at the end of the consolidation process have been used as an initial condition for the momentary liquefaction analysis. It should be stressed that during the construction phase, when the consolidation state has not been reached, the vulnerability of the structure to liquefaction occurrences could be higher.

3.6.2 *Wave-induced seabed response*

Figure 3.12 shows the wave-induced transient pore pressure and the seepage flow in the seabed at the time instant t = 676 s, for one of the simulated test cases (i.e. h_B/h_T = 0.59 and L_B/L_W =

0.3). As expected, the passage of wave crests induces positive transient pore pressures, whilst the transient pore pressures become negative under the wave troughs. The same big picture could be drawn focusing on the seepage flow, and its direction is directly related to the wave phases (e.g. Jeng et al., 2013).

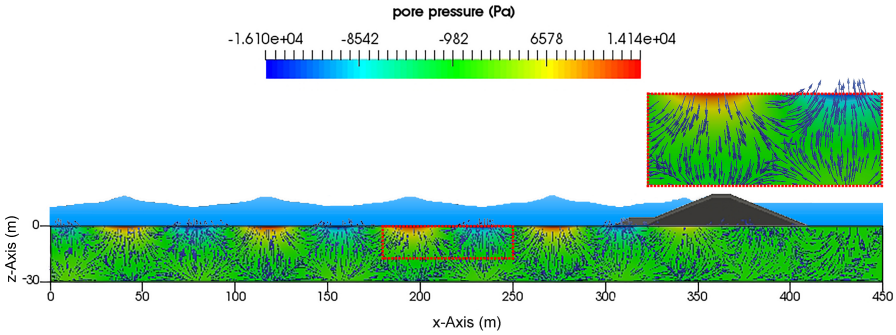

Figure 3.12: Transient pore pressure and seepage flow at the instant t = 676 s (H = 4 m) for a breakwater with submerged berm characterized by h_B/h_T = 0.59 and L_B/L_W = 0.30.

The seepage flow is directed downward during the passage of wave crests, leading to the compression of the soil. On the other hand, the seepage flow is directed upward during the passage of wave troughs, leading to the decompression of the soil. It should be underlined that the momentary liquefaction is directly related to the magnitude and direction of seepage forces. In particular, when the upward pore pressure gradient (strictly related to the seepage forces) exceeds the vertical initial effective stress, the momentary soil liquefaction is likely to occur and further affects the structure stability. The seabed does not liquefy when the seepage force is downward because it increases the contact effective stresses of soil particles (e.g. Jeng et al., 2013). A deeper discussion about the liquefaction analysis is presented in the next section.

Figure 3.13 shows the wave-induced shear stresses σ_{xz} in the seabed. By neglecting the seabed response close to the left boundary of the computational soil domain, affected by the lateral boundary proximity, it could be observed that under the periodic wave loading, the shear stresses σ_{xz} values switch from positive to negative periodically. In the present work, the shear

failure is not investigated. Nevertheless, it should be stressed that the wave-induced cyclic dynamic shear stresses could be a crucial factor for the stability of breakwaters (Ye et al., 2016). They can lead to the progressive buildup pore pressure that may eventually be large enough to result in significant deformation of the soil (Nataraja and Gill, 1983).

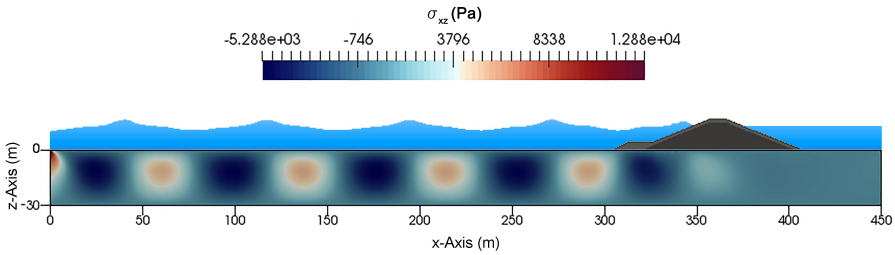

Figure 3.13: Shear stress σ_{xz} distribution in the seabed at the instant t = 676 s (H = 4 m) for a breakwater with submerged berm characterized by h_B/h_T = 0.59 and L_B/L_W = 0.30.

3.6.3 *Momentary liquefaction analysis*

The liquefaction criterion adopted in the present work is a modified version from Zen and Yamazaki, (1990). The latter authors proposed a 1D liquefaction criterion based on the excess pore pressure:

$$p(z,t) - p(0,t) \geq (\gamma_s - \gamma_w)z \tag{3.7}$$

afterward extended by Jeng, (1997) to the 3D cases:

$$p(z,t) - p(0,t) \geq -\frac{1+2K_0}{3}(\gamma_s - \gamma_w) \tag{3.8}$$

where $p(z,t)$ is the pore pressure in the seabed, $p(0,t)$ is the pore pressure at the seabed surface, γ_s and γ_w are the unit weight of soil and water respectively, K_0 is the coefficient of lateral earth pressure.

It should be stressed that Equation 3.8 is only applicable in absence of any structure. As for this work, if rubble mound

breakwaters are concerned, the adopted momentary liquefaction criterion reads as follows:

$$p(z,t) - p(0,t) \geq \sigma'_{z0} \tag{3.9}$$

where σ'_{z0} represents the initial vertical effective stress induced by the gravitational forces from the consolidation process. The present criterion was used in the works of Sui et al., (2017), Zhao et al., (2017) and Li et al., (2018). In order to investigate the effects of submerged berm deployment, the adopted rationale imposes a comparison among the aforementioned series of results deriving from the deployment of a rubble mound breakwater without a berm. Figure 3.14 shows the liquefaction depth achieved in the presence of the rubble mound breakwater without the submerged berm. It should be emphasized that, for comparison purposes, this simulation has been carried out considering the armor layer elements in direct contact with the seabed, loading the soil in a discontinuous way, as well as taking into account a transition layer deployment only beneath the core.

The upper panel of Figure 3.14 shows the maximum values of liquefaction depth around and beneath the structure, whereas in the lower panel, the maximum liquefied area has been divided into two subareas: the internal subarea (i.e. light green zone) shows what happens beneath the structure, whilst the external one (i.e. dark green zone) shows what happens in front of the structure, up to the breakwater toe.

In the lower panel of Figure 3.14, the origin of the coordinate system is located at the core toe. For each of the detected subareas, the maximum and the mean local depth (i.e. obtained dividing the subarea value by its superficial length) have been evaluated. From the inspection of Figure 3.14, it appears that the maximum internal liquefaction depth (hereinafter referred to as $d_{max_{int}}$), equal to 1.75 m, is greater than the external one (hereinafter referred to as $d_{max_{ext}}$) equal to 1.49 m. Also the comparison among the mean maximum values (hereinafter referred to as $\bar{d}_{ext}$ and $\bar{d}_{int}$) confirms that in a rubble mound breakwater

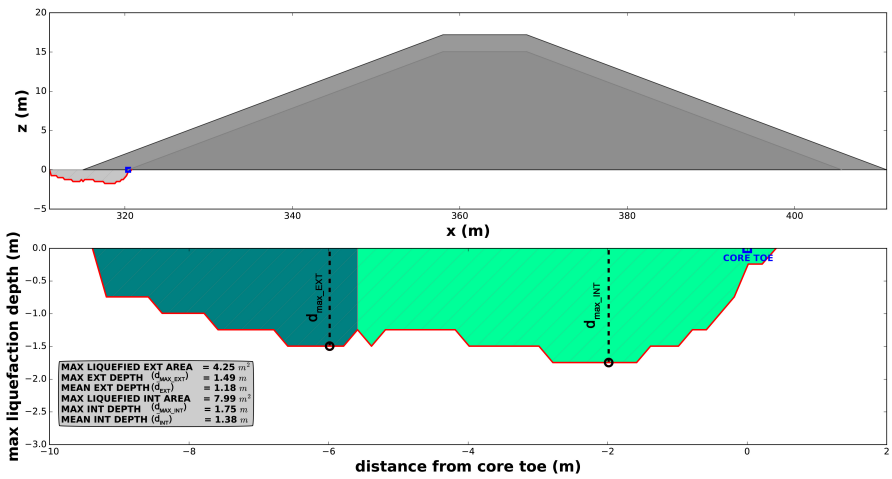

Figure 3.14: Wave-induced momentary liquefaction with reference to a breakwater without submerged berm. Upper panel: momentary liquefaction maximum depth around and beneath the structure. Lower panel: zoom of the momentary liquefaction maximum area splits into two subareas, according to the location of the liquefaction occurrences. Dark green subarea refers to maximum liquefaction depth in front of the structure up to the breakwater toe. Light green subarea refers to maximum liquefaction depth beneath the structure.

without submerged berm, the most exposed part to the momentary liquefaction occurrences is the area beneath the armor layer. Hence, the probability of the structure failure triggering is high in that location.

For comparison purposes, Figures 3.15 and 3.16 show the maximum liquefaction depths in presence of rubble mound breakwaters with two different submerged berms characterized by $h_B/h_T = 0.59$, $L_B/L_W = 0.17$ (Figure 3.15) and $h_B/h_T = 0.59$, $L_B/L_W = 0.30$ (Figure 3.16), respectively.

The inspection of Figures 3.15 and 3.16 reveals the positive effects of submerged berms deployment on the reduction of momentary liquefaction depth. From the comparison between Figures 3.15 and 3.14 it appears that even though $d_{max_{int}}$ remains the same, $\bar{d}_{int}$ decreases down to 1.16 m, less than what is achieved in absence of berm (i.e. 1.38 m).

A similar consideration applies for $\bar{d}_{ext}$ that drops down to 0.54 m. The big picture description further improves looking

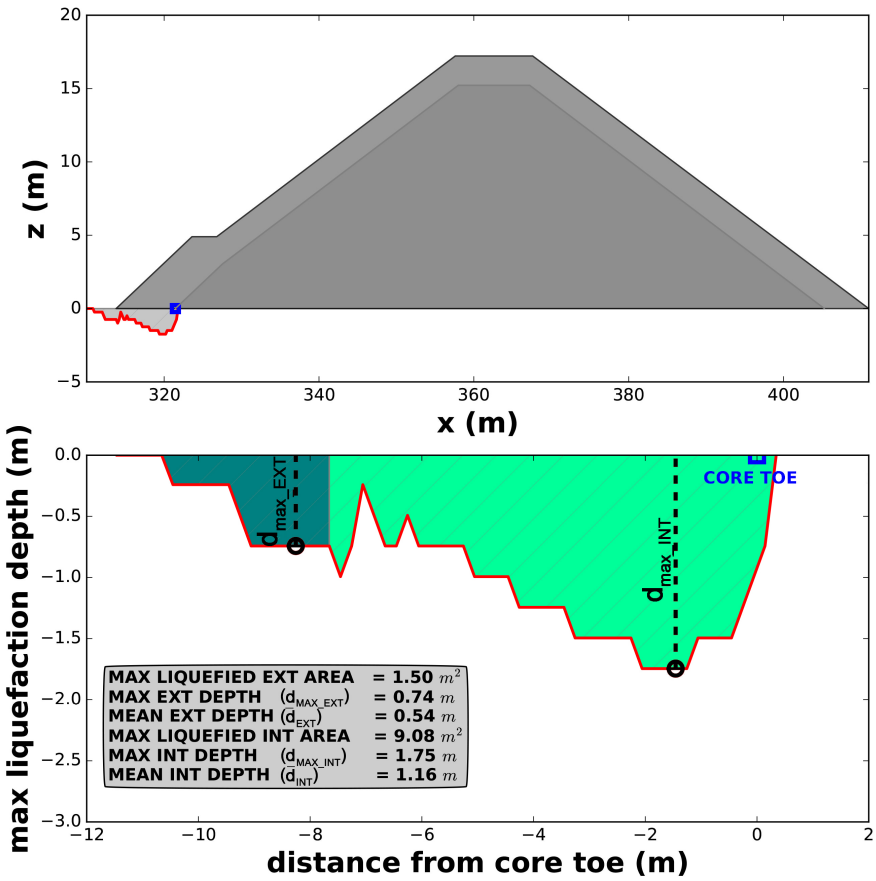

Figure 3.15: Wave-induced momentary liquefaction with reference to breakwater with submerged berm characterized by $h_B/h_T = 0.59$ and $L_B/L_W = 0.17$. Upper panel: momentary liquefaction maximum depth around and beneath the structure. Lower panel: zoom of the momentary liquefaction maximum area splits into two subareas, according to the location of the liquefaction occurrences. Dark green subarea refers to maximum liquefaction depth in front of the structure, up to the breakwater toe. Light green subarea refers to maximum liquefaction depth beneath the structure.

at Figure 3.16. The deployment of a longer submerged berm implies a reduction of $d_{max_{int}}$ that drops down to 1.24 m as well as $\bar{d}_{int}$ that is equal to 0.64 m. In contrast, $d_{max_{ext}}$ and $\bar{d}_{ext}$ grow up reaching values equal to 0.99 m and 0.77 m, respectively. The latter phenomenon is likely due to the upward wave-induced pore pressure gradient rather than to a reduced initial vertical stress distribution, in view of the increased distance from the breakwater core. Looking again at Figure 3.14, it appears

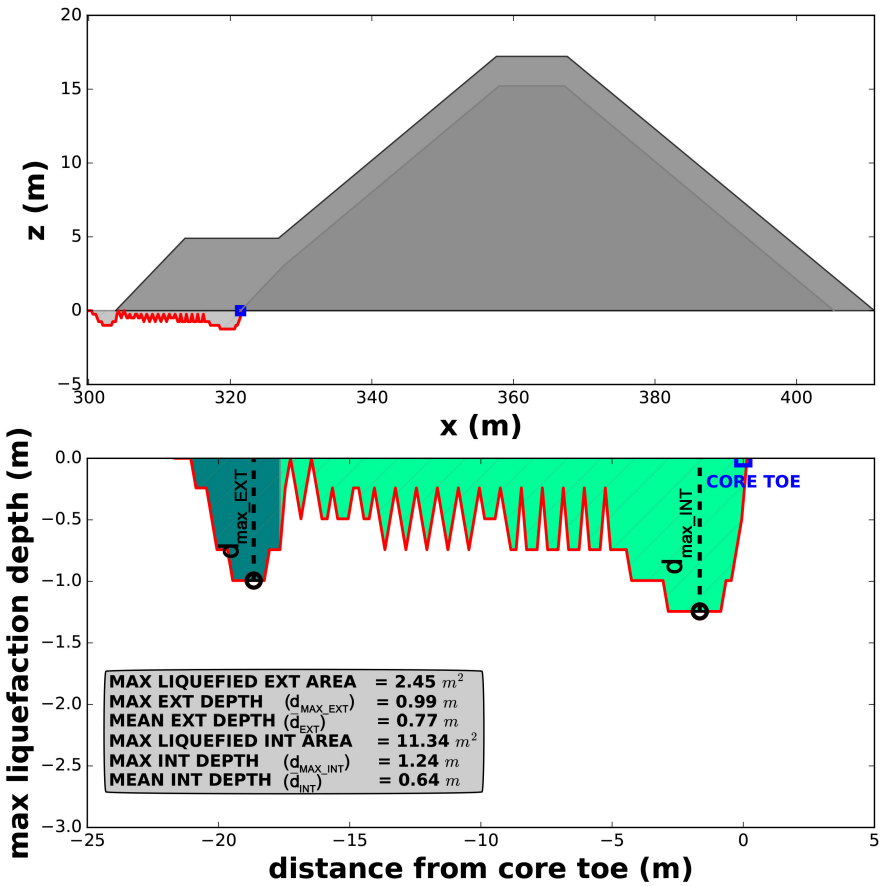

Figure 3.16: Wave-induced momentary liquefaction with reference to breakwater with submerged berm characterized by $h_B/h_T = 0.59$ and $L_B/L_W = 0.30$. Upper panel: momentary liquefaction maximum depth around and beneath the structure. Lower panel: zoom of the momentary liquefaction maximum area splits in two subareas, according to the location of the liquefaction occurrences. Dark green subarea refers to maximum liquefaction depth in front of the structure, up to the breakwater toe. Light green subarea refers to maximum liquefaction depth beneath the structure.

that the maximum liquefied area for the straight sloped rubble mound breakwater is lower if compared to the liquefied areas of Figures 3.15 and 3.16 where submerged berms are employed. Of course, this is expected, since the contact length among the seabed and the structure increases as the berm length increases. However, this does not imply a growth of potential structure failure. Indeed, the longer the berm, the lower the momentary liquefaction probability near the breakwater core, and the higher

the momentary liquefaction probability at the toe of the berm, where the stability of the armor layer is not compromised.

This concept could be better caught looking at the upper panel of Figure 3.17, where d represents the ratio of $\bar{d}_{ext}$ to $\bar{d}_{int}$, as a function of the dimensionless berm length L_B/L_W. Except for the lowest berms (i.e. characterized by $h_B/h_T = 0.9$), the lengthening of the berm tends to push away the liquefaction probability from the zone beneath the breakwater to the area in front of the structure. Just for instance, the longest berms characterized by the ratio h_B/h_T equal to 0.49 and 0.59, lead to $d^* > 1$, i.e. $\bar{d}_{ext} > \bar{d}_{int}$. Nevertheless, the positive effects of the berm lengthening do not apply for the lowest berms, for which d^* remains almost constant varying the berm length.

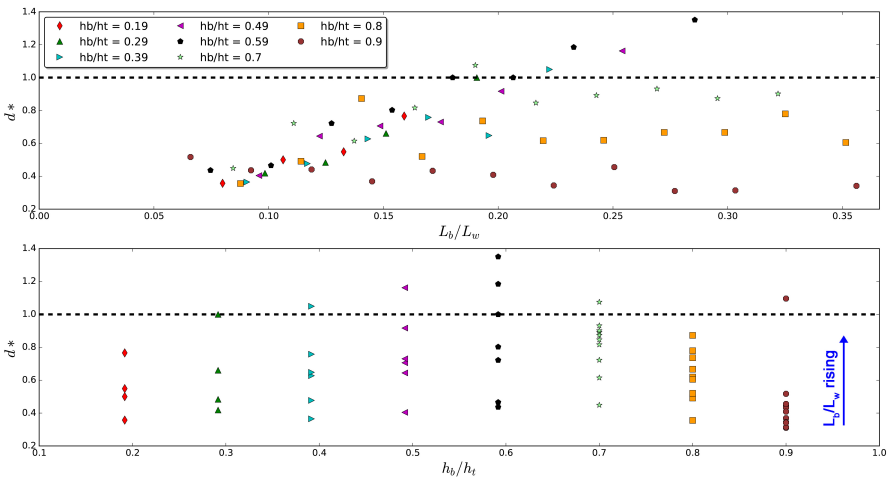

Figure 3.17: Variation of d^*, (i.e. the ratio $\bar{d}_{ext}/\bar{d}_{int}$) as a function of the dimensionless berm length (L_B/L_W , upper panel) and of the dimensionless water depth over the berm (h_B/h_T , lower panel).

The inspection of the lower panel of Figure 3.17 confirms that within the framework of long berms (i.e. roughly $L_B/L_W > 0.20$), the best performances belong to those marked by h_B/h_T equal to 0.49 and 0.59. For short berms, roughly marked $L_B/L_W \leq 0.1$, d^* is almost constant for different dimensionless water depth over the berm h_B/h_T values, i.e. a variation of the berm height does not induce appreciable modification on the area where liquefaction phenomena are likely to occur.

By focusing on the general behavior of submerged berms in influencing the liquefaction phenomena, the evaluation of the mean maximum liquefaction depth d_m, computed considering the whole liquefied area, could be helpful. By taking the mean maximum liquefied depth (d_{m0}), achieved in presence of a straight sloped conventional breakwater without a berm as reference, Figure 3.18 shows the variation of the ratio d_m/d_{m0} as a function of the dimensionless berm length L_B/L_W (upper panel) and of the dimensionless water depth over the berm h_B/h_T (lower panel).

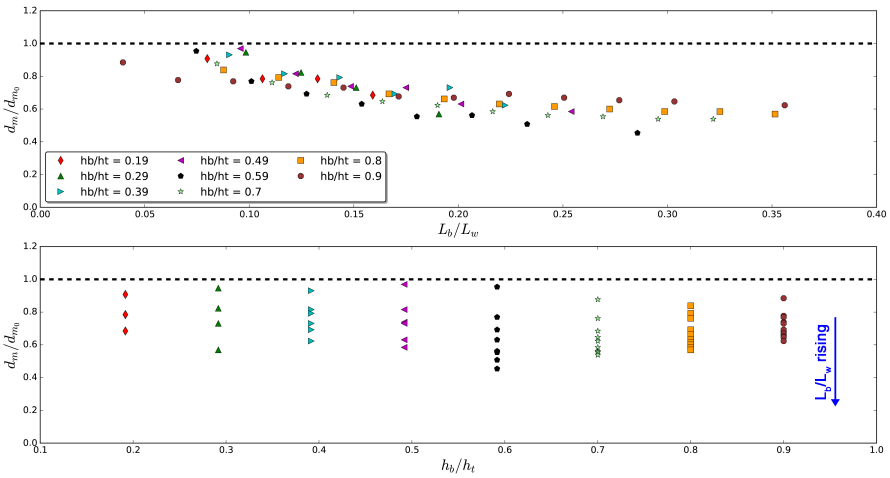

Figure 3.18: Variation of the normalized mean maximum liquefaction depth d_m/d_{m0} as a function of the dimensionless berm length (L_B/L_W, upper panel) and of the dimensionless water depth over the berm (h_B/h_T, lower panel).

In particular, from the inspection of the upper panel of Figure 3.18 it is confirmed that, for the same water depth over the berm, the longer the berms, the higher the reduction of liquefaction depths around and beneath the structure. It has to be emphasized that even though high berms (i.e. characterized by lower values of h_B/h_T) strongly affect the wave propagation (see Chapter 2), the strongest influence on the momentary liquefaction occurrence belongs again to the berms characterized by the ratio $h_B/h_T = 0.59$. Higher berms tend to better attenuate the wave-induced pore pressure at the seabed interface, however, being heavier than the low ones, they enhance a stronger

initial vertical effective stress reduction in the unloaded areas, i.e. where the armour elements are not in direct contact with the seabed. On the other hand, low berms (i.e. characterized by the ratio h_B/h_T ranging from 0.7 up to 0.9), being lighter than the high ones, marginally influence the initial vertical effective stress reduction, while at the same time, have no significant effect on the attenuation of the wave-induced pore pressure at the seabed interface. The influence of low berms length on momentary liquefaction attenuation is therefore negligible, being the ratio d_m/d_{m0} almost constant varying the ratio L_B/L_W. The long berms, characterized by the ratio h_B/h_T = 0.59, could be hence intended as the right balance in terms of seabed pore pressure attenuation and initial vertical effective stress reduction. Therefore, within the range of the tested configurations, they could be regarded as the best design choice to limit the liquefaction phenomena. On a final note, the lower panel of Figure 3.18 confirms that for short berms with a given length, the change of the berm height has no significant influence on the liquefaction occurrences, being the ratio d_m/d_{m0} almost constant varying the ratio h_B/h_T.

4

THE ROLE OF SUBMERGED BERMS ON THE RANDOM WAVE-INDUCED MOMENTARY LIQUEFACTION AROUND RUBBLE MOUND BREAKWATERS

The Chapter is aimed to evaluate the effects of random waves on the momentary liquefaction around and beneath rubble mound breakwaters with submerged berms. It begins with the introduction to the topic, including also a literature review. The following sections describe the carried out numerical investigations and the achieved results as well, specifying that, within the evaluation of momentary liquefaction occurrences, the usage of representative regular wave instead of irregular waves, could lead to an underestimation of the soil portion potentially affected by momentary liquefaction.

4.1 INTRODUCTION

The design of rubble mound breakwaters is aimed to ensure structural response to hydraulic loading, by tackling the actions of both waves and currents. The structural stability of such structures is then achieved by selecting the armor unit size, by adopting one of the many empirical methods available in literature.

In this regard, Chapter 2 shows that it may be appropriate to modify the straight slopes of conventional breakwaters, by deploying a submerged berm marked by higher length than usual, in order to increase the stability of the rocks in the armor layer.

Further to the structural response, in designing rubble mound breakwaters, the soil response and its effects on the foundation stability must be assessed. Indeed, the stability of such structures

can be threatened also by geotechnical causes, as the wave-induced liquefaction.

In this context, Chapter 3 shows that the introduction of a submerged berm is valuable also in reducing wave-induced momentary liquefaction phenomena, if compared to the case of straight sloped conventional rubble mound breakwaters. In particular, a parametric study by varying the berm geometry in terms of its length and its height has been carried out, keeping constant the elastic properties of the soil, the water depth and the offshore regular wave conditions, in order to identify the best berm configuration in attenuating momentary liquefaction occurrences.

The rationale adopted in Chapter 3 imposed a comparison among different berm configurations for the same wave conditions, which make reasonable the regular waves assumption, despite irregular waves always occur in the real ocean environments.

To date, only a few research studies considered the effect of random waves on the soil responses and liquefaction processes.

Liu and Jeng, (2006) developed a semi-analytical solution for random wave-induced soil response and seabed liquefaction. In particular, the influence of random wave loading on the soil response was investigated and compared with the corresponding representative regular wave results, carrying out a parametric study by varying the wave height and period, the seabed thickness, the degree of saturation as well as the soil permeability.

Xu and Dong, (2011) carried out a numerical study about the liquefaction occurrences due to irregular waves, by identifying the liquefaction depths in form of probability distributions. Their results indicate that the random wave-induced liquefaction depth is much larger than the corresponding to regular waves with the equivalent wave height (i.e. significant wave height equal to the wave height of regular wave train).

The aforementioned studies, although underline how important is the use of irregular wave conditions in assessing the maximum liquefaction depth and its implications in the design process, did not include the presence of any structure in

their works. Therefore, the aim of this Chapter is to investigate the random-wave-induced momentary liquefaction probability around and beneath rubble mound breakwaters with submerged berm. In order to analyze the influence of random wave loading on the momentary liquefaction phenomena, a comparison with the corresponding representative regular wave results (i.e. significant wave height equal to the wave height of regular wave train)., showed in Chapter 3, has been carried out by following the work of Xu and Dong, (2011). From an energetic point of view, it has to be stressed that the considered irregular waves trains are more energetic than the corresponding refular wave train. In particular, three ad-hoc domains have been selected: a straight sloped conventional rubble mound breakwater without a berm and two rubble mound breakwaters with submerged berms characterized by h_B/h_T = 0.59, L_B/L_W = 0.35, and h_B/h_T = 0.19, L_B/L_W = 0.35, respectively (being h_T the water depth at the toe of the berm, h_B the water depth over the berm, L_B the berm length and L_W the wave length at the toe of the berm). The first one has been chosen for comparison purposes. This is to assess if also under random-wave loading, the introduction of a submerged berm leads to a reduction of the momentary liquefaction probability, if compared to the case of straight sloped conventional breakwaters without a berm, as for regular wave conditions (see Chapter 3). The second domain represents the best design choice to prevent liquefaction phenomena, under the regular wave conditions, at least within the considered configurations. Then, it is important to evaluate if, with this geometry, the momentary liquefaction probability continues to be low. The last domain has been selected to confirm that also under irregular waves, the change of the berm height has no significant influence on the liquefaction occurrences.

As done for the regular wave conditions, the random-wave induced dynamic seabed pressure has been evaluated by means of SWASH (Zijlema et al., 2011) and the seabed response has been evaluated by means of the poro-elastic soil model developed by Li et al., (2018). The seabed dynamic pressure has been used as one-way coupling boundary condition in order

to simulate the interaction between multiple physical phases. The detailed description of the mathematical models and the coupling algorithm can be found in Chapter 3.

4.2 MODEL CALIBRATION AND VALIDATION

Both the adopted numerical models were already subjected to a calibration and validation phases, as described in the Section 3.4.

Since the simulated domains are equal to those already implemented, it is reasonable to extend the calibration and validation achievements to this study. Therefore, for the numerical model SWASH, used to compute the random-wave induced seabed pressure, it has been decided to adopt a computational grid spatial resolution equal to 0.2 m, which suffices to accomplish reliable numerical accuracy. The model ability to catch the effects of submerged berms on the incident wave transformation was already validated, through a comparison with experimental data (e.g. see Figure 2.9 of Section 2.5). The reliability of the results given by SWASH, in terms of dynamic seabed pressure was already verified through a comparison with the ones obtained by using a numerical two-phase flow solver (Higuera et al., 2014), as shown in Figure 3.6.

The seabed response to the wave-induced seabed pressures has been evaluated by using an ad-hoc anisotropic poro-elastic soil solver (Li et al., 2018), developed within the OpenFOAM framework. A grid convergence study was already carried out, consequently $2,7 \times 10^5$ grid points have been used to evaluate the soil response within the study described herein. The capability of the solver to catch the wave-induced seabed response was already validated by Li et al., 2018, through a comparison with experimental data provided by Tsai and Lee, (1995) (e.g. see their Figure 2,3 and 4).

4.3 NUMERICAL INVESTIGATION

Once recognized the potential damage resulting from the liquefaction phenomena, several research studies have been carried out on the soil response to the wave-induced seabed pressure around marine structures. Nevertheless, almost all have been referred to regular wave conditions. Under the random real wave assumption, the soil response to the wave-induced seabed pressure may, however, be dissimilar. Therefore, the aim of this work is to evaluate also how different could be the soil response, in terms of liquefaction depths, by considering both irregular and regular wave conditions. The former results are those shown in Chapter 3, considering regular waves characterized by H = 4m and T = 8s.

In order to compare the soil responses induced by regular and irregular waves, representative wave parameters (i.e. significant or spectral wave height and peak or mean wave period) must be chosen. Comparing the pore pressure accumulation data from experimental measurements, Sumer et al., (1999) found that the best comparison with regular wave results was given by a representative wave height $H_r = H_s/2$ and wave period $T_r = T_z$, where the quantity $H_s/2$ could be interpreted as the equivalent wave height of the irregular waves, whilst T_z is the mean zero upcrossing period.

The same approach was adopted by Liu and Jeng, (2007).

Liu and Jeng, (2006), instead, considered the significant wave height H_s and significant wave period T_s as the representative wave parameters.

Unlike the previous works, in this research study, the spectral wave height H_{m0} and the peak period T_p have been used for comparison purposes. In this regard, the time-series of surface elevation has been derived synthesizing Jonswap spectrum (γ = 3.3), by adopting H_{m0} = 4m and T_p = 8s (see Figure 4.1).

Hence, assuming irregular waves condition, three ad-hoc domains have been selected from those described in Section 2.5: a straight sloped conventional rubble mound breakwater without a berm and two rubble mound breakwaters with submerged

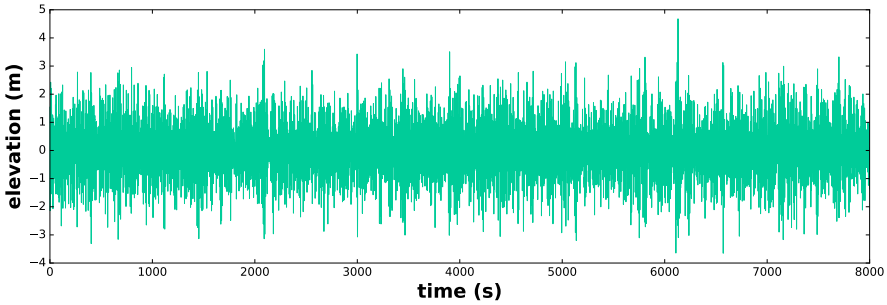

Figure 4.1: Time history of the simulated irregular waves, equal for each simulation. The represented water levels do not take into account the offshore water depth h = 12 m.

berms characterized by h_B/h_T = 0.59, L_B/L_W = 0.35, and h_B/h_T = 0.19, L_B/L_W = 0.35, respectively (being h_T the water depth at the toe of the berm, h_B the water depth over the berm, L_B the berm length and L_W the wave length at the toe of the berm, see Figure 3.9).

In all cases the absence of a transition layer beneath the armour layer and the berm is assumed by considering the stones in direct contact with the seabed, loading the soil in a discontinuous way. For each simulation, the total length of the computational domain is set at 411 m and the cell size in the x-direction at 0.2 m. To properly describe the wave frequency dispersion, the model is run with three layers in the vertical direction. The offshore boundary is considered as weakly reflective and a water level time series, reproducing irregular waves, is imposed (see Figure 4.1). For each test almost 1000 waves have been simulated, in order to reproduce the correct statistical distribution of individual wave heights It has to be emphasized that the numeber of reproduced waves are quite larger than the number of waves considered within the frame of regular wave trains. At the onshore boundary, the Sommerfeld radiation condition is applied. Following the same rationale adopted within the Chapter 3, for each of the three tested configurations, the computed seabed dynamic pressure time series have been collected and applied as coupling boundary condition for the anisotropic Biot's porous soil model. For comparison purposes, the numerical domain of the porous seabed and the porous

seabed parameters are identical to that implemented under the regular wave conditions. Therefore, the domain is 450 m long and 30 m thick. The soil porosity n is set to 0.3 and the saturation factor S_r is to 0.975. The anisotropic parameter settings are shown in Table 3.2. The boundary conditions of the seabed domain are specified as follows:

- at the wave-seabed and the porous structure-seabed interfaces, the effective soil stresses vanish, hence the soil has zero traction at the seabed surface. The pore pressure, at the aforementioned interfaces, is equal to the dynamic wave pressure acting on the seabed and beneath the porous structure;
- at the bottom and lateral boundaries of the seabed, the soil skeleton is allowed to slip and the normal pore pressure gradient is zero.

4.4 RESULTS

4.4.1 *Consolidation*

As described in Chapter 3, the determination of the initial consolidation status is an essential step for the evaluation of the wave-induced soil liquefaction probability. Hence, the vertical effective stresses $\sigma_z^{'}$, computed at the end of the consolidation process, have been used as an initial condition for the momentary liquefaction analysis. For a simulated test case with h_B/h_T = 0.19 and L_B/L_W = 0.35, Figure 4.2 shows the distribution of the vertical effective stresses $\sigma_z^{'}$ in the soil (a negative value of $\sigma_z^{'}$ indicates the compression of the soil skeleton), whilst Figure 4.3 shows the vertical soil displacement U_z, both evaluated at the completion of the consolidation process. A negative value of U_z indicates that the soil skeleton is compressed and moves downward.

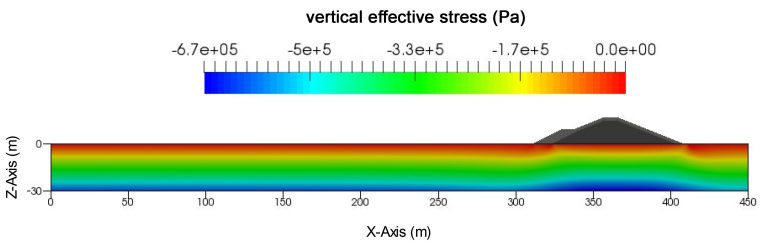

Figure 4.2: Vertical effective stress $\sigma_z^{'}$ after the completion of the consolidation process for a breakwater with submerged berm characterized by $h_B/h_T = 0.19$ and $L_B/L_W = 0.35$.

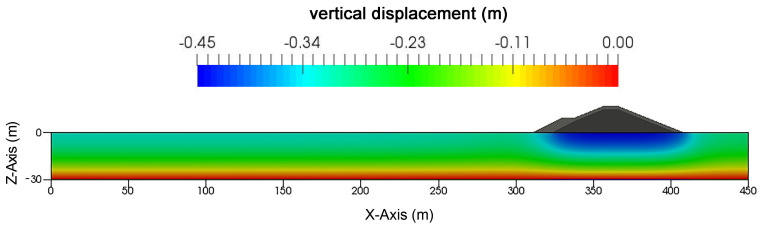

Figure 4.3: Vertical soil displacement U_z after the completion of the consolidation process for a breakwater with submerged berm characterized by $h_B/h_T = 0.19$ and $L_B/L_W = 0.35$.

4.4.2 *Momentary liquefaction analysis*

As formerly detailed in Chapter 3, in order to take into account the gravitational effects deriving from the deployment of any structure (i.e. a rubble mound breakwater), the adopted momentary liquefaction criterion reads as follows:

$$p(z,t) - p(0,t) \geq \sigma_z^{'} \tag{4.1}$$

where $p(z,t)$ is the pore pressure in the seabed, $p(0,t)$ is the pore pressure at the seabed, whilst $\sigma_z^{'}$ represents the initial vertical effective stress induced by the gravitational forces from the consolidation process.

With a view to understanding how different could be the soil response in terms of momentary liquefaction, achieved under the action of regular and irregular waves, the percentiles of liquefaction depths have been evaluated.

Figures 4.4, 4.5 and 4.6 show the percentiles of the regular wave-induced momentary liquefaction depths d_i (where i represents indeed the percentile), achieved in presence of a straight sloped conventional rubble mound breakwater without a berm (see Figure 4.4) and the two rubble mound breakwaters with submerged berms characterized by $h_B/h_T = 0.59$, $L_B/L_W = 0.35$ (see Figure 4.5), and $h_B/h_T = 0.19$, $L_B/L_W = 0.35$ (see Figure 4.6), respectively.

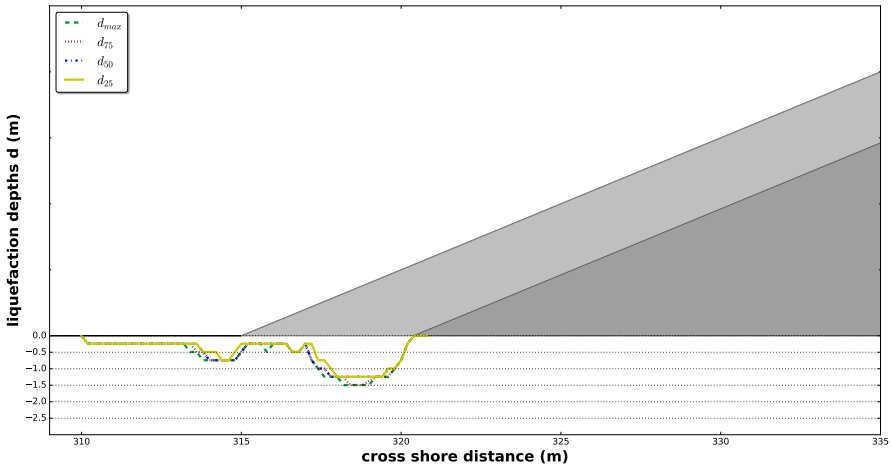

Figure 4.4: Regular wave-induced momentary liquefaction depth percentiles with reference to a breakwater without submerged berm.

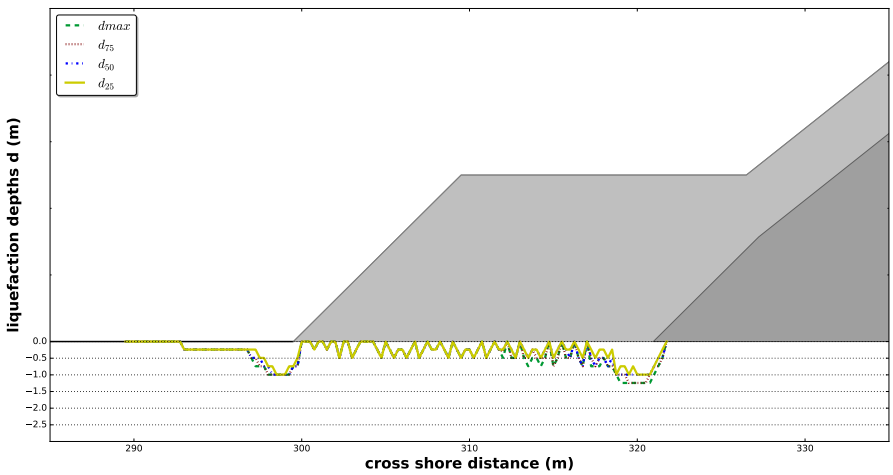

Figure 4.5: Regular wave-induced momentary liquefaction depth percentiles with reference to a breakwater with submerged berm characterized by $h_B/h_T = 0.59$, $L_B/L_W = 0.35$.

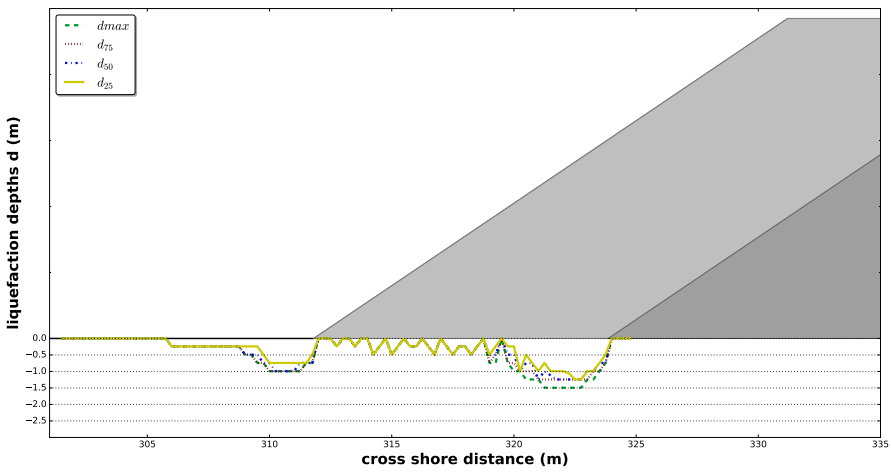

Figure 4.6: Regular wave-induced momentary liquefaction depth percentiles with reference to a breakwater with submerged berm characterized by h_B/h_T = 0.19, L_B/L_W = 0.35.

From all the aforementioned Figures, it appears that, with a reference to the selected configuration, the momentary liquefaction depths assume almost the same values for different considered percentiles. This is not surprising, since the results refer to momentary liquefaction depths achieved under regular wave conditions (H = 4, T = 8). The wave regularity entails that in each point of the seabed, momentary liquefaction depths vary periodically, achieving the same maximum values over the time.

Figures 4.7, 4.8 and 4.9 show, instead, the random wave-induced momentary liquefaction depths as well as the representative regular wave-induced momentary liquefaction depths, for the three different configurations previously mentioned.

In view of the regular wave-induced momentary liquefaction depths invariance for different considered percentile values, the 50th percentile (i.e d_{50REG}, black line) has been selected for comparison purposes.

Looking at Figures 4.7, 4.8 and 4.9, it appears the advantages concerning the deployment of submerged berms. In fact, for the case devoid of submerged berm, the maximum momentary liquefaction depth beneath the armor layer reaches 2.5 m, the greatest value among the simulated configurations, and, by the way, almost constant within the soil portion affected by

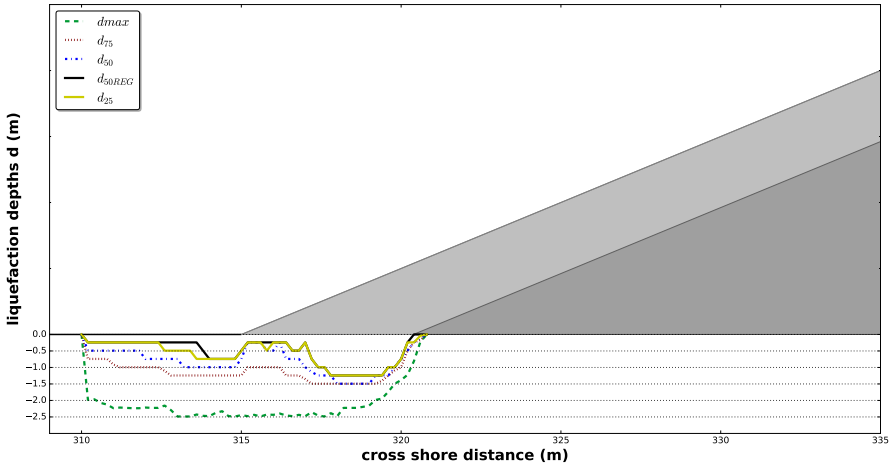

Figure 4.7: Random wave-induced momentary liquefaction depth percentiles with reference to a breakwater without submerged berm.

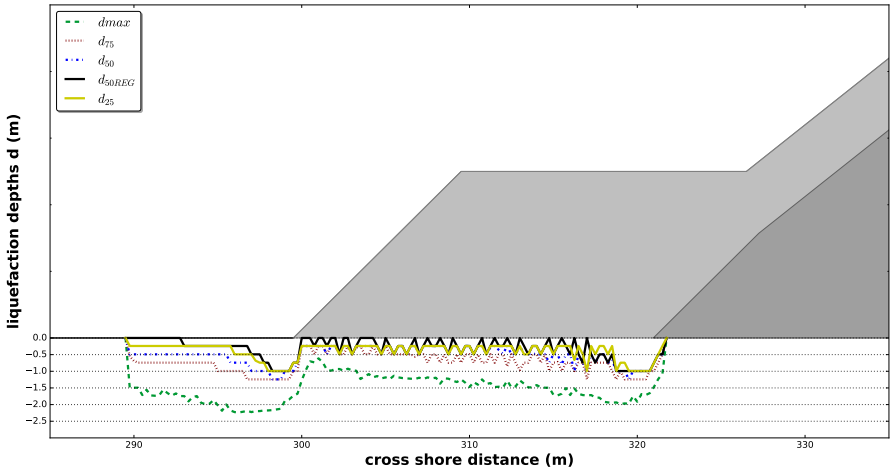

Figure 4.8: Random wave-induced momentary liquefaction depth percentiles with reference to a breakwater with submerged berm characterized by $h_B/h_T = 0.59$, $L_B/L_W = 0.35$.

liquefaction. Therefore, even under irregular wave conditions, it is confirmed that the presence of submerged berms tends to attenuate momentary liquefaction occurrences.

Moreover, it is confirmed that the lengthening of the berm tends to move the location where liquefaction probability is high, from the zone beneath the breakwater to the area in front of the structure (see Figure 4.8). It could be appreciated the main role of submerged berms, able to protect the armor layer from momentary liquefaction occurrences and scouring process con-

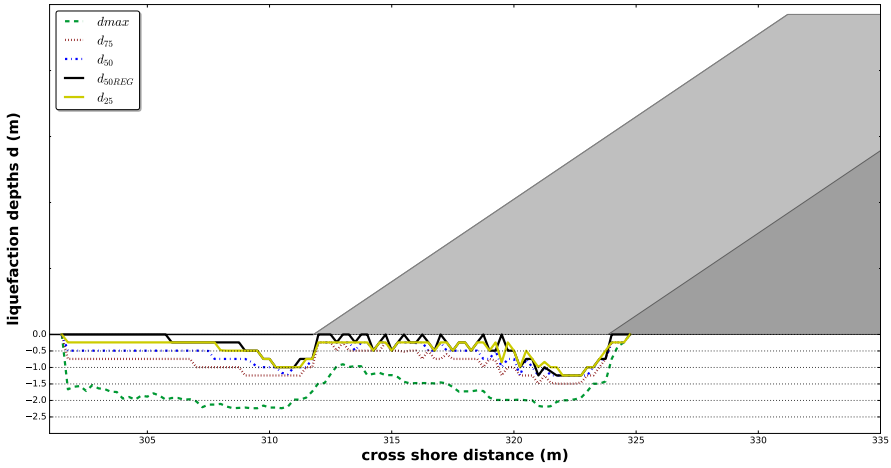

Figure 4.9: Random wave-induced momentary liquefaction depth percentiles with reference to a breakwater with submerged berm characterized by $h_B/h_T = 0.19$, $L_B/L_W = 0.35$.

sequently. Basically, they could be intended as the expendable part of the structure.

Looking again at the aforementioned Figures, it appears that the momentary liquefaction phenomena are more influenced by changing the berm length rather than the berm height. The cases represented in Figure 4.8 and 4.9, show different results in terms of momentary liquefaction depths in front of the berm, being larger the portion of soil affected by liquefaction in case of submerged berm characterized by $h_B/h_T = 0.19$. Nevertheless, the liquefaction depths occurring beneath the berm are comparable. Then, the change of the berm height has no significant influence on the liquefaction occurrences.

It has to be stressed that, although the random wave results exhibit similar tendency along the x-axis as the regular wave cases, the random wave-induced momentary liquefaction depths are larger than the corresponding representative regular ones. Indeed, from Figures 4.7, 4.8 and 4.9, it appears that d_i are greater than, or at most equal to d_{50REG}. The reliance on representative regular wave conditions, albeit enables an estimation of momentary liquefaction depths with relative low computational time (it may be sufficient to simulate few regular waves to obtain

stationary results), could lead to an underestimation of the soil portion potentially affected by momentary liquefaction.

A safe design should hence be based on the estimation of momentary liquefaction induced by more severe random waves.

5

CONCLUDING REMARKS

Berms deployed at the toe of conventional rubble mound breakwaters may be useful for various purposes, i.e. (i) to reduce wave loads acting on the breakwater armor elements, (ii) to reduce wave overtopping, (iii) to reduce momentary liquefaction occurrences under the structure, (iv) to protect from the scouring the breakwater toe.

With reference to the first part of the Thesis (see Chapter 2), it has been proposed a new design criterion able to describe the influence of relatively low and long berms on the stability of the rock armor of conventional breakwaters. The design of the berm itself was not tackled herein. A parametric correction factor of the incident significant wave height at the toe of the structure has been provided and included in a well-established design criterion. Basically, the proposed method consists of Equations 2.12 or 2.13, with the correction factor evaluated by means of and parameters of Table 2.5. The proposed method is intended to be general, i.e. valid for deep and shallow waters, and easy to use as it is almost similar to standard criteria with the needing of the further estimation of the correction factor depending upon the berm configuration (i.e. length and water depth) and the incident wave length at the toe of the structures, evaluated by using the peak period. The validity interval of the proposed method spans water depths over the berm (h_B) ranging from $0.09h_T$ up to $0.91h_T$ (being h_T the water depth at the toe of the structure) and berm lengths (L_B) from $(0.282–0.267h_B/h_T)L_W$ up to $0.356L_W$ (being h_B the water depth over the berm and $L_W$the wave length at the toe). The experimental comparison confirmed the reliability of the proposed method by highlighting the importance to use design criteria within their validity ranges.

In relation to the second part of the Thesis (see Chapter 3), the regular wave-induced soil response and the liquefaction prob-

ability around and beneath a rubble mound breakwaters with (and without) submerged berm have been numerically investigated. Two numerical tools have been used for this study: the effects of submerged berms on the dynamic pressure acting on the seabed have been evaluated by means of SWASH, whereas the seabed responses to the regular wave-induced seabed pressures have been evaluated by using an ad-hoc anisotropic poro-elastic soil solver, developed in OpenFOAM (Li et al., 2018). A parametric study has been carried out by changing the berm configuration, to find out their performances in attenuating momentary liquefaction probability, especially under the breakwater core, where a partial failure could lead to a severe damage for the whole structure. For all the tested configurations, the effects of the consolidation process on the wave-induced soil response, have been taken into account. Within the range of the tested configurations, the main conclusions are drawn as follows.

1. The presence of any berm tends to attenuate momentary liquefaction occurrences if compared to the case of a straight sloped conventional breakwater without a berm.

2. Except for the lowest tested berm (i.e. characterized by $h_B/h_T = 0.9$), the lengthening of the berm tends to move the location where liquefaction probability is high, from the zone beneath the breakwater to the area in front of the structure, i.e. where a potential damage does not compromise the structure integrity.

3. High berms tend to better attenuate the wave-induced pore pressure at the seabed interface, however, being heavier than the low ones, they enhance a stronger initial vertical effective stress reduction in the unloaded areas. Consequently, the momentary liquefaction attenuation is limited.

4. Low berms, being lighter than the high ones, slightly influence the initial vertical effective stress reduction, while at the same time, have no significant effects on the attenuation of the wave-induced pore pressure at the seabed

interface. The resulting momentary liquefaction attenuation is limited.

5. The greater momentary liquefaction attenuation is given by long berms characterized by the ratio $h_B/h_T = 0.59$, i.e. an intermediate height within the considered range, at least for the tested wave conditions. They could be intended as the right balance in terms of seabed pore pressure attenuation and initial vertical effective stress reduction. Therefore, they could be regarded as the best design choice to prevent the liquefaction phenomena, within the tested conditions.

With a reference to the last part of the Thesis (see Chapter 4), the effects of irregular waves on the momentary liquefaction around and beneath rubble mound breakwater with (and without) submerged berms have been evaluated. In particular, a numerical study has been carried out by selecting three ad-hoc domains, among those tested under regular wave conditions (see Chapter 3). In this respect, the same numerical tools adopted for the aforementioned parametric study of Chapter 3, have been used. Results indicate that even under irregular wave conditions, the presence of submerged berms tends to attenuate momentary liquefaction occurrences, with the lengthening of the berm that tends to move the location where liquefaction probability is high, from the zone beneath the breakwater to the area in front of the structure. Moreover, the influence of random wave loading on the momentary liquefaction occurrences have been investigated through a comparison with the corresponding representative regular wave results. Due to the wave randomness, the random wave-induced momentary liquefaction depths are larger than the corresponding representative regular ones. This means that for the detection of momentary liquefaction occurrences, the usage of representative regular wave, corresponding to the significant value of random waves, could underestimate the liquefaction depth, determining an unsafe design in the engineering practice.

BIBLIOGRAPHY

Battjes, Jurjen A and Heiko W Groenendijk (2000). "Wave height distributions on shallow foreshores." In: *Coastal engineering* 40.3, pp. 161–182.

Biot, Maurice A (1941). "General theory of three-dimensional consolidation." In: *Journal of applied physics* 12.2, pp. 155–164.

Burcharth, HF and OK Andersen (1995). "On the one-dimensional steady and unsteady porous flow equations." In: *Coastal engineering* 24.3-4, pp. 233–257.

Burcharth, Hans F, Zhou Liu, and Peter Troch (1999). "Scaling of core material in rubble mound breakwater model tests." In: *The International Conference on Coastal and Port Engineering in Developing Countries*. COPEDEC, pp. 1518–1528.

CIRIA/CUR/CETMEF (2007). *The Rock Manual: The use of rock in hydraulic engineering*. Vol. 683. Ciria.

Castellino, M., P. Sammarco, A. Romano, L. Martinelli, P. Ruol, L. Franco, and P. De Girolamo (2018). "Large impulsive forces on recurved parapets under non-breaking waves. A numerical study." In: *Coastal Engineering* 136, pp. 1 –15. ISSN: 0378-3839.

Cengel, Y and J Cimbala (2006). *Fundamentals and Application*. McGraw-Hill, USA.

Chung, SG, SK Kim, YJ Kang, JC Im, and K Nagendra Prasad (2006). "Failure of a breakwater founded on a thick normally consolidated clay layer." In: *Geotechnique* 56.6, pp. 393–409.

De Groot, MB, MD Bolton, P Foray, P Meijers, AC Palmer, R Sandven, A Sawicki, and TC Teh (2006). "Physics of liquefaction phenomena around marine structures." In: *Journal of Waterway, Port, Coastal, and Ocean Engineering* 132.4, pp. 227–243.

Di Risio, M., I. Lisi, G.M. Beltrami, and P. De Girolamo (2010). "Physical modeling of the cross-shore short-term evolution of protected and unprotected beach nourishments." In: *Ocean Engineering* 37.8, pp. 777 –789. ISSN: 0029-8018.

Elsafti, H. and H. Oumeraci (2016). "A numerical hydro-geotechnical model for marine gravity structures." In: *Computers and Geotechnics* 79, pp. 105 –129. ISSN: 0266-352X.

Franco, Leopoldo (1994). "Vertical breakwaters: the Italian experience." In: *Coastal Engineering* 22.1-2, pp. 31–55.

Frigaard, Peter and Michael Brorsen (1995). "A time-domain method for separating incident and reflected irregular waves." In: *Coastal Engineering* 24.3-4, pp. 205–215.

Frostick, Lynne E, Stuart J McLelland, and Theresa G Mercer (2011). *Users guide to physical modelling and experimentation: Experience of the HYDRALAB network*. CRC Press.

Goda, Yoshimi (2010). "Reanalysis of regular and random breaking wave statistics." In: *Coastal Engineering Journal* 52.01, pp. 71–106.

Hald, Tue (1998). "Wave induced loading and stability of rubble mound breakwaters." PhD thesis. Hydraulics & Coastal Engineering Laboratory, Department of Civil Engineering, Aalborg University.

Hedges, TS (1984). "The core and underlayers of a rubble-mound structure." In: *BREAKWATERS Design & Construction*. Thomas Telford Publishing, pp. 99–106.

Herrera, Maria P., Jorge Molines, and Josep R. Medina (2016). "Hydraulic stability of nominal and sacrificial toe berms for mound breakwaters on steep sea bottoms." In: *Coastal Engineering* 114.Supplement C, pp. 361 –368. ISSN: 0378-3839. DOI: `https://doi.org/10.1016/j.coastaleng.2016.05.006`.

Herrera, Maria P, M Esther Gómez-Martín, and Josep R Medina (2017). "Hydraulic stability of rock armors in breaking wave conditions." In: *Coastal Engineering* 127, pp. 55–67.

Higuera, Pablo, Javier L. Lara, and Inigo J. Losada (2013). "Realistic wave generation and active wave absorption for Navier–Stokes models: Application to OpenFOAM®." In: *Coastal Engineering* 71, pp. 102 –118. ISSN: 0378-3839.

– (2014). "Three-dimensional interaction of waves and porous coastal structures using OpenFOAM®. Part I: Formulation and validation." In: *Coastal Engineering* 83, pp. 243 –258. ISSN: 0378-3839.

Hsu, J. R. C. and D. S. Jeng (1994). "Waveinduced soil response in an unsaturated anisotropic seabed of finite thickness." In: *International Journal for Numerical and Analytical Methods in Geomechanics* 18.11, pp. 785–807.

Hudson, Robert Y (1959). "Laboratory investigation of rubble-mound breakwaters." In: *Reprint of the original paper as published in the Journal of the Waterways and Harbors Division of ASCE, proceedings paper 2171*.

Hughes, Steven A (1993). *Physical models and laboratory techniques in coastal engineering*. Vol. 7. World Scientific.

Hur, Dong-Soo, Chang-Hoon Kim, and Jong-Sung Yoon (2010). "Numerical study on the interaction among a nonlinear wave, composite breakwater and sandy seabed." In: *Coastal Engineering* 57.10, pp. 917–930.

Iribarren, R (1938). "Una fórmula para el cálculo de diques de escollera." In: *Pasajes*.

Jeng, D.-S. and J.H. Ye (2012). "Three-dimensional consolidation of a porous unsaturated seabed under rubble mound breakwater." In: *Ocean Engineering* 53, pp. 48 –59. ISSN: 0029-8018.

Jeng, D.-S., J.-H. Ye, J.-S. Zhang, and P.L.-F. Liu (2013). "An integrated model for the wave-induced seabed response around marine structures: Model verifications and applications." In: *Coastal Engineering* 72, pp. 1 –19. ISSN: 0378-3839.

Jeng, Dong-Sheng (1997). "Soil response in cross-anisotropic seabed due to standing waves." In: *Journal of geotechnical and geoenvironmental engineering* 123.1, pp. 9–19.

– (2012). *Porous models for wave-seabed interactions*. Springer Science & Business Media.

Kjekstad, O. and T. Lunne (1981). "Soil parameters used for design of gravity platforms in the North Sea." In: *Applied Ocean Research* 3.2, pp. 50 –58. ISSN: 0141-1187.

Kudella, M., H. Oumeraci, M. B. de Groot, and P. Meijers (2006). "Large-Scale Experiments on Pore Pressure Generation underneath a Caisson Breakwater." In: *Journal of Waterway, Port, Coastal, and Ocean Engineering* 132.4, pp. 310–324.

Lamberti, A., R. Archetti, M. Kramer, D. Paphitis, C. Mosso, and M. Di Risio (2005). "European experience of low crested

structures for coastal management." In: *Coastal Engineering* 52.10. Low Crested Structures and the Environment, pp. 841–866. ISSN: 0378-3839.

Li, Yuzhu, Muk Chen Ong, and Tian Tang (2018). "Numerical analysis of wave-induced poro-elastic seabed response around a hexagonal gravity-based offshore foundation." In: *Coastal Engineering* 136, pp. 81–95.

Liu, Haijiang and Dong-S Jeng (2006). "Response of a porous seabed under random wave loading." In: *25th International Conference on Offshore Mechanics and Arctic Engineering*. American Society of Mechanical Engineers, pp. 85–93.

Liu, Haijiang and Dong-Sheng Jeng (2007). "A semi-analytical solution for random wave-induced soil response and seabed liquefaction in marine sediments." In: *Ocean Engineering* 34.8, pp. 1211 –1224. ISSN: 0029-8018. DOI: https://doi.org/10.1016/j.oceaneng.2006.07.004.

Mansard, Etienne PD and ER Funke (1980). "The measurement of incident and reflected spectra using a least squares method." In: *Coastal Engineering 1980*, pp. 154–172.

Mase, Hajime, T Sakai, and M Sakamoto (1994). "Wave-induced porewater pressures and effective stresses around breakwater." In: *Ocean Engineering* 21.4, pp. 361–379.

Melby, Jeffrey A. and Nobuhisa Kobayashi (1998). "Progression and Variability of Damage on Rubble Mound Breakwaters." In: *Journal of Waterway, Port, Coastal, and Ocean Engineering* 124.6, pp. 286–294.

Nago, Hiroshi, Shiro Maeno, Takayuki Matsumoto, Yasushi Hachiman, et al. (1993). "Liquefaction and densification of loosely deposited sand bed under water pressure variation." In: *The Third International Offshore and Polar Engineering Conference*. International Society of Offshore and Polar Engineers.

Nataraja, MS and HS Gill (1983). "Ocean wave-induced liquefaction analysis." In: *Journal of Geotechnical Engineering* 109.4, pp. 573–590.

Oumeraci, H (1994). "Review and analysis of vertical breakwater failures—lessons learned." In: *Coastal Engineering* 22.1-2, pp. 3–29.

Pasquali, D., M. Di Risio, and P. De Girolamo (2015). "A simplified real time method to forecast semi-enclosed basins storm surge." In: *Estuarine, Coastal and Shelf Science* 165, pp. 61 –69. ISSN: 0272-7714.

Smit, Pieter, Marcel Zijlema, and Guus Stelling (2013). "Depth-induced wave breaking in a non-hydrostatic, near-shore wave model." In: *Coastal Engineering* 76, pp. 1–16.

Smith, Greg, Ida Wallast, and Marcel RA van Gent (2003). "Rock slope stability with shallow foreshores." In: *Coastal Engineering 2002: Solving Coastal Conundrums*. World Scientific, pp. 1524–1536.

Sui, Titi, Jinhai Zheng, Chi Zhang, Dong-Sheng Jeng, Jisheng Zhang, Yakun Guo, and Rui He (2017). "Consolidation of unsaturated seabed around an inserted pile foundation and its effects on the wave-induced momentary liquefaction." In: *Ocean Engineering* 131, pp. 308–321.

Sumer, B Mutlu (2014). *Liquefaction around marine structures*. World Scientific.

Sumer, B.M, J Fredsøe, S Christensen, and M.T Lind (1999). "Sinking/floatation of pipelines and other objects in liquefied soil under waves." In: *Coastal Engineering* 38.2, pp. 53 –90. ISSN: 0378-3839. DOI: https://doi.org/10.1016/S0378-3839(99)00024-1.

Suzuki, Tomohiro, Corrado Altomare, William Veale, Toon Verwaest, Koen Trouw, Peter Troch, and Marcel Zijlema (2017). "Efficient and robust wave overtopping estimation for impermeable coastal structures in shallow foreshores using SWASH." In: *Coastal Engineering* 122, pp. 108–123.

The SWASH team (2017). *SWASH user manual, version 4.01*.

Thompson, DM and RM Shuttler (1975). "Riprap design for wind wave attack." In: *A laboratory study in random waves. Wallingford, EX* 707.

Tsai, CP (1995). "Wave-induced liquefaction potential in a porous seabed in front of a breakwater." In: *Ocean Engineering* 22.1, pp. 1–18.

Tsai, Ching-Piao and Tsong-Lin Lee (1995). "Standing wave induced pore pressures in a porous seabed." In: *Ocean Engineering* 22.6, pp. 505 –517. ISSN: 0029-8018.

USACE (1975). "Shore protection manual." In: *U.S. Army Engineer Waterways Experiment Station, Vicksburg, Mississippi*.

– (1984). "Shore protection manual." In: *U.S. Army Engineer Waterways Experiment Station, Vicksburg, Mississippi*.

Ulker, M.B.C., M.S. Rahman, and M.N. Guddati (2010). "Wave-induced dynamic response and instability of seabed around caisson breakwater." In: *Ocean Engineering* 37.17, pp. 1522 –1545. ISSN: 0029-8018.

Vafai, K. and C.L. Tien (1981). "Boundary and inertia effects on flow and heat transfer in porous media." In: *International Journal of Heat and Mass Transfer* 24.2, pp. 195 –203. ISSN: 0017-9310.

Van Der Meer, Jentsje W (1987). "Stability of breakwater armour layers—design formulae." In: *Coastal engineering* 11.3, pp. 219–239.

– (1988). "Rock slopes and gravel beaches under wave attack." In:

Van Der Meer, Jentsje (2011). "Design aspects of breakwaters and sea defences." In: *5th SCACR 2011 International Short Conference on Applied Coastal Research*, p. 3.

Vidal, Cesar, Francisco L Martin, V Negro, X Gironella, B Madrigal, and J García-Palacios (2004). "Measurement of armor damage on rubble mound structures: comparison between different methodologies." In: *Coastal Structures 2003*, pp. 189–200.

Xu, Haixia and Ping Dong (2011). "A probabilistic analysis of random wave-induced liquefaction." In: *Ocean Engineering* 38.7. Offshore Geotechnics, pp. 860 –867. ISSN: 0029-8018. DOI: https://doi.org/10.1016/j.oceaneng.2010.10.011.

Ye, Jianhong, D.-S. Jeng, P.L.-F. Liu, A.H.C. Chan, Wang Ren, and Zhu Changqi (2014). "Breaking wave-induced response of composite breakwater and liquefaction in seabed foundation." In: *Coastal Engineering* 85, pp. 72 –86. ISSN: 0378-3839.

Ye, Jianhong, Dongsheng Jeng, Ren Wang, and Changqi Zhu (2015). "Numerical simulation of the wave-induced dynamic response of poro-elastoplastic seabed foundations and a composite breakwater." In: *Applied Mathematical Modelling* 39.1, pp. 322 –347. ISSN: 0307-904X.

Ye, Jianhong, D.-S. Jeng, A.H.C. Chan, R. Wang, and Q.C. Zhu (2016). "3D Integrated numerical model for fluid–structures–seabed interaction (FSSI): Elastic dense seabed foundation." In: *Ocean Engineering* 115, pp. 107 –122. ISSN: 0029-8018.

Zen, Kouki and Hiroyuki Yamazaki (1990). "Mechanism of wave-induced liquefaction and densification in seabed." In: *Soils and Foundations* 30.4, pp. 90–104.

Zhao, HY, D-S Jeng, JS Zhang, CC Liao, HJ Zhang, and JF Zhu (2017). "Numerical study on loosely deposited foundation behavior around a composite breakwater subject to ocean wave impact." In: *Engineering Geology* 227. New Advances in Coastal Engineering Geology and Geotechnics, pp. 121 –138. ISSN: 0013-7952.

Zijlema, M. and G.S. Stelling (2008). "Efficient computation of surf zone waves using the nonlinear shallow water equations with non-hydrostatic pressure." In: *Coastal Engineering* 55.10, pp. 780 –790. ISSN: 0378-3839.

Zijlema, Marcel and Guus S. Stelling (2005). "Further experiences with computing nonhydrostatic freesurface flows involving water waves." In: *International Journal for Numerical Methods in Fluids* 48.2, pp. 169–197.

Zijlema, Marcel, Guus Stelling, and Pieter Smit (2011). "SWASH: An operational public domain code for simulating wave fields and rapidly varied flows in coastal waters." In: *Coastal Engineering* 58.10, pp. 992 –1012. ISSN: 0378-3839.

van Gent, Marcel (2013). "Rock stability of rubble mound breakwaters with a berm." In: *Coastal Engineering* 78, pp. 35–45.

van Gent, Marcel and Ivo van der Werf (2014). "Toe stability of rubble mound breakwaters." In: *Coastal Engineering Proceedings* 1.34, p. 22.

van Gent, Marcel, Alfons J Smale, and Coen Kuiper (2004). "Stability of rock slopes with shallow foreshores." In: *Coastal Structures 2003*, pp. 100–112.

Daniele Celli

Curriculum Vitae

Short introduction

Daniele is a Ph.D. student in coastal engineering at the final year. His reseach is focused on the stability of coastal structures such as conventional rubble mound breakwaters and breakwaters with sumberged berm, from numerical and experimental point of view. He is also engaged in the research on wave-seabed-structure interaction (WSSI) for the evaluation of liquefaction phenomena around marine structures.

Education

Sep. 2017 **FIRST certificate**, *Cambridge Language Assessment*.

July 2016 **PET certificate**, *Cambridge Language Assessment*.

Oct. 2016 **Course on analytical methods for the differential equations solutions**, *University Rome Tor Vergata*, Rome.

Oct. 2016 **Course on analytical methods for the differential equations solutions**, *University Rome Tor Vergata*, Rome.

June 2016 **"Labview Core 1" course**, *Technical University of Bari*, Bari.

2011 – 2015 **Master degree in Civil Engineering**, *University of L'Aquila*, L'Aquila, Thesis: Lattice-Boltzmann model of flow over spillways.
Supervisors: Prof. Marcello Di Risio, Prof. Carmine di Nucci - Final grade: 110/110 cum laude

2006 – 2011 **Bachelor degree in Civil Engineering**, *University of L'Aquila*, L'Aquila, Thesis: : An hydraulic model for complex water systems..
Supervisors: Prof. Aniello Russo Spena, Prof. Carmine di Nucci - Final grade: 107/110

Experience

Jan – June 2018 **Visiting Ph.D. student within the framework of wave-seabed-structure interaction**, *Univestity of Stavanger*, Stavanger, Supervisor: Prof. Muk Chen Ong.

Nov 2015 – Present **Ph.D student within the framework of experimental and numerical study on the interaction between waves and rubble mound breakwaters with submerged berms**, *Technical University of Bari*, Bari, Supervisors: Prof. Michele Mossa, Prof. Marcello Di Risio.

C.da Colle dell'Orso 51/G – 86100 Campobasso (Italy)
(+39) 334 7460197 • daniele.celli@poliba.it

Jun – Oct 2015 **Scholarship student at the LIAM-DICEAA of the University of L'Aquila in numerical and experimental analysis for the hydraulic structures efficiency**, *University of L'Aquila*, L'Aquila, Supervisor: Prof. Marcello Di Risio.

Scientific publications

International Journal

February 2018 **Effects of submerged berms on the stability of conventional rubble mound breakwaters, Coastal Engineering, pp. 16-25, doi: https://doi.org/10.1016/j.coastaleng.2018.01.011**, *Celli, D., Pasquali, D., De Girolamo P., Di Risio M., (2018).*

Dicember 2016 **Post-Event Site Investigation, Monitoring, Stability Analysis, and Modeling of a Gas Pipeline Explosion, Journal of Failure Analysis and Prevention, pp. 1-7, doi:10.1007/s11668-016-0212-0**, *Totani, G., Totani F., Celli, D., Pasquali, D., Di Risio M., (2016).*

International Journal - under review

August 2018 **The role of submerged berms on the momentary liquefaction around conventional rubble mound breakwaters, submitted to Applied Ocean Research**, *Celli, D., Li, Y., Ong M.C., Di Risio M., (2018)).*

August 2018 **A simplified hindcast method for the estimation of extreme storm surge events in semi- enclosed basins, submitted to Applied Ocean Research**, *Pasquali, D., Bruno M.F., Celli, D., Damiani, L., Di Risio M., (2018).*

Conference paper

October 2018 **The influence of submerged berms on the stability of rubble mound breakwaters, XXXVI National Congress of Hydraulic and Hydraulic Structures, Ancona**, *Celli, D., Pasquali, D., Li, Y., Ong M.C., Di Risio M.*

October 2018 **The analysis of an inner harbour wave agitation, XXXVI National Congress of Hydraulic and Hydraulic Structures, Ancona**, *Pratola L., Rinaldi A., Molfetta M.G., Bruno M.F., Celli, D., Pasquali, Di Risio M., Mossa M.*

October 2018 **A method to assess wave energy variability within the frame of a multicriteria approach, XXXVI National Congress of Hydraulic and Hydraulic Structures, Ancona**, *Di Risio M., Celli, D., Pasquali, D.*

October 2018 **Underwater Remotely Operated Vehicles for fast and low cost bathymetry surveys, IEEE INternational Workshop on Metrology for the sea, Bari**, *Di Risio M., D'Ovidio G., Celli, D., Pasquali, D.*

October 2018 **The role of submerged berms on the stability of rubble mound breakwaters,AIOM-PIANC days, Lecce**, *Celli, D., Pasquali, D., Di Risio M.*

September 2018 **Optimal selection of deployment site for wave energy devices, SDEWES Conference, Palermo**, *Di Risio M., Greco P., Celli, D., San Lorenzo D., Pasquali, D.*

Technical Reports

2015 – 2016 **Hydrological monitoring of Colle di Roio (L'Aquila, Italy)**, *Laboratory of Hydraulic and Maritime Constructions (LIAM), University of L'Aquila*, Leopardi M., Di Risio M., Pasquali D., Celli D., Scorzini A., Matergia L.

Research Projects

2018 **2D hydraulic model tests of the Fishery Port at Duqm (Oman)**, *Laboratory of Hydraulic and Maritime Constructions (LIAM), University of L'Aquila*, Scientific supervisor:, Prof. Marcello Di Risio - Role: scientific assistant.

2016 **GERDP: Complete model, Plunge Pool - Movable bed tests**, *Laboratory of Hydraulic and Maritime Constructions (LIAM), University of L'Aquila*, Scientific supervisors: Prof. Paolo De Girolamo, Prof. Marcello Di Risio - Role: scientific assistant.

Conference

Oct. 2018 **AIOM-PIANC days, Lecce (IT)**.

Sep. 2018 **IDRA2018: National Conference on Hydraulics and Hydraulic Structures, Ancona (IT)**.

June 2018 **PhD Days: National conference, Catania (IT)**.

Oct. 2017 **SCACR: International Short Course and Conference on Applied Coastal Research, Santander (SPA))**.

June 2017 **PhD Days: National conference, Torino (IT)**.

Sep. 2016 **IDRA2016: National Conference on Hydraulics and Hydraulic Structures, Bologna (IT)**.

Advisor activities for master thesis

2018 **Title: Numerical modelling of submerged berms influence upon the seabed wave-induced pressure under rubble mound breakwaters**, *Student: Valerio Cotturone*, University of L'Aquila. Role: Co-advisor.

2016 **Title: Numerical model to investigate the fluid flow across the spillway ski jump**, *Student: Giampaolo Carducci*, University of L'Aquila. Role: Co-advisor.

2015 **Title: Numerical model to investigate the role of submerged landslides initial acceleration on the impulsive waves generation**, *Student: Benedetto Di Paolo*, University of L'Aquila. Role: Co-advisor.

Computer skills

Basic C,C++

Intermediate Comsol Multiphysics, Epanet, Palabos, Paraview, OpenFOAM, Linux, IHFOAM, olaFlow, SWAN

Advanced LaTeX, SWASH, python, Matlab, Autocad, Microsoft Office, Photoshop

Languages

Italian	**Mothertongue**	
English	**Intermediate**	*Conversationally fluent*
Spanish	**Basic**	*Basic words and phrases only*

C.da Colle dell'Orso 51/G – 86100 Campobasso (Italy)
(+39) 334 7460197 • daniele.celli@poliba.it